University of Alberta

Multi-scale mantle reflectivity imaging using secondary seismic arrivals

by

Ryan James Schultz

A thesis submitted to the Faculty of Graduate Studies and Research
in partial fulfillment of the requirements for the degree of

Master of Science
in
Geophysics

Department of Physics

Fall 2012
Edmonton, Alberta

Your file Votre référence
ISBN: 978-0-494-91434-2

Our file Notre référence
ISBN: 978-0-494-91434-2

Abstract

On the global scale, seismically observed stratifications in mantle reflectivity have been attributed to mineralogical phase changes of olivine. Analysis of a large set of SS precursors constrains the topography of mantle stratifications beneath parts of the descending Pacific plate along the Honshu and Kuril islands. These findings provide compelling evidence for strong deformations in the stagnant slabs and for lower-mantle penetrating lithosphere. Alternative to SS, P′P′ precursors promise to resolve the fine scale structure in the mantle, owing to its short-period nature, shallow angle of incidence and nearly symmetric Fresnel zone. Unfortunately, P′P′ precursors are known for several complications: phase triplication and the maximum-phase Fresnel zones result in strong scattering and asymmetric arrivals. This thesis purports a means for resolving fine scale mantle structure with the problematic P′P′ phase. Results indicate resolutions competitive with receiver functions, but with the advantage of the P′P′ precursor distribution.

Acknowledgements

I would like to thank my advisor, Jeff Gu, for his mentorship during my time at the University of Alberta. Additionally, I would like to extend thanks to my peers in research: Ahmet Ökeler, Sean Contenti and Luyi Shen.

Contents

1 Introduction 1

1.1 Background 1

1.2 Motivation 3

1.3 Thesis outline 5

2 Tracking slabs beneath subduction zones 8

2.1 Data and Method 12

2.2 Results 14

2.2.1 Maps of reflection amplitudes 14

2.2.2 Cross-sections of reflectivity and seismic velocity 17

2.3 Discussion and interpretations 20

2.3.1 Average reflection amplitudes 22

2.3.2 Depth correlation of the 410 and 660 23

2.3.3 Continuity of the 410 25

2.3.4 Slab stagnation and distortion 27

2.3.5 Slab penetration beneath southern Kuril arc 31

2.3.6 Other HRZs and their potential origins 33

2.4 Conclusions 34

3 The Radon transform **36**

3.1 Theory 38

3.2 Application of the Radon transform 42

3.3 Conclusions 46

4 Development of P'P' analysis **48**

4.1 Method 51

4.1.1 Preprocessing 51

4.1.2 Deconvolution 52

4.1.3 Partial stacking 54

4.1.4 Radon transform 55

4.1.5 Migration 56

4.2 Synthetic tests 59

4.2.1 Discussion 60

4.3 Conclusions 61

5 Analysis of the South America subduction zone **62**

5.1 Processing details 65

5.2 Multi-scale migration results 68

5.3 Discussions 71

5.3.1 Implications for mantle stratification and dynamics 72

5.4 Conclusion 77

6 Conclusions **78**

6.1 Future direction and suggestions 81

Bibliography **82**

Appendices

List of Figures

2.1 (a) Schematic drawing of a SS precursor reflecting from a subducting oceanic lithosphere at the base of upper mantle. These waves are sensitive to the depths of mantle interfaces and the impedance contrasts across them. (b) Key steps in the time-to-depth conversion of SS precursors. By placing the aligned SS precursors at the surface (middle), we map a given time sample prior to the arrival of SS (left) to the appropriate reflection depth along the predicted differential time curves computed based on PREM (Dziewoński and Anderson, 1981). The right panel shows the isotropic shear velocities of PREM down to 1200-km depth. 11

2.2 Ray theoretical surface reflection points of 6014 high-quality SS precursors used in this study. The main tectonic elements, plate boundaries (Bird, 2003) and slab contours (Gudmundsson and Sambridge, 1998) are indicated by dashed lines and thin solid lines, respectively; the slab contours are taken at 50 km intervals from the trench. All SS BPs represented by circles contribute to the construction of 3D reflectivity maps (see Figure 2.3), while only solid circles are used in the examinations of four vertical Profiles A-D (see Figure 2.4). 14

2.3 Interpolated reflectivity maps of SS precursor amplitude variations at MTZ (A to C) and shallow lower-mantle (D) depths. The thin magenta lines show the slab contours from Gudmundsson and Sambridge (1998). The viewing angles differ slightly among the four panels. The abbreviation Mt = Mountain. The color bar on the left is used for the reflection maps shown by panels A and C, and the one on the right is used to produce the remaining two panels. 16

2.4 Interpolated reflection stacks along Profiles A to D (see Figure 2.2) superimposed on high-resolution P-wave velocities from Obayashi et al. (2006). The magenta circles show the earthquakes within the averaging window of each profile and the sizes of the circles scale with event magnitudes. Seismic activity extends down to 650 km and outlines the Wadati-Benioff zone in the northwestern Pacific region. Key observations are encircled or highlighted by dotted lines and arrows. 18

2.5 A comparison of depth-converted reflection amplitudes at 680-km depth based on averaging CMP gathers of (a) $2° \bullet 6° = 12°^2$, and (b) $5° \bullet 10° = 50°^2$. The numbers on the left side of the equations are the dimensions (in arc deg) of the CMP gathers along section-parallel and section-perpendicular directions, respectively. The right side of the equation indicates the uniform CMP area for each experiment. Significant scatter in Figure 2.5a suggests instability associated with limited numbers of traces in some CMP gathers, while the results in Figure 2.5b suffers from over-smoothing. The main reflective structures such as strong depressions near the deepest part of the Wadati-Benioff zone are consistent between these maps. 22

2.6 (a) A subsection of the migrated reflectivity along Profile A. The gray circles mark the locations and sizes of deep earthquakes along the profile (see Figure 2.4 for details). The contours superimposed on the shaded reflection amplitudes are taken at 4% and 8% values. (b) Magnified subsections of reflection amplitude near the top of the MTZ for all three profiles. The highlighted region shows a relatively continuous 410 above the stagnant part of Honshu slab. 25

2.7 The observed depths of the 410 and 660 beneath Profiles A-C with interpretations. The undulations on the 410 and 660 have been exaggerated by a factor of 2 from the original observations presented in Figure 2.4. The short dashed lines mark regions of low reflection amplitude and the white arrows indicate the dip of the Wadati-Benioff zones. The region shaded in blue shows 1% P velocity perturbations from Obayashi et al. (2006), and the regions shaded in green (see Profiles A and B) represent interpreted MTZ low-temperature regimes based on the observed SS precursor amplitudes of this study. Three distinct sub-regions at the base of the upper mantle are labeled Seg 1-3. Their dimensions are estimated based on a reference depth of 670 km and rounded to the nearest 50 km. In Figure 2.7a, the region shaded in gray shows the shape of a stagnant slab from recent numerical simulations that consider temperature- and pressure-dependent viscosity (edited from Figure 2.12 of Fukao et al., 2009 and Figure 2.4 of Nakakuki et al., 2010). 29

3.1 Schematic diagram depicting the Radon transform. Linear path-functions are focused around the distance parameter δ in the spatial domain (left panel). Integration paths defined by ray parameters p1, p2 and p3 intersect in the spatial domain at (τ, δ) (left panel), which are projected to the Radon domain as energy foci (right panel). Integration along ray parameter p3 maps the high-amplitude phase in the spatial domain to an energetic signal in the Radon domain (dark solid circle). A weaker Radon signal results from integrating along parameter p1 (gray circle, right panel), due to smaller amplitude phase move-out, while an integration path devoid of arrivals (see p2) yields minimal Radon energy (white circle). It should be noted that these three paths only intersect at the designated distance parameter δ, whereas any other choice would result in distinct τ arrivals in the Radon domain. 39

3.2 Radon transform of a simulated record section containing SS and its precursors. (a) SS and its precursors in the spatial domain. The synthetic seismograms have been aligned on SS. Precursors resulting from discontinuities at 220, 410 and 660 km are highlighted by solid lines. The depths of the 410- and 660-km seismic discontinuities are 400 and 670 km, respectively, in PREM. (b) Instantaneous amplitude of the Radon transform, where the inversion was regularized using an ℓ_2 norm and $\delta \approx 125$. Distinct peaks in Radon domain are attributed to each ray parameter and their respective slopes in the spatial domain. Additional Radon inversions are performed using (c) ℓ_1 and (d) Cauchy methods. Sharper signals are observed in these two cases, especially for SS, due to the emphasis on sparseness. The variance of the residuals was kept constant to ensure a fair comparison of the inversion methods. 43

3.3 Resampling and filtering of seismic data using RT. (a) An irregularly sampled synthetic record section containing SS and its precursors. (b) Instantaneous amplitude of RT based on ℓ_2 regularization. (c) Reconstructed and spatially interpolated record section by applying the forward operator on the Radon signal. (d) Result of applying the forward operator after retaining only the RT signals associated with $S_{220}S$ and $S_{660}S$. 45

3.4 RT of receiver function data from station EDM. (a) A record section showing nonlinear arrivals originated from crustal multiples and P-to-S conversions at the 410- and 660-km discontinuities. (b) Instantaneous amplitude of RT domain signals. The transform is computed based on the ℓ_2 norm, parabolic path-functions and $\delta = 30$. Signals corresponding to P410s and P660s are recognizable, especially the former due to coherent, energetic arrivals in the spatial domain. A first-order crustal reverberation, near the main P arrival, is labeled M1 in both panels. 46

4.1 Ray paths for various bottom-side reflection phases (a). P′P′ phases ($PKPPKP_{AB}$, $PKPPKP_{BC}$, PKiKPPKiKP and PKIKPPKIKP) have antipodal bounce points, while SS and PP (not shown, analogous path to SS) have bounce points which are roughly the geometric mid point. All of these phases may also have precursory arrivals due to reflections below the surface. Move-out curve for P′P′ and $P'_{660}P'$ phases (b) based on ak135 earth model. All P′P′ phases have a negative, apparent slowness due to their long (>180°) paths. 50

4.2 Surface Fresnel zones for SS (a) and PKIKPPKIKP (b). Fresnel cutoffs are depicted with black contour lines, based on a quarter of the phase's period. SS phases are minimum-maximum and bounded by 20°, while PKIKPPKIKP is maximum phase and bounded by roughly 4°. 50

4.3 Deconvolution of a single P′P′ seismogram. The seismogram (a) shows the P′P′ arrival, which has been windowed for deconvolution. The signal on the second panel (b) has been deconvolved from this P′P′ waveform, which now appears as a simpler impulse (scaled to an amplitude of 1.0). The deconvolved signal has been enhanced using a running average of seismic energy, to elucidate other arrivals. Precursory arrivals have been labeled according to their estimated depths, other interfering arrivals (podal PKiKPPKiKP and PKKP) will be omitted from migration in the Radon process. A test (c) determines optimal damping at the zero crossing of the test value. Numbers indicate step progression in interpolating toward optimally damped solution. The final panel (d) is smaller section of the deconvolved trace, showing MTZ reflections more closely. 54

4.4 Caricature depicting sample ray paths for specular, asymmetric and scattered SS arrivals (a), incorporation of all arrivals is important for further P′P′ analysis (P′P′ paths not shown). Dotted lines show specular arrivals for the main phase and precursor. Ray paths for forward scattering (path 2) and an asymmetric reflection due to a dipped surface (path 1) are also depicted. Migration mappings for SS (b) and P′P′ (c) are tabulated using epicentral distances of 130° and 60°, respectively. The P′P′ phase has the potential to constrain whole mantle structure while SS only permits the analysis of the upper-mantle. Specular reflections are confined to time and ray parameter values along the white line. Non-specular ray paths are also defined for various scattering depths, ray parameters and differential times. Scattering from a constant reflector depth defines contours (isobaths) in this domain and reveals P′P′ and SS are maximum phase with respect to perturbations in ray parameter. 58

4.5 Statistical results from synthetic tests on RPA. Absolute value of the residual bias (a) and residual standard deviation (b). A general trend of decreasing accuracy, reliability and stability are noted for decreasing cap sizes and/or SNR ratio. The resolution baseline is determined by the Nyquist frequency, the smallest possible resolving power of a seismogram. An acceptable level (Resolution threshold) was chosen as twice this and caps above this value are deemed too unstable for reliable analysis. 60

5.1 BPs of the 5720 traces used in the study of Contenti et al. (2012) (a). Slab contours are represented by thin grey lines (Gudmundsson and Sambridge, 1998), plate boundaries are depicted with thick black lines (Bird, 2003) and plate motions by filled arrows (Kreemer et al., 2003). The reflectivity cross section path is bounded by the points A and A′, the results of which are in panel (b). Interpreted position of the Nazca slab is outlined in white and the 410, 520 and 660 discontinuites are denoted with black lines laterally along the cross section and white circles indicate earthquake hypocenters. Radial white lines reference the cap centres studied in this chapter (see Figure 5.2). Figure is modified after Contenti et al. (2012). 64

5.2 Two sample caps near South America. The distribution of BPs for SS (red triangles) and P'P' (blue circles) are depicted for two caps (Cap 1 and 2) sampling oceanic and subduction zones. Cap 1 contains 778 SS and 381 P'P' traces, while Cap 2 contains 469 SS and 276 P'P'. Subducted lithosphere is represented by green contours (Gudmundsson and Sambridge, 1998). 65

5.3 Spatial data has been transformed into the Radon domain for Cap 1 (a and c) and 2 (b and d) with specular reflections occurring along the black line. The low frequency content of SS data (a and b) manifests as large sidelobes. Oceanic data (a) depicts a strong, specular reflection of 660 (γ). In contrast, depression of the 660 in subduction zones implies a dipping reflection interface, evidenced in the Radon image (b). P'P' Radon domains (c and d) starkly contrast SS counterparts. Arrivals are completely independent, no sidelobes are apparent. Many of the P'P' precursors are non-specular and thus difficult to interpret in the Radon domain. Migration will correctly assign a depth to all arrivals, regardless of scattering or asymmetric reflections. Letters and numbers provide labels to phases referred to in the text. 67

5.4 Migration profiles for Cap 1 and 2. Migration for SS (red-filled traces) and P'P' (blue-filled traces) is repeated for both their positive (upper half) and negative (faded lower half) amplitude information. Positive amplitude information is used to infer mantle structure, dynamics and composition local to the south eastern Pacific ocean (a) and subduction zone (b) caps. Letters and numbers (color-coded) provide labels to phases referred to in the text. . 68

List of Symbols and Abbreviations

α	Shorthand for seismically observed $S_{410}S$
β	Shorthand for seismically observed $S_{520}S$
χ^2	Statistical test to determine goodness of fit or independence of observations
Δ	Epicentral distance
δ	distance parameter in Radon inversion
ℓ_p	A generalized vector norm, calculated by taking the p-th root of elements raised to the p-th power and then summed
γ	Shorthand for seismically observed $S_{660}S$
μ, λ, b	Hyperparameters in Radon optimization
Ω	Shorthand for seismically observed mid mantle SS reflection
ω	Frequency
τ	Intercept variable in the Radon domain
$\mathbf{A}$	Time shift operator
$\mathbf{Q}$	Diagonal matrix
A	A seismic waveform of a bottom-side reflected phase

A_d	A seismic waveform for precursors to bottom-side reflected phase
D	Deconvolved trace
H	Transfer function
i, j, k, l, m	Vector/matrix indecies
J	Cost function
M	Spatial domain
p	Ray parameter
R	Radon domain
r	Response to reflection
S	A seismic trace including bottom-side reflected phase and precursors
s	Seismic source function
T	A time shift function
t	Seismic arrival time
410	410-km discontinuity
520	520-km discontinuity
660	660-km discontinuity
ak135	A layered model of Earth's seismic structure
Al	Aluminum
CMP	Common mid point
Fe	Iron
GCMT	Global Centroid Moment Tensor

GDSN Global Digital Seismic Network

GEOSCOPE Global Netwok of Broad Band Seismic Stations

H_2O Water

HRZ Highly reflective zone

IRIS Incorporated Research Institutions for Seismology

IRLS Iteratively Reweighted Least Squares

Ma Megaannum, one million years ago

MTZ Mantle transition zone

Mw Earthquake moment magnitude

OH Hydroxyl group

P′ A shorthand notation for triplicated waves PKP, PKIKP and PKiKP

PREM Preliminary Reference Earth Model

RPA Robust precursor analysis

RT Radon transform

SNR Signal to noise ratio

X Shorthand for seismically observed reflection of SS from the X-discontinuity

CHAPTER 1

Introduction

1.1 Background

Subduction plays an integral role in the mantle by transporting lithospheric mass, sediments and water back into the underlying mantle, arguably driving mantle convection. At convergent plate boundaries oceanic lithosphere is forced under continental margins, descending into the mantle transition zone (MTZ). This process is chiefly perpetuated by the negative buoyancy of slab material, which is colder and denser than the surrounding ambient mantle. Additionally, the descent of the slab is aided on contact with the 410 km discontinuity (major discontinuities are denoted by their average depth), a globally observed seismic discontinuity ascribed to the transition of olivine to wadsleyite (Ringwood, 1975; Ita and Stixrude, 1992). The positive Clausius-Clapeyron relation of this phase transition implies a promotion of material flux through its boundary (Schubert et al., 1975) and an elevation in discontinuity depth with decreased temperature (and *vice versa*). Opposite to sign of the 410's Clausius-Clapeyron relation, the 660 is interpreted as the endothermic post spinel transition of ringwoodite to perovskite and magnesiowustite (Ringwood, 1975; Ita and Stixrude, 1992; Lebedev et al., 2002b). Buoyant forces from the post spinel transition resist plate motion, potentially deflecting impinging slab material (Weidner and Wang, 1998;

Bina and Kawakatsu, 2010). If conditions are favourable, stagnation of slab material within the MTZ is possible, with proposed simulations considering trench migration (Christensen, 1996; Billen, 2010), slab weakening (Nishihara et al., 2006) or variable viscosity (Karato and Wu, 1993). Results from tomographic imaging reason that faster-than-average seismic velocities along the Wadati-Benioff zone are a byproduct of cold subducting material, favoring cases for slab penetration (van der Hilst et al., 1997; Sambridge and Gudmundsson, 1998; van der Hilst and Karason, 1999) and stagnation (van der Hist et al., 1991; Fukao et al., 2001; Christensen, 1995; Billen, 2008). Stagnation manifests in a variety of morphologies, *i.e.*, flattening or buckling, with indication that stagnated slab may reside within or below the MTZ (Kárason and van der Hilst, 2000; Fukao et al., 2009). For example, olivine within a slab (made metastable through slow kinetics and fast descent) would act as a ballast attempting to 'resurface' slab material to the 410. Depressions to the topography of 660 silhouettes stagnant slab configuration, as thermal effects from cold slab material depresses the adjacent 660, according to the Clausius-Clapeyron relation.

The infiltration of slab material to the mantle heralds considerable chemical heterogeneity. Dehydration of water-rich slabs is accommodated by olivine and wadsleyite (Inoue et al., 1995; Kohlstedt et al., 1996), with wadsleyite being more accommodating. The transition phase loops of these minerals are affected by presence of water and other chemical heterogeneities introduced from the slab (*e.g.*, Kohlstedt et al., 1996; Weidner and Wang, 2000; Akaogi et al., 2002; Smyth and Frost, 2002). The supersaturation of olivine beyond its solidus potentially allows for the production of neutrally buoyant melt, which resides atop the 410 (Revenaugh and Sipkin, 1994; Inoue, 1994; Tauzin et al., 2010). The subduction processes can potentially feed this phenomenon through the viscous entrainment of water-rich wadsleyite into the less water soluble upper mantle (Leahy and Bercovici, 2007; Schmerr and Garnero, 2007; Leahy and Bercovici, 2010). Flattened portions of slab are thought to undergo a less vigorous process, with water-rich constituents percolating upwards (Lei and Zhao, 2005; Huang and Zhao, 2006).

1.2 Motivation

Much of what is known about mantle is based on the interpretation of changes in impedance (velocity • density), loosely defined as seismic discontinuities or reflectors depending on the spatial scale and orientation of the interface. Two prominent examples are the 410 and 660, which are widely observed and bound the MTZ in one-dimensional reference Earth models (Dziewoński and Anderson, 1981; Kennett and Engdahl, 1991; Morelli and Dziewonski, 1993; Kennett et al., 1995). On the global scale, these mantle stratifications have been attributed to mineralogical phase changes of olivine (Ringwood, 1975; Katsura and Ito, 1989; Ita and Stixrude, 1992), though their properties are variably affected by other mantle constituents such as garnet, water and trace elements/ions (Kohlstedt et al., 1996; Weidner and Wang, 2000; Akaogi et al., 2002; Smyth and Frost, 2002; Ohtani, 2005; Saikia et al., 2008; Inoue et al., 2010). In comparison, detection and interpretation of additional seismic discontinuities/reflectors above (Revenaugh and Jordan, 1991a; Revenaugh and Sipkin, 1994; Gu et al., 2001), within (Shearer, 1990; Gu et al., 1998) and below (Revenaugh and Jordan, 1991b; Niu and Kawakatsu, 1997; Gu et al., 2009) the MTZ are less frequent and remain questionable on the global scale (Deuss and Woodhouse, 2002; Deuss, 2009). Key sources of uncertainty for both known and postulated reflectors are the accuracy and resolution of detection methods, as proper assessment of the strength, spatial location and dimension of a targeting structure generally requires significant enhancement of the associated secondary seismic phases in time and/or transformed domains (Rost and Thomas, 2009; Rondenay, 2009; Gu and Sacchi, 2009). Improvements in data coverage and assessments through diverse and multi-resolution approaches are some of the most effective means to reduce the uncertainties in characterizing the mantle.

Among the various approaches, results from long-period SS/PP precursors (Shearer, 2000; Helffrich, 2000; Kind and Li, 2003; Deuss, 2009; Gu et al., 2012) and high frequency receiver functions (Ammon, 1991; Ligorria and Ammon, 1999; Rondenay, 2009) are routinely compared to increase the confidence of the recovered mantle stratifications. SS and PP

precursor signals made a significant impact on the understanding of upper mantle discontinuities (Shearer, 1991b; Shearer and Masters, 1992; Flanagan and Shearer, 1998; Gu et al., 1998, 2003; Deuss et al., 2006; Houser et al., 2008; Thomas and Billen, 2009; Houser and Williams, 2010; Schmerr and Thomas, 2011), with their analysis typically having bandwidths around 6-75s (Shearer, 1991b; Deuss et al., 2006). Their large distance ranges (80-160°) and dependency on bounce point (abbreviated BP) are ideal for mapping the amplitude and topography of discontinuities on the global scale. However, the long-period frequencies and minimum-maximum Fresnel zones negatively impact their resolvability (Shearer, 1993; Chaljub and Tarantola, 1997; Neele et al., 1997; Schmerr and Garnero, 2006). Receiver function approaches have proven to be highly successful in constraining the mineralogy and dynamics beneath continents and plate boundary zones (Sheehan et al., 1995; Suetsugu et al., 2009; Schulte-Pelkum et al., 2005; Andrews and Deuss, 2008; Rondenay et al., 2008), but their reliance on station density and location severely limits its effectiveness globally due to the prohibitive cost associated with ocean-bottom seismic deployments.

The short-comings of receiver functions and SS/PP precursors pose limitations to their applicability. Alternatively, precursors to the phase P′P′ are both high frequency (Teng and Tung, 1973; Tkalčić et al., 2006) and partially decoupled from receiever location (Adams, 1968). The high frequency nature of P′P′ samples mantle structure on a scale comparable to receiver functions, without the dependence on station location. Ostensibly it may seem that analysis of P′P′ is superior to SS/PP precursors or receiver functions. However, P′P′ is rife with complications; small precursor amplitude, phase triplication (Adams, 1968), complicated source mechanisms, maximum-phase Fresnel zones (Day and Deuss, 2010), scattering and asymmetric arrivals (Tkalčić et al., 2006; Earle et al., 2011; Wu et al., 2012) prove detrimental. These complications have limited P′P′ applicability, with only a handful of studies on the subject presenting themselves in the past century. This thesis develops methodology to overcome the problems associated with P′P′. Deconvolution of P′P′ removes the source function, allowing for the estimation of the reflectivity series below the BP. The Radon transform (for brevity RT) incorporates ray parameter information to the spatial data, enabling the removal of extraneous phases. Ray parameter information

unambiguously characterizes reflected, asymmetric and scattered arrivals. Coupled with migration techniques, precursors are accurately mapped back to their depth of origin. The combination of these techniques mitigates P'P' problems, enabling the analysis of the fine structure of the mantle.

1.3 Thesis outline

Chapter 2 details a revised approach to SS precursors to provide a two-dimensional snapshot of the present-day mantle stratification beneath western Pacific subduction zones. This section emphasizes the larger scale (~500 km laterally, 25-40 km radially) mantle anomalies and provide a detailed account of the various parts of the Pacific slab near Japan and eastern China. The outcome of this experiment sheds light on the behavior of slabs in the transition zone. Among the various key findings, evidence of strong north-south structural variations at mantle transition depths and irregular structures at the base of upper mantle in the previously dubbed 'flat' part of the stagnant slab could have significant implications for the overall understanding of subduction dynamics. Across Honshu arc, the 410 and 660 are detected at the respective depths of 395±5 and 685±5 km within the Wadati-Benioff zone. Their topographies are negatively correlated along slab dip, showing the dominant effect of temperature on the olivine phase changes within the upper mantle transition zone. The base of the upper mantle shows broad depressions as well as localized zones of shallow/average depths beneath Korea and northeast China. The 15+ km peak-to-peak topography west of the Wadati-Benioff zones suggests that the stagnant part of the subducted Pacific plate is not as flat as previously suggested. Eastward slab 'pile-up' is also possible at the base of the upper mantle. Across southern Kuril arc, the shear wave reflection coefficients of major olivine phase boundaries fall below 5% within the Wadati-Benioff zone. The apparent reflection gaps and the spatial connection between a strong reflector at ~900 km depth may imply possible compositional variations at the top and bottom of the transition zone and substantial mass/heat flux across the 660-km seismic discontinuity. Also identified are strong reflectors within the subducted oceanic lithosphere at mid transition zone depths. The

depths and strengths of these reflectors are highly variable between Honshu and southern Kuril islands.

Chapter 3 reviews the theory, programming designs and merits of two Matlab-based routines for the forward and inverse RT. These routines offer flexible choices of integration path functions to take advantage of improved Radon-domain identification and isolation of seismic phases. Least-squares inversion of frequency components and judicious choices of regularization techniques enables additional noise suppression and signal enhancement in the Radon domain. The forward RT routine has the added benefit of spatial interpolation for irregularly sampled data. The accuracy and applicability of these two routines are demonstrated using data sets containing long-period SS precursors and high-frequency receiver functions. With minimal modifications these two highly portable, carefully documented RT routines could be easily adapted for a broad range of applications.

In chapter 4 I present a general method for the analysis of mantle reflectivity structure using bottom-side reflected phases (*e.g.*, SS, PP and P′P′) and their precursory arrivals. I review the basis and merits of methodology in precursor analysis, while highlighting techniques utilized in this robust method. A suite of synthetic tests are performed to quantify the fidelity and stability of this method under differing noise and data availability conditions, providing a rubric for future analysis. This chapter purports a robust means for determining mantle structure at resolutions more competitive with receiver functions, but with the advantage of P′P′ precursor distribution.

Chapter 5 provides further inquiry to a sample of South America data, demonstrating the consistency in resolving both the broad structure of the mantle for the well known SS phase and the fine structure using the more obscure P′P′ phase. Migration profiles tentatively reveal both olivine and garnet related transitions in the mantle, with some constraints on the sharpness of these transitions. Observations of a depressed 660 are attributed to thermal variations. Prominent 520 arrivals near subducted slab material suggest this transition is sharpened to a thickness resonant with P′P′ ($\sim$11 km). Evidence for a layer of melt at the top of the MTZ is supported by both SS and P′P′ with diminished SS amplitudes and com-

plex P′P′ arrivals. This 'complex' arrival is characterized by a sharp negative arrival marking the initiation of the low velocity zone, scattered arrivals recorded incoherently throughout its extent and finalized by the arrival of the ubiquitous 410. P′P′ and precursors, coupled with methodology described in this study, provide the opportunity to study the existence, depth, sharpness and strength of reflectors/discontinuities offering new constraints on the dynamics and mineralogy of the mantle.

CHAPTER 2

Tracking slabs beneath northwestern Pacific subduction zones[1]

The convergent boundaries between the Pacific, Amurian, and North American plates are among the fastest destruction zones of old oceanic domains. The subduction process in this region initiated prior to the Eocene epoch (> 55 Ma) (Fukao et al., 2001; Northrup et al., 1995) and continues to accommodate regional differential plate motions at the present-day rates of 8-9.5 cm/yr (Bird, 2003; Demets et al., 1990; Seno et al., 1996). The subducted old oceanic lithospheres are colder than the surrounding mantle, hence are manifested as high velocity anomalies in seismic tomographic images (*e.g.*, Fukao et al., 1992; Fukao et al., 2001; Gorbatov and Kennett, 2003; Gorbatov et al., 2000; Grand, 2002; Kárason and van der Hilst, 2000; Lebedev and Nolet, 2003; Li and van der Hilst, 2010; Obayashi et al., 2006; Romanowicz, 2003; van der Hist et al., 1991; van der Hilst et al., 1997; Widiyantoro et al., 1999; Zhao, 2004; Zhao and Ohtani, 2009). The inferred morphologies and depths of subducted oceanic lithospheres (from here on, 'slabs') vary significantly among the various northwestern segments of the Pacific plate boundary. Parts of the Pacific slab exhibit strong deformation

[1] A version of this chapter has been published (Gu et al., 2012, Earth and Planetary Science Letters. 331: 269 - 280.).

near the base of the upper mantle, *e.g.*, 'pile-up' or stagnation (Fukao et al., 1992; Fukao et al., 2001) by as much as 800-1000 km (Huang and Zhao, 2006; Obayashi et al., 2006), while others favor continued descent into the lower mantle (*e.g.*, Fukao et al., 2001; Fukao et al., 2009; Gorbatov and Kennett, 2003; Obayashi et al., 2006). Both modes of slab deformation have been corroborated by recent geodynamical calculations that incorporated trench migration and rollback history (Billen, 2010; Nakakuki et al., 2010; Tagawa et al., 2007; Zhu et al., 2010). The interplay between high and low velocities in connection with descending slabs, multi-scale advection (Korenaga and Jordan, 2004; Obayashi et al., 2006) and transition zone slab dehydration (An et al., 2009; Duan et al., 2009; Feng and An, 2010; Lebedev and Nolet, 2003; Li and van der Hilst, 2010; Obayashi et al., 2006; Priestley et al., 2006; Zhao, 2004; Zhao et al., 2007; Zhao and Ohtani, 2009) is inductive to strong gradients in temperature and composition at depths below 250 km.

In addition to seismic tomography, amplitudes and arrival-times of reflected/converted seismic waves from mantle interfaces are effective measures of changes in rock elastic properties. Slab geometry and transition zone thickness are strongly influenced by mineralogical phase transformations of olivine to wadsleyite near 410 km, wadsleyite to ringwoodite near 520 km, and ringwoodite to perovskite and magnesiowustite near 660 km (Akaogi et al., 2007; Bina, 2003; Helffrich, 2000; Ita and Stixrude, 1992; Katsura and Ito, 1989). The endothermic phase change at the base of the upper mantle increases local buoyancy forces, which can deflect subducting slabs and cause stagnation (Billen, 2008, 2010; Christensen, 1995; Fukao et al., 2009). Assuming an olivine-rich mantle composition and thermodynamic equilibrium, low temperatures from a descending slab are expected to increase the thickness of the transition zone. In fact, broad depressions of the 660-km discontinuity beneath the northwestern Pacific region (*e.g.*, Revenaugh and Jordan, 1991; Shearer and Masters, 1992; Vidale and Benz, 1992) have been widely regarded as crucial observational support for the laboratory experiments.

Among the various observations, bottom-side SH reflections from mantle interfaces known as SS precursors (Shearer, 1991b; Shearer and Masters, 1992) played a key role in

the determination of mantle discontinuity depths. Due to path similarities, the relative times and amplitudes of SS and its precursors are sensitive to reflection characteristics beneath the midpoint of the ray path (Figure 2.1a). In comparison to converted waves (*e.g.*, Lawrence and Shearer, 2006; Lawrence and Shearer, 2008; Tauzin et al., 2008; Rondenay, 2009), seismic imaging based on SS precursors offers more complete global data coverage (Deuss and Woodhouse, 2002; Flanagan and Shearer, 1998; Gossler and Kind, 1996; Gu and Dziewoński, 2002; Gu et al., 1998; Shearer, 1990, 1991b, 1993; Shearer and Masters, 1992; Deuss, 2009), but their resolving powers at length scales appropriate for slabs have been questioned (Chaljub and Tarantola, 1997; Neele et al., 1997; Shearer et al., 1999). With few exceptions (*e.g.*, Heit et al., 2010; Schmerr and Garnero, 2007), comparisons between shear wave reflectivity and velocity near subduction zones generally emphasized low-degree spherical harmonics (*e.g.*, Gu et al., 2003; Houser and Williams, 2010; Houser et al., 2008; Lawrence and Shearer, 2006; Romanowicz, 2003) and remained qualitative at local length scales.

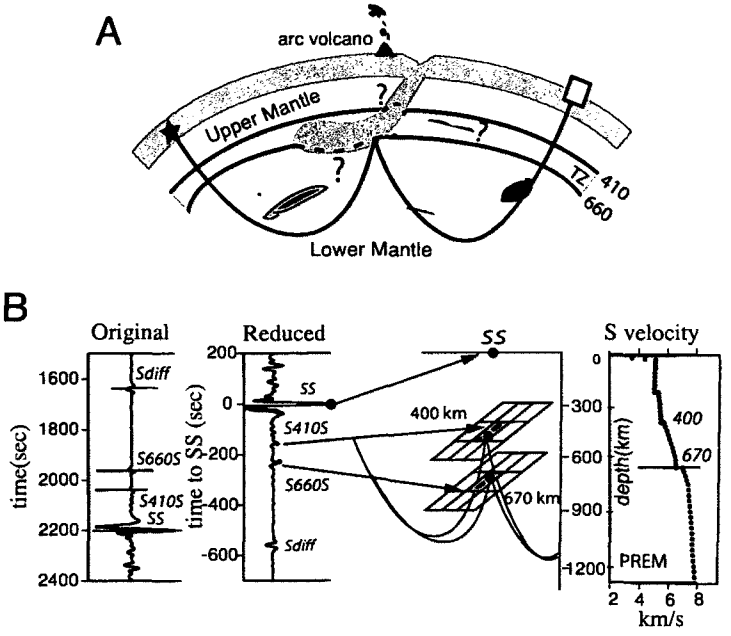

Figure 2.1: (a) Schematic drawing of a SS precursor reflecting from a subducting oceanic lithosphere at the base of upper mantle. These waves are sensitive to the depths of mantle interfaces and the impedance contrasts across them. (b) Key steps in the time-to-depth conversion of SS precursors. By placing the aligned SS precursors at the surface (middle), we map a given time sample prior to the arrival of SS (left) to the appropriate reflection depth along the predicted differential time curves computed based on PREM (Dziewoński and Anderson, 1981). The right panel shows the isotropic shear velocities of PREM down to 1200-km depth.

This study presents new evidence of stagnating and lower-mantle penetrating slabs based on a dense regional dataset of SS precursors and effective imaging techniques. Through detailed comparisons of reflection amplitude and high-resolution seismic velocity, we aim to provide a self-consistent, three-dimensional (3D) snapshot of the mantle beneath the northwestern Pacific region. For brevity the following sections will refer to the upper mantle transition zone as MTZ and the associated seismic discontinuities as the 410, 520 and 660.

2.1 Data and Method

In this study we utilize all available broadband, high-gain recordings of earthquakes prior to 2008, a dataset currently managed by the IRIS Data Management Center and contributed by GDSN, IRIS, GEOSCOPE and many other temporary deployments. We only retain shallow (depth $<$ 75 km) events to minimize the effect of depth phases, and adopt a magnitude cutoff of Mw $>$ 5 to ensure the availability of source mechanisms from GCMT (Dziewoński et al., 1981) for synthetic seismogram computations. We restrict the epicentral distance range to 100°-160° to minimize known waveform interferences from topside reflection and ScS precursors (An et al., 2007; Schmerr and Garnero, 2007), and apply a Butterworth band-pass filter with corner periods at 12 s and 75 s. We further eliminate traces with signal-to-noise ratio lower than 3.0 (Gu et al., 2003) and align the resulting traces on the first major swing of SS. A constant time shift is subsequently added to each trace based on model predicted SS-S_{520}S times to account for variations in crust thickness (Bassin and Laske, 2000) and surface topography (ETOPO5 database) (*e.g.*, Gu et al., 2003). A reference reflection at 520 km offers an effective compromise between reflections at the 410 and 660 despite a potential depth error of 3-5 km for structures 200-400 km away from the MTZ. Finally, each time sample preceding the reference SS time is mapped to a crustal/mantle depth (*e.g.*, Gu et al., 2008; Heit et al., 2010; Zheng et al., 2007) according to travel times predicted by PREM (Dziewoński and Anderson, 1981) (Figure 2.1b). The sampling rate along the depth axis is 1 km.

Figure 2.2 shows the region of interest in this study and 6014 high-quality traces after processing. The ray theoretical reflection points of the precursors are particularly dense in the latitude range of 35°-50°, which enables a direct comparison between southern/central Honshu arc (Profiles A and B) and Kuril trench (Profile C). To obtain a 3D reflectivity image we first partition the study region using a series of equally-spaced, minor-arc cross-sections parallel to Profile A. The perpendicular arc distance between any two cross-sections is 4°, and their end points (hence lengths) vary to reflect the available data coverage. Then,

a series of equal-area Common Mid Point (CMP) gathers are populated along each cross-section with section-parallel and section-perpendicular dimensions of 3° and 8°, respectively. These rectangular bins are adopted to maximize the nominal resolutions, especially along the east-west orientation, while ensuring sufficient data in each bin for noise suppression. We subsequently interpolate the resulting migration stacks using a bi-linear method for 3D visualization. Despite linear interpolation used in each spatial direction, bi-linear interpolation is able to construct new data points from a discrete set of original values based on a quadratic function (Press et al., 2002). Finally, Profiles B-D (see Figure 2.2) differ from cross-sections used in the 3D construction for a closer examination of the targeted slabs, but the CMP selection strategy and size remain unchanged.

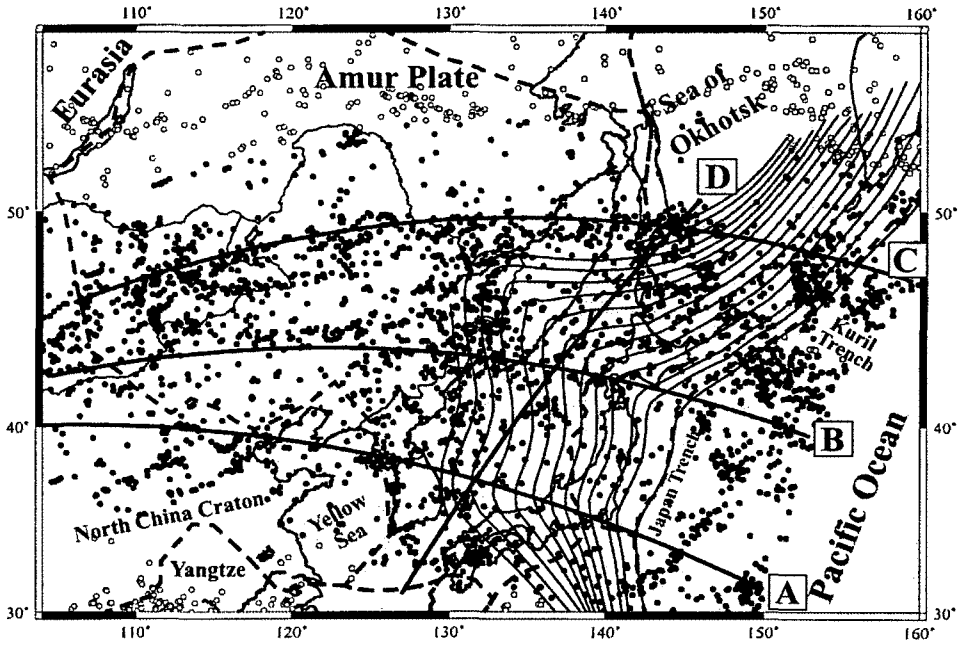

Figure 2.2: Ray theoretical surface reflection points of 6014 high-quality SS precursors used in this study. The main tectonic elements, plate boundaries (Bird, 2003) and slab contours (Gudmundsson and Sambridge, 1998) are indicated by dashed lines and thin solid lines, respectively; the slab contours are taken at 50 km intervals from the trench. All SS BPs represented by circles contribute to the construction of 3D reflectivity maps (see Figure 2.3), while only solid circles are used in the examinations of four vertical Profiles A-D (see Figure 2.4).

2.2 Results

2.2.1 Maps of reflection amplitudes

Stacks of depth-converted S_dS show large-scale structures in the MTZ and shallow lower mantle. The most prominent structure at the top of the MTZ (Figure 2.3a) is an elongated, highly reflective zone (HRZ) that extends from northern Great Khingan Range to Gobi desert in the northwestern corner of the study region. This anomaly reaches a maximum

amplitude of 9.5% relative to SS (for short, 9.5%) at ~425-km depth (Figure 2.3a), approximately 15 km below the global average of the 410 (Gu et al., 2003; Houser et al., 2008), and the limited vertical extent of ~20 km based on 5% reflection amplitude suggests a relative sharp phase transition. A slightly weaker, semi-circular HRZ is further visible in the southwestern corner of the study region, peaking at ~400 km depth and spanning over 1000 km in latitude in northern-central China (see Figure 2.3a). The reflection amplitudes of both HRZs are substantially larger than those within the Wadati-Benioff zones (Gudmundsson and Sambridge, 1998) at the respective depths.

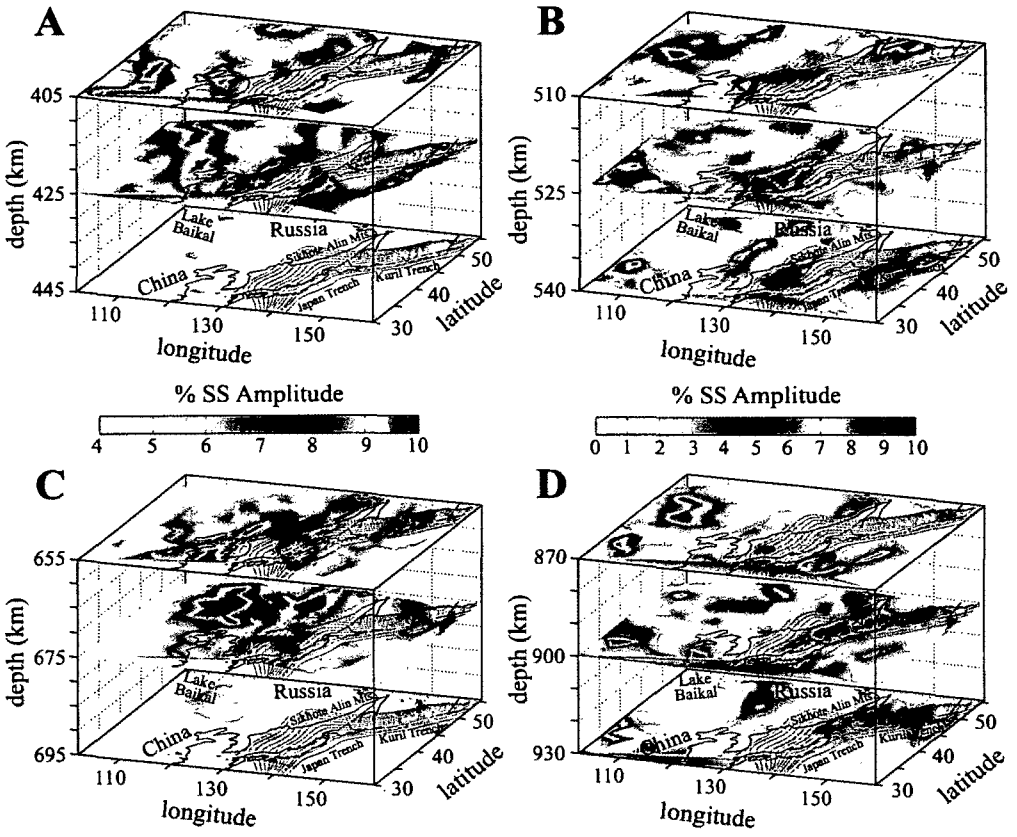

Figure 2.3: Interpolated reflectivity maps of SS precursor amplitude variations at MTZ (A to C) and shallow lower-mantle (D) depths. The thin magenta lines show the slab contours from Gudmundsson and Sambridge (1998). The viewing angles differ slightly among the four panels. The abbreviation Mt = Mountain. The color bar on the left is used for the reflection maps shown by panels A and C, and the one on the right is used to produce the remaining two panels.

The relative reflectivity of Wadati-Benioff zone increases significantly in mid MTZ (Figure 2.3b). A wedge-shaped HRZ with 7-8.5% amplitude is observed near the slab corner between Japan and Kuril subduction zones (Gudmundsson and Sambridge, 1998). This is a localized and sharp anomaly, as the reflection amplitude falls below our detection threshold outside the 515-535 km depth range. While sharpness remains consistent, the strengths and lateral dimensions of HRZs are substantially larger at the base of the upper mantle than

the depths above (Figure 2.3c). At 675 km, major north-south oriented HRZs are present 1) west of the Wadati-Benioff zone, and 2) across eastern Gobi desert (see Figure 2.3c). The maximum amplitudes of 9-12% provide strong regional constraints on the nature and depth of major mineralogical phase transition(s). In comparison, HRZs of similar strengths below 850 km (Figure 2.3d) require a closer examination. As detailed in the following sections, a dominant north-south oriented HRZ at ~900-km depth along southern Kuril seismogenic zone could have significant implications for the dynamics and mineralogy of the lower mantle.

2.2.2 Cross-sections of reflectivity and seismic velocity

To explore the relationship between reflection amplitude and seismic velocity, we overlay depth-converted SS precursors (Figure 2.4) with high-resolution regional P velocities (Obayashi et al., 2006). While the use of a regional S velocity model would be ideal, major heterogeneities in the study region are generally consistent between P and S velocity models (Grand, 2002; Romanowicz, 2003), with the former being potentially better resolved in the western Pacific region (Fukao et al., 2009). The depth-converted SS precursors show clear evidence of sub-horizontal reflectors within depth ranges of 120-180 km, 380-440 km and 630-700 km. The focus of this study is the MTZ and lower mantle where waveform complexities associated with SS side-lobes are negligible (*e.g.*, Gu et al., 2003; Shearer, 1993). To ensure the robustness of the key observations, we estimate the uncertainty of the reflectivity profiles based on a bootstrapping resampling algorithm (Efron, 1979) and subtract two standard deviations from all data stacks. While this procedure slightly reduces the overall signal strength, reflection amplitudes at the depths with large uncertainties are preferentially suppressed for a more objective assessment.

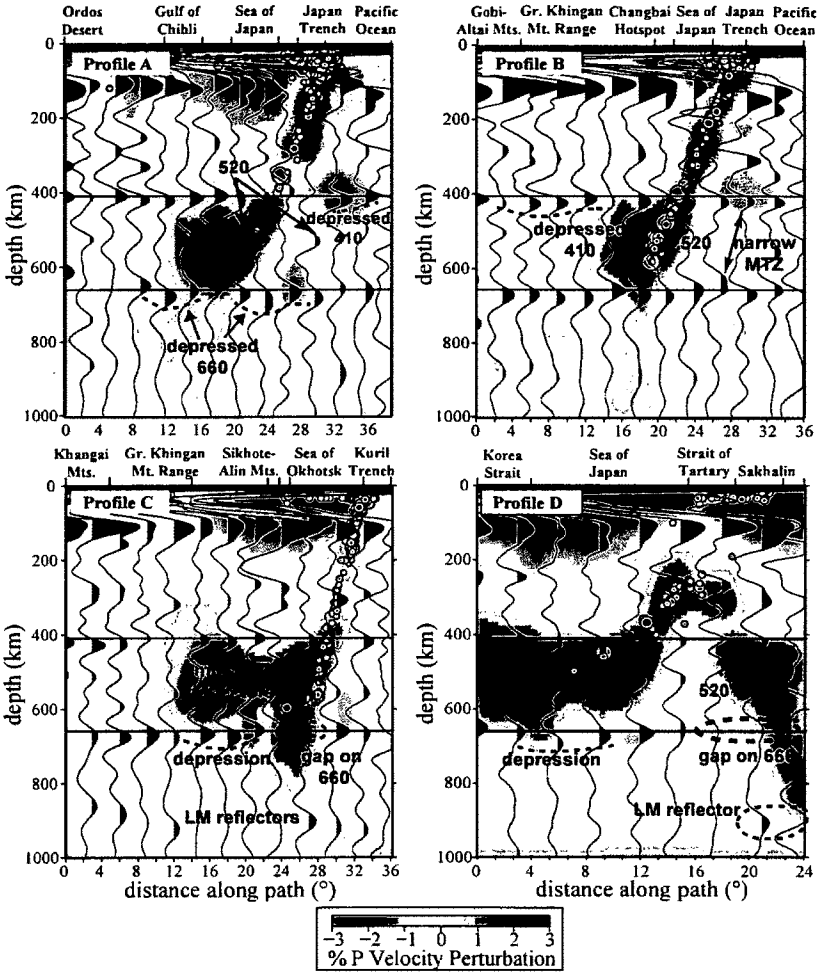

Figure 2.4: Interpolated reflection stacks along Profiles A to D (see Figure 2.2) superimposed on high-resolution P-wave velocities from Obayashi et al. (2006). The magenta circles show the earthquakes within the averaging window of each profile and the sizes of the circles scale with event magnitudes. Seismic activity extends down to 650 km and outlines the Wadati-Benioff zone in the northwestern Pacific region. Key observations are encircled or highlighted by dotted lines and arrows.

Profile A (see Figure 2.4) shows highly undulating MTZ boundaries between the Pacific Plate and the volcanic arc near central Honshu Island. The 410 east of the Japan trench undergoes 15-20 km local depression relative to the cross-sectional average of 413±5

km. This 500-km wide HRZ reaches the maximum reflection amplitude of ~8% beneath central Honshu arc and overlaps with a P wave low-velocity zone between 380 and 400 km depths (Obayashi et al., 2006; Bagley et al., 2009; Li and van der Hilst, 2010; Zhao and Ohtani, 2009). The reflection characteristics change sharply towards the Wadati-Benioff zone, where the 410 elevates to ~395 km but loses 3-4% amplitude (see Figure 2.4, Profile A). Complex reflective structures are also evident at the base of the MTZ east of Japan trench. The 660 shows 25+ km peak-to-peak topography and the undulations negatively correlate with those of the 410 along trench dip. A deep 660 is observed beneath eastern Sea of Japan (~684 km) and Gulf of Chihli (~675 km), whereas the area in between shows an average or shallow 660 (see Figs. 2.3c and 2.4).

The shape of the high-velocity structure becomes quasi-linear near northern Honshu where a significant number of deep-focus earthquakes have been recorded (Figure 2.4, Profile B). The 410 remains depressed oceanward from the Wadati-Benioff zone, while a strong HRZ at ~300 km depth approximately marks the top of a P-wave low-velocity zone above the MTZ. The reflection characteristics of the 410 in this region are generally consistent with those from central Honshu arc (see Profile A), but the amplitude and depth variations are visibly diminished. A strong 660 is detected at ~645 km depth beneath northern Honshu, which reduces the MTZ width to ~225-km along trench dip (see Figure 2.4, Profile B). Further west, the reflectivity profiles shows a broad depression beneath Sea of Japan and Changbai hotspot. This mild depression zone overlaps with high P velocities near the base of the MTZ, but appears wider than that expected from 1+% P velocities.

The high-velocity zone beneath Kuril arc (Figure 2.4, Profile C) is more complex than those within the two southern profiles. Above-average P velocities extend to depths below 750 km along trench dip and across exceptionally weak 410 and 660 (hereafter, 'reflection gap') within the Wadati-Benioff zone. The base of this anomaly, which is interpreted as 0.3-0.5% P velocity perturbations, is underlain by an eastward dipping lower-mantle reflector at ~900 km depth (see also Figure 2.3d) in the vicinity of the reflection gap. The strength of the 660 gradually increases toward Sikhote-Aline Mountains and effectively outlines the

1+% P velocity zone in the lower half of the MTZ (see Figure 2.4, Profile C).

A southwest-northeast transect over the deepest part of the Wadati-Benioff zones (Figure 2.4, Profile D) highlights the key reflectivity differences between Japan and Kuril subduction systems. South of Hokkaido corner, large-scale high-velocity structures are mainly confined to the MTZ. Despite slightly reduced amplitudes, the MTZ phase boundaries are laterally continuous and the base of the MTZ between Korea Strait and Sea of Japan shows 30+ km depressions relative to the global average. Across southern Kuril arc, however, the amplitude of the 660 falls below noise level within a localized lower mantle high-velocity zone. As suggested by Profile C, the base of the northward dipping high-velocity structure partially overlaps with a strong reflector at 900-930 km depths (see Figure 2.4, Profile D).

A common link between Japan and Kuril subduction zones is the presence of reflectors within the MTZ (see Figs. 3B and 4). We identify a single HRZ with maximum amplitudes in excess of 6% at ~525 km within the Wadati-Benioff zones in the two southern profiles. Two distinct reflectors are further detected across southern Kuril arc in the depth ranges of 500-530 km and 580-600 km (see Figure 2.4d), and their amplitudes increase in the northward direction.

2.3 Discussion and interpretations

The effectiveness of SS precursors in resolving local or regional length-scale structures has been underscored by recent studies of subduction zones (Heit et al., 2010; Schmerr and Garnero, 2007), hot mantle plumes (Cao et al., 2011; Gu et al., 2009; Schmerr and Garnero, 2006) and crust (Rychert and Shearer, 2009). Despite concerns over Fresnel zone size and shape (Chaljub and Tarantola, 1997; Neele et al., 1997), shear waves such as SS precursors are capable of recovering structures at length scales beyond their 'nominal' resolution, especially when waveform information is incorporated (Ji and Nataf, 1998; Mégnin and Romanowicz, 2000). Major HRZs reported in this study are minimally affected by mod-

erate changes to the CMP sizes and shapes. For example, the semi-linear structure across northern Honshu Islands and large lateral-scale depressions west of the Hokkaido Corner are consistently captured by reflection maps constructed based on CMP areas of $12^{\circ 2}$ and $50^{\circ 2}$ (Figure 2.5), despite instabilities associated with limited data traces in smaller CMPs (Figure 2.5a) and over-smoothing in the case of larger averaging areas (Figure 2.5b). Our heuristically determined averaging area of $24^{\circ 2}$ represents a reasonable compromise between image stability and resolution.

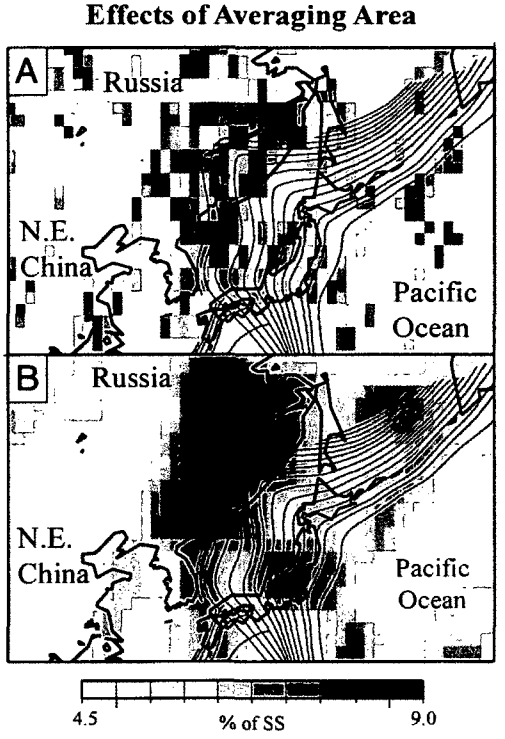

Figure 2.5: A comparison of depth-converted reflection amplitudes at 680-km depth based on averaging CMP gathers of (a) $2° \bullet 6° = 12°^2$, and (b) $5° \bullet 10° = 50°^2$. The numbers on the left side of the equations are the dimensions (in arc deg) of the CMP gathers along section-parallel and section-perpendicular directions, respectively. The right side of the equation indicates the uniform CMP area for each experiment. Significant scatter in Figure 2.5a suggests instability associated with limited numbers of traces in some CMP gathers, while the results in Figure 2.5b suffers from over-smoothing. The main reflective structures such as strong depressions near the deepest part of the Wadati-Benioff zone are consistent between these maps.

2.3.1 Average reflection amplitudes

The detectable ranges of amplitudes are 4-9% for $S_{410}S$ and 4-12% for $S_{660}S$. The former range overlaps with the predicted values of ~8% from PREM (Dziewoński and Anderson, 1981) and the global average of 6.7% from SS precursors (Shearer, 1996), but the latter

range falls well short of 14% based on PREM (Shearer, 2000). These individual amplitude estimates are strongly affected by the strength of SS, the normalizing reference phase. For instance, the presence of attenuating low-velocity structures (*e.g.*, Huang and Zhao, 2006; Lei and Zhao, 2005; Zhao, 2001; Zhao et al., 1992; Zhao et al., 2007), especially near back arc regions (*e.g.*, Roth et al., 1999, 2000; Xu and Wiens, 1997; Zhao, 2001), could diminish SS and increase the relative amplitude of S_dS. Compositional variations associated with Al at the base of upper mantle (Deuss, 2009; Deuss and Woodhouse, 2002; Weidner and Wang, 1998; Weidner and Wang, 2000) or Fe content (Agee, 1998; Akaogi et al., 2007; Inoue et al., 2010) are also known to broaden phase boundary widths and reduce precursor amplitudes. A more stable parameter is the amplitude ratio between the 410 and the 660 (*e.g.*, Shearer, 2000), which we estimate to be within the range of 0.7-0.8. This value is slightly higher than the earlier estimates of 0.64-0.68 based on global SS precursors (Shearer, 1996) and regional ScS observations (Revenaugh and Jordan, 1991), though it is in poor agreement with that of PREM (0.5). A regionally sharp 410 (Ai and Zheng, 2003; Benz and Vidale, 1993; Jasbinsek et al., 2010; Melbourne and Helmberger, 1998; Neele, 1996; Vidale et al., 1995) is possible but requires a quantitative analysis of the waveforms, particularly those prior to phase equalization. Additionally, since the average observed topography on the 660 is 25-30% larger relative to the 410 (see Figure 2.3 and Figure 2.4), defocusing and energy loss due to incoherent stacking (Shearer, 2000) would be more severe for reflections from the 660.

2.3.2 Depth correlation of the 410 and 660

The depth-converted reflectivity profiles of this study offer new insights on the effect of mantle temperatures on the phase transition depths. For olivine-rich mantle compositions, the depths of the 410 and 660 should anticorrelate based on results of high-pressure laboratory experiments (*e.g.*, Akaogi et al., 2007; Helffrich, 2000; Irifune et al., 1998; Ita and Stixrude, 1992; Katsura and Ito, 1989) as well as high-frequency seismic observations in the northwestern Pacific region (*e.g.*, Ai and Zheng, 2003; Collier et al., 2001; Li et al., 2000;

Ramesh et al., 2005; Saita et al., 2002; Tonegawa et al., 2006; van der Meijde et al., 2005). However, global surveys of the spectral contents and amplitudes of these two phase boundaries have often attributed a locally thick MTZ to a highly deformed 660 at the base of the upper mantle (Flanagan and Shearer, 1998; Gu and Dziewoński, 2002; Gu et al., 1998, 2003; Houser et al., 2008). The depth of the 410 remains problematic in view of expected phase boundary behavior (*e.g.*, Deon et al., 2011; Du et al., 2006; Fee and Dueker, 2004; Gilbert et al., 2003; Gu and Dziewoński, 2002; Gu et al., 2003; Schmerr and Garnero, 2007; Tauzin et al., 2008) and prompted additional assumptions involving MTZ velocity corrections (Deon et al., 2011; Flanagan and Shearer, 1998; Gu et al., 2003; Houser et al., 2008; Schmerr and Garnero, 2006) and/or mechanisms predicated on extensive compositional variations (Deon et al., 2011; Gu et al., 2009; Houser and Williams, 2010; Schmerr and Garnero, 2007).

Our migration results enable a careful examination of the correlation between temperature and discontinuity topography in the northwestern Pacific region. An excellent test case is Profile A in which both discontinuities are laterally continuous and exhibit strong topography (Figure 2.6). The peak-to-peak depth variations of the 410 and 660 are approximately 30 km and 40 km, respectively, both exhibiting large deformation from the trench onset to the deepest part of the Wadati-Benioff zone across southern Japan (Figure 2.6a). A simple bin-to-bin correlation, which implicitly assumes vertical continuity of seismic velocities, yields a small positive correlation. To account for non-vertical structures following the slab dip ($\sim$30°, Gudmundsson and Sambridge, 1998), we revise the correlation analysis by introducing an offset such that the depth of the 410 at a given location is correlated with that of the 660 at a location $\sim$200 km further inland. The 'dip-corrected' phase boundaries show a clear negative correlation in the vicinity of the slab (see Figure 2.6a) that favors a thermal origin for the observed shape of the MTZ. The negative correlation benefits from an anomalously shallow 410 within the Wadati-Benioff zone, which is a notable departure from earlier findings of global time-domain analyses of SS precursors (*e.g.*, Flanagan and Shearer, 1998; Gu et al., 2003).

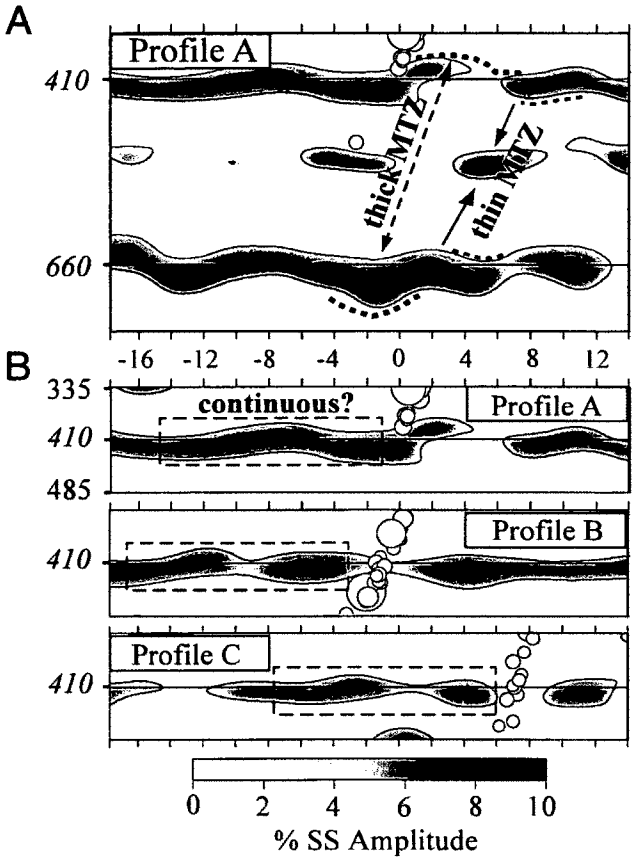

Figure 2.6: (a) A subsection of the migrated reflectivity along Profile A. The gray circles mark the locations and sizes of deep earthquakes along the profile (see Figure 2.4 for details). The contours superimposed on the shaded reflection amplitudes are taken at 4% and 8% values. (b) Magnified subsections of reflection amplitude near the top of the MTZ for all three profiles. The highlighted region shows a relatively continuous 410 above the stagnant part of Honshu slab.

2.3.3 Continuity of the 410

There have been considerable discussions of the existence of, and support for, a water/melt rich layer near the top of the MTZ (Frost and Dolejs, 2007; Inoue et al., 1995; Inoue et al., 2010; Kohlstedt et al., 1996; Smyth and Frost, 2002; Wood, 1995). Wadsleyite has a strong capacity to accommodate hydroxyl (OH single bond) and can store up to 3 wt.% H_2O under

equilibrium conditions (Frost and Dolejs, 2007; Inoue et al., 1995; Inoue et al., 2010; Wood, 1995). These laboratory-based measurements have been supported by regional (*e.g.*, Revenaugh and Sipkin, 1994; Schaeffer and Bostock, 2010; Schmerr and Garnero, 2007; Zheng et al., 2007) and global (Deuss, 2009; Gu et al., 2009; Tauzin et al., 2010) seismic observations that require explanations beyond temperature. Mechanisms involving the infiltration of hydrous melt are elucidated further by geodynamical calculations and syntheses (*e.g.*, Bercovici and Karato, 2003; Billen, 2008; Karato, 2006; Leahy and Bercovici, 2007, 2010).

Our migrated reflectivity structures provide further constraints on this hypothesized hydrous layer. The 410 west of the Wadati-Benioff zone (Figure 2.6b) is consistently shallower than the regional average in this study. The largest topography is observed in the southernmost cross-section, reaching a depth of ~400 km beneath Korea and northeastern China. The two northern profiles B and C show modest highs of ~410 km near Great Khingan Range and Sikhote-Alin Mountains, respectively, and the average amplitudes of the 410 in all three profiles well exceed the regional averages (see Figure 2.6b). These characteristics are reminiscent of those reported beneath Tonga subduction zone (Zheng et al., 2007) where a hydrous layer is suggested to reside atop the 410. While the highlighted region (see Figure 2.6b) is farther away from the Wadati-Benioff zone than the target area in Zheng et al. (2007), metasomatism involving slab-derived fluids rising through the flattened part of slabs (Fukao et al., 2001; Fukao et al., 2009; Zheng et al., 2007) could give rise to intraplate volcanoes near Changbai Mountain and Wudalianchi (Huang and Zhao, 2006; Lei and Zhao, 2005; Zhao, 2001; Zou et al., 2008).

Based on multiple cross-sections in South America, Schmerr and Garnero (2007) inferred a 'melt lens' from evidence of delayed and split/missing $S_{410}S$ east of the Nasca-South America convergent zone. A wide 410 reflection gap is corroborated by Contenti et al. (2012) based on SS precursors and the same imaging technique presented in this study, but the associated $S_{410}S$ waveforms from South America are much more complex than those shown in this study. If a fluid-rich layer exists atop the MTZ, its spatial scale, infiltration/storage mechanism and/or chemistry (*e.g.*, Richard and Iwamori, 2010) beneath

the Pacific Northwest would most likely differ from those beneath Tonga and South America.

2.3.4 Slab stagnation and distortion

Subducted ocean basins in the western Pacific region have been known to deflect to a near-horizontal direction at the MTZ for nearly two decades (Fukao et al., 1992; Okino et al., 1989; van der Hist et al., 1991). Since these early reports, ample evidence of slab stagnation (Fukao et al., 1992; Fukao et al., 2001) has been provided by global and regional tomographic images (Fukao et al., 2001; Fukao et al., 2009; Li and van der Hilst, 2010; Sugioka et al., 2010; Zhao and Ohtani, 2009), as well as by anomalous dip-angle variations in the distribution of intermediate-depth earthquakes (Chen et al., 2004). The conditions and characteristics of stagnant slabs were constrained further by recent numerical calculations that incorporated thermo-petrological buoyancy forces (Bina and Kawakatsu, 2010; Bina et al., 2001; Tetzlaff and Schmeling, 2000), rheology (Billen, 2008, 2010; Billen and Hirth, 2007) and plate history and rollback (Christensen, 2001; Nakakuki et al., 2010; Tagawa et al., 2007; Torii and Yoshioka, 2007; Zhu et al., 2010).

With the help of seismic velocities, the reflectivity information provided by our study can place crucial constraints on slab deformation at the base of the MTZ and the shallow lower mantle. Our observations suggest reduced topography on the 660 in the northward direction (see Profiles A and B in Figure 2.4), which is consistent with earlier findings based on receiver functions (Niu et al., 2005) and postcursors of sScS (Yamada et al., 2009). A 'soft' slab under the influence of trench migration and rollback may be possible beneath northern Honshu arc (Li et al., 2008). However, for the same region Li et al. (2008) detected little or no oceanward broadening of the 660 from high-resolution S to P converted waves. This result is inconsistent with the observed shift in this study between the high-velocity zone and the onset of the broad depression in the vicinity of the island arcs (see Figure 2.4 and Figure 2.6a). While resolution differences between SS precursors and receiver functions may play a role, the 100-300 km horizontal broadening of the 660 in the oceanward direction could be caused by slab 'pile-ups' at the base of MTZ.

A more intriguing observation from the two southern profiles is two distinct zones of large lateral scale depression: 1) near the piercing point of the slab at the base of MTZ, and 2) in the western half of the stagnant slab (*e.g.*, Fukao et al., 2009; Huang and Zhao, 2006). These two basins are nearly identical in shape, and the depth of the 660 between them is raised sharply to 655-660 km. By assuming a reference discontinuity depth of 670 km, we estimate the horizontal dimensions of the depression zones (Seg 1 and Seg 3) to be 350-450 km in Profile A (Figure 2.7a) and 550-600 km in Profile B (Figure 2.7b). The respective phase boundary elevations between the basins are roughly estimated to be ~600 km and ~350 km, rendering a total length of ~950 km (*i.e.*, Seg 2 + Seg 3) for both profiles beyond the slab piercing point at the 660. This value falls within an estimated length of 800-1000 km for deflected slabs (Fukao et al., 2009; Huang and Zhao, 2006), though true length could be slightly smaller due to the effect of spatial averaging. The flat part of the slab, which is expected to reside on the 660, is no wider than 600 km.

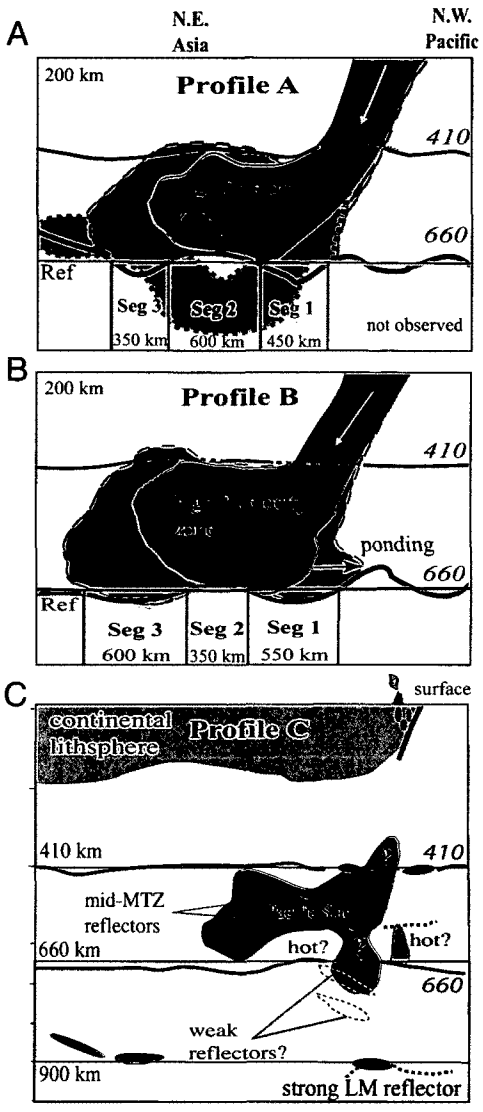

Figure 2.7: The observed depths of the 410 and 660 beneath Profiles A-C with interpretations. The undulations on the 410 and 660 have been exaggerated by a factor of 2 from the original observations presented in Figure 2.4. The short dashed lines mark regions of low reflection amplitude and the white arrows indicate the dip of the Wadati-Benioff zones. The region shaded in blue shows 1% P velocity perturbations from Obayashi et al. (2006), and the regions shaded in green (see Profiles A and B) represent interpreted MTZ low-temperature regimes based on the observed SS precursor amplitudes of this study. Three distinct sub-regions at the base of the upper mantle are labeled Seg 1-3. Their dimensions are estimated based on a reference depth of 670 km and rounded to the nearest 50 km. In Figure 2.7a, the region shaded in gray shows the shape of a stagnant slab from recent numerical simulations that consider temperature- and pressure-dependent viscosity (edited from Figure 2.12 of Fukao et al., 2009 and Figure 2.4 of Nakakuki et al., 2010).

The shape of the 660 raises new questions about the 'flatness' (Okino et al., 1989) of stagnant slabs. The observation of contention is the average or shallow 660 between the two distinct basins, which implies a significant temperature/compositional gradient leading to the center of the stagnating slab segment. This observation is inconsistent with the broad depressions reported earlier based on seismic tomography (see Fukao et al., 2009) and reflection depth/MTZ thickness imaging (*e.g.*, Flanagan and Shearer, 1998; Gu et al., 1998, 2003; Houser et al., 2008; Lawrence and Shearer, 2006; Shearer and Masters, 1992). The amplitude of the 660 within this uplifted region (see Seg 3, Figure 2.7a and B) is higher than the regional averages, which may be interpreted as a narrow ringwoodite to perovskite and magnisiowustite phase loop at temperatures above the geotherm. Formations of twin basins on the 660 are plausible according to geodynamical calculations of slab geometry that incorporated trench retreat (Christensen, 1996; Tagawa et al., 2007; Zhu et al., 2010) or temperature- and pressure-dependent viscosity (see Figure 2.12 of [Fukao et al., 2009] and [Karato and Wu, 1993]). These calculations suggest a deep 660 at the slab piercing and MTZ re-entry points, between which the phase boundary remains nearly unperturbed (see Figure 2.7a). While the horizontally oriented, lower-mantle slab segment in Figure 2.7a (*e.g.*, Christensen, 1996; Fukao et al., 2009; Tagawa et al., 2007) is not convincingly supported by our SS precursor observations, buckling (Bayly, 1982; Ribe et al., 2007) is plausible due to interactions between the tip of the descending slab and the viscous lower mantle (*e.g.*, Kellogg et al., 1999; Obayashi et al., 2006). During these episodes, entrapped ambient mantle material could form isolated, higher-temperature pockets within a highly deformed stagnant slab. Trench migration and rollback history (Christensen, 1996; Schmid et al., 2002), water (*e.g.*, Huang and Zhao, 2006; Inoue et al., 1995; Inoue et al., 2010; Kohlstedt et al., 1996; Litasov et al., 2006; Ohtani et al., 2001; Suetsugu et al., 2006; van der Meijde et al., 2003), grain-size reduction (*e.g.*, Billen, 2010; Nakakuki et al., 2010), and possible separation of oceanic crust from the descending lithosphere (Hirose et al., 1999; Hirose et al., 2005; Irifune and Ringwood, 1993; van Keken et al., 1996) could all contribute large internal gradients on the 660 within the 'flat' part of the slab.

2.3.5 Slab penetration beneath southern Kuril arc

The reflectivity structures shed new light on the long-standing debate about the depth of slab in the Pacific Northwest (Fukao et al., 1992; Fukao et al., 2001; Fukao et al., 2009; van der Hist et al., 1991; van der Hilst et al., 1997). While the vertical extent of slabs and the general style of mantle convection remain debated on the global scale, there is growing evidence of scattered and deformed slab material in the lower mantle (Bijwaard et al., 1998; Chang et al., 2007; Courtier and Revenaugh, 2008; Fukao et al., 2001; Fukao et al., 2009; Li and van der Hilst, 2010; Obayashi et al., 2006; van der Hilst et al., 1997).

Among the various HRZs documented in this study, sub-MTZ anomalies in Profiles C and D present the best arguments for slab penetration into the lower mantle. The most visible change from central Honshu to southern Kuril arcs is the reflection amplitude reduction of both the 410 and the 660, highlighted by apparent reflection gaps in the northernmost transect. These gaps coincide with the Wadati-Benioff zone of the Kuril slab (Figure 2.7c) and their origins remain enigmatic. For instance, increasing Al content could broaden the depth range of garnet-to-perovskite transformation and influence olivine and pyroxene normative proportions near the base of the upper mantle (Gasparik, 1996; Weidner and Wang, 1998). This scenario is plausible when majorite garnet transforms to metastable ilmenite and, eventually, to Ca-perovskite (*e.g.*, Weidner and Wang, 1998; Weidner and Wang, 2000) in subduction zones. The presence of Al-bearing akimotoite could introduce further complexities, such as a high velocity layer or a steep velocity gradient, to mid MTZ depths at low temperatures (Gasparik, 1996; Wang et al., 2004). However, changes in Al content mainly impact mantle reflectivity structure under mid-to-lower MTZ pressure-temperature conditions (*e.g.*, Tateno et al., 2005; Wang et al., 2004; Weidner and Wang, 2000), which fails to explain the weak 410 within the Kuril slab (see Figure 2.4, Profile C and Figure 2.7c). Alternatively, increasing Fe concentration could substantially broaden the phase loops of both olivine-wadsleyite and ringwoodite to perovskite and magnisiowustite transitions (Akaogi et al., 2007; Deon et al., 2011; Inoue et al., 2010; Litasov et al., 2006), thus reducing the reflection amplitudes of both discontinuities. Observational support for Fe enrichment in

subduction zones (Agee, 1998; Zou et al., 2008) remains insufficient.

Water transported into the MTZ by slabs could potentially modify the impedance contrast, and hence the visibility of a reflecting body (Fukao et al., 2009; Ichiki et al., 2006; Ohtani and Sakai, 2008; van der Meijde et al., 2003). Aided by the strong inclinations of wadsleyite and ringwoodite to retain water (Bercovici and Karato, 2003; Inoue et al., 1995; Kohlstedt et al., 1996; Fukao et al., 2009), a hydrous MTZ can simultaneously affect the width and depth of the 660 (Akaogi et al., 2007; Inoue et al., 2010; Litasov et al., 2006). The effect of water on the phase loop of olivine-Wadsleyite transition is, unfortunately, both complex and weaker than expected based on 1 wt.% H_2O inclusion (Inoue et al., 2010). A larger amount of water is likely required within the descending slab to diminish the amplitude of $S_{410}S$ beyond the detection threshold. Recent seismic observations (Bina and Kawakatsu, 2010; Fukao et al., 2009; Suetsugu et al., 2006; Suetsugu et al., 2010) have generally favored 'dry' (*e.g.*, < 0.5 wt. H_2O, (Suetsugu et al., 2006; Suetsugu et al., 2010) slabs in various subduction zones along the western Pacific plate boundaries, however. In addition, the 660 appears to be locally elevated, despite a diminutive amplitude, which is at odds with the expected effect of water in the MTZ (Billen, 2008; Litasov et al., 2006).

Aside from minerological explanations, the observed reflection gaps are most definitely affected by wave optics. Similar to the scattering of light, the stacked amplitudes of the underside SH-wave reflections are sensitive to the geometry of the reflecting surface. For instance, a dipping structure or interface can easily cause defocusing or scattering, depending on the size of the structure relative to the wavelength of the incoming wave (Chaljub and Tarantola, 1997). Deconstructive wave field interference from multiple reflectors could further reduce the perceived strength of the 660. Within low-temperature slabs, garnet-ilmenite-perovskite transitions (*e.g.*, Akaogi et al., 2002; Vacher et al., 1998; Weidner and Wang, 1998; Weidner and Wang, 2000) have been suggested to take place over a depth range of 60-100 km at the base of the MTZ (Akaogi et al., 2002; Vacher et al., 1998). Observationally, multiple reflectors have been reported under different tectonic settings (*e.g.*, Ai and Zheng, 2003; Deuss and Woodhouse, 2002; Schmerr and Thomas, 2011; Tibi et al.,

2007), but remain questionable beneath the western Pacific region (Lebedev et al., 2002c; Niu et al., 2005; Tonegawa et al., 2006). In this study, only the Kuril profile (see Figure 2.4c and d) hinted at subtle reflectors with 4-5% amplitudes at ~700- and 780-km depths along slab dip (see Figure 2.7c).

The presence of a robust lower-mantle HRZ beneath Kuril slab (see Figure 2.7c) lends further support for a deep Kuril slab. Phase transitions of Ca-perovskite (Stixrude et al., 2007), metastable garnet (Kawakatsu and Niu, 1994; Kubo et al., 2002), stishovite (Hirose et al., 2005; Ohtani, 2005), as well as transformations of dense hydrous magnesium silicates under lower-mantle pressure-temperature conditions (Ohtani, 2005; Ohtani et al., 2001; Richard et al., 2006; Shieh et al., 1998), are possible origins of the observed lower-mantle reflectors (*e.g.*, Kaneshima and Helffrich, 1999, 2003; Niu et al., 2003). A slightly weaker lower-mantle HRZ in the depth range of 850-1000 km away from active subduction (see Figure 2.4a and 2.7c) remains enigmatic.

2.3.6 Other HRZs and their potential origins

Two additional reflection signals from this study could have significant implications if confirmed. First, we identify one (across Honshu arc) or more (across southern Kuril arc) reflectors with amplitudes ranging from 5% to 9% within the MTZ (see Figure 2.3b, 2.4 and 2.7). The peak locations generally reside within the descending slab, with the notable exception of a strong 520 east of the Wadati-Benioff zone beneath central Honshu island (see Figure 2.3a) The origins of MTZ reflective structures or velocity gradients remain controversial, though their existence has long been documented in the study region based on travel times (Fukao, 1977). It was later proposed to be a weak global seismic discontinuity from studies of SS precursors (Shearer, 1990, 1991b), despite suggestions of artifacts associated with low-frequency side-lobes of $S_{410}S$ and $S_{660}S$ (Bock, 1994). Highly undulating MTZ reflectors received further support from reflected and converted body waves (Chevrot et al., 1999; Deuss, 2009; Deuss and Woodhouse, 2002; Flanagan and Shearer, 1998; Gossler and Kind, 1996; Gu et al., 1998, 2003; Lawrence and Shearer, 2006; Shearer, 1996; Shen

et al., 2008), and were generally attributed to wadsleyite to ringwoodite (Bina, 2003; Helffrich, 2000) and garnet to Ca-perovskite (Ita and Stixrude, 1992) phase changes. Within subduction zones, these two transformations likely occur at different MTZ depths (Saikia et al., 2008) and manifest into distinct reflectors (Deuss, 2009; Deuss and Woodhouse, 2002) resembling those detected below southern Kuril arc in this study. Alternative explanations include a delayed meta-stable olivine phase transition (Bina and Kawakatsu, 2010; Iidaka and Suetsugu, 1992; Jiang et al., 2008; Chien-Min, 1976), water within slabs (*e.g.*, Inoue et al., 1995; Inoue et al., 2010; Koyama et al., 2006; Lawrence and Shearer, 2006) and a flat garnetite layer (Shen et al., 2008). A combination of these mechanisms may be responsible for the different signatures in the Honshu (a single 520 reflector) and Kuril (multiple MTZ reflectors) profiles.

Finally, a narrow MTZ and a series of strong HRZs (see Figure 2.4 and Figure 2.7) suggest reduced MTZ temperatures east of the Wadati-Benioff zone. This interpretation is supported by recent studies of ScS reverberations (Bagley et al., 2009; Revenaugh and Jordan, 1991), seismic tomography (Huang and Zhao, 2006; Obayashi et al., 2006; Zhao and Ohtani, 2009), and electrical conductivity (Ichiki et al., 2006). The large reflection amplitudes of these reflections (8-12% of SS) likely require compositional variations associated with a residual thermal plume from the past 130 Ma (Honda et al., 2007; Ichiki et al., 2006; Miyashiro, 1986; Obayashi et al., 2006; Zhao and Ohtani, 2009; Zou et al., 2008).

2.4 Conclusions

Key conclusions from our study of SS precursors sampling the northwestern Pacific subduction zones are:

1. The depths of the 410 and 660 are negatively correlated if slab dip is considered, especially beneath central Honshu arc. The MTZ olivine phase boundary variations are mainly governed by temperature.

2. The Pacific plate stagnates across central Honshu island at MTZ depths, but the center of the stagnant slab appears to be strongly deformed or buckled near the base of the upper mantle, *i.e.*, the stagnant slab may not be as flat as previously suggested. Eastward broadening of the 660 is likely due to slab 'pile-ups'.

3. The Pacific plate extends below the transition zone across southern Kuril arc. Major mass and heat fluxes and possible compositional variations are expected near the slab piercing point.

4. Strong reflectors exist within/near the descending slabs at mid MTZ and lower mantle depths.

From a technical standpoint, the results presented in this study provide a glimpse of the future for regional-scale analysis based on intermediate-period SS precursors. Increasingly diverse applications in recent years have underlined the remarkable resolving power of this data set, one that was traditionally tapped as a 'low resolution' constraint on mantle structure. This trend will continue in the foreseeable future, especially in view of the growing number of global seismic networks and applications of array methods.

CHAPTER 3

The Radon transform[1]

Conventional methods in precursor analysis are unable to reliably, robustly and accurately constrain mantle structure from P'P' precursors. This has necessitated the adaptation of more sophisticated signal processing techniques for my purposes, one of which is the RT. I developed two Matlab routines to perform the forward and inverse RTs, which are now publicly available. In this chapter I will elaborate on the properties of the transform as well as specifics to this implementation.

The RT was originally formulated as an integration of a 2D function along a set of straight lines expressed by orientation angles and distances to the origin (Radon, 1917). This problem has since been extended to more general functions and laid the foundation for applications in astrophysics (Bracewell, 1956), computed axial tomography (Cormack, 1963), seismic tomography (Liu and Gu, 2012) and reflection seismology (Sacchi and Ulrych, 1995; Trad et al., 2003). More recently, earthquake-based seismic structure analysis also utilized RT in both traditional (An et al., 2007; Gu et al., 2009; Gu and Sacchi, 2009) and more generalized (Cao et al., 2010) forms. Within the context of seismology, the integration paths are typically constrained by ray parameter (alternatively called slowness and denoted by p),

[1] A version of this chapter has been accepted for publication (Schultz and Gu, 2012a, Computers and Geosciences).

a conserved quantity along a potentially curved trajectory in a heterogeneous medium. Some applications may adopt the form

$$t = \tau + p\Delta, \tag{3.1}$$

where seismic arrival time (t) is linearly dependant on epicentral distance (Δ). The ability of RT to project move-out (spatial) data $M(t, \Delta)$ to the Radon domain $R(\tau, p)$ allows for the identification and differentiation of unique phase arrivals. Extraneous arrivals may be conveniently isolated and attenuated in the Radon domain. The forward operator can also be applied to a filtered Radon domain, effectively minimizing obfuscating phases in the spatial domain. This property has been instrumental in exploration seismology for the removal of multiple reflections (Thorson and Claerbout, 1985; Hampson, 1986; Beylkin, 1987). With the advent of increasingly dense regional seismic arrays (*e.g.*, USArray and Hi-Net, Japan) as well as convenient access and dissemination of geophysical data, it is becoming more feasible to extend techniques such as RT to interrogate reflectivity structure at global or regional scales (An et al., 2007; Gu et al., 2009).

In this chapter I document the theory, implementation and usage of Radon_inverse and Radon_forward, two open-source Matlab-based routines. I designed these functions under the premise of simplicity and flexibility, consistent with the built-in Matlab functions (*e.g.*, fft and interp1). Radon_inverse implements a frequency-based inversion and includes regularization methods pertaining to ℓ_2 and ℓ_1 norms as well as a Cauchy-based (Sacchi and Ulrych, 1995) cost function. Both the forward and inverse routines include linear and parabolic path functions, and the ambitious user may incorporate additional path functions, regularizations or inversion techniques as needed. The routine's functionality has been tested on long-period shear wave reflections from mantle interfaces (Shearer and Masters, 1992) and high-frequency receiver functions (Rondenay, 2009). This method and algorithm remain general and are easily adaptable to other applications, both within and outside of seismology.

3.1 Theory

RT represents an integral transform that in its original context described an integration along lines parameterized by distance to the origin and angular orientation. This parameterization leads to Radon inversions commonly referred to as sinograms in computed axial tomography. In seismology, discrete approaches to this problem have been estimated using a summation known as slowness slant stacking. The equation governing the summation-based approximation to the Radon domain (vespagram) is expressible as

$$R(\tau_k, p_i) = (1/N_\Delta) \sum_{j=1}^{N_\Delta} M(\tau_k + T(p_i, \Delta_j, \delta), \Delta_j). \tag{3.2}$$

For each parameter of slowness p_i, a summation is performed over all seismograms with offsets/distances Δ_j in the move-out domain. Each seismogram is shifted in time by the function $T(p_i, \Delta_j, \delta)$ that describes the path of integration in the spatial domain. Coherent signals along these paths (see Figure 3.1) will stack constructively and potentially increases signal-to-noise ratio by a factor of $\sqrt{N_\Delta}$ (Shearer, 1991b), where N_Δ is the number of seismograms. Integration methods are distinguished by their path function as linear, parabolic, hyperbolic or generalized. In this path function formulation, a phase's intersection in time with the distance parameter δ determines the τ arrival in the Radon domain.

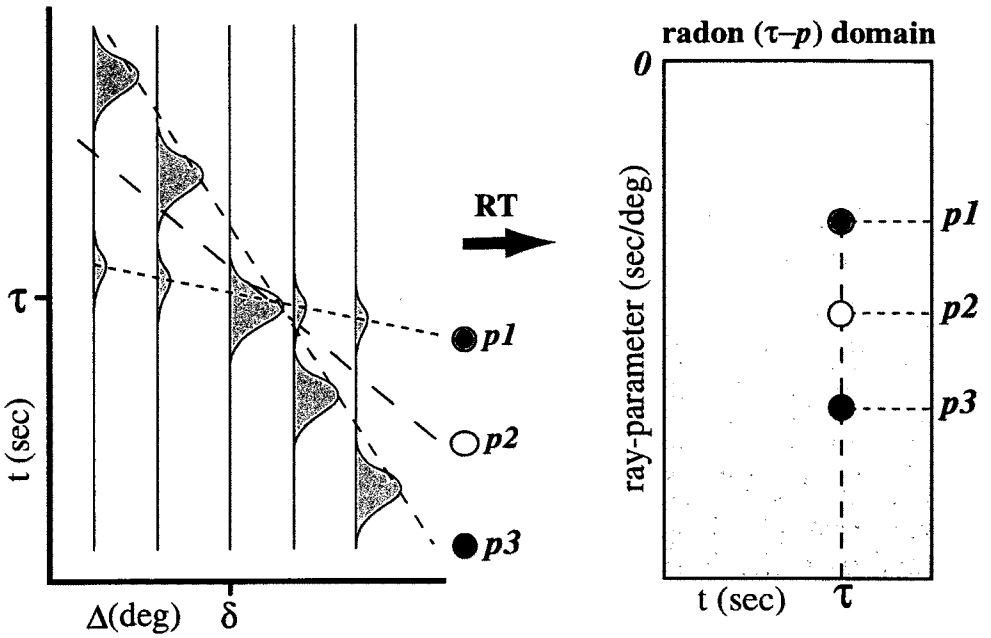

Figure 3.1: Schematic diagram depicting the Radon transform. Linear path-functions are focused around the distance parameter δ in the spatial domain (left panel). Integration paths defined by ray parameters p1, p2 and p3 intersect in the spatial domain at (τ, δ) (left panel), which are projected to the Radon domain as energy foci (right panel). Integration along ray parameter p3 maps the high-amplitude phase in the spatial domain to an energetic signal in the Radon domain (dark solid circle). A weaker Radon signal results from integrating along parameter p1 (gray circle, right panel), due to smaller amplitude phase move-out, while an integration path devoid of arrivals (see p2) yields minimal Radon energy (white circle). It should be noted that these three paths only intersect at the designated distance parameter δ, whereas any other choice would result in distinct τ arrivals in the Radon domain.

Slant stack methods (Rost and Thomas, 2009) offer a simple, effective technique to estimate the Radon domain. Other non-linear stacking techniques such as N-th root (Kanasewich et al., 1973) and phase-weighted (Schimmel and Paulssen, 1997) have been employed with slowness slants to detect coherent, low amplitude arrivals and increase slowness resolution. However, these alternatives tend to distort the signal's amplitude information, a potentially fatal flaw for some applications. Inversion-based methods have been suggested as

a more robust and reliable approach (Beylkin, 1987; Sacchi and Ulrych, 1995). Formulating RT as an inverse problem requires the forward relationship between the spatial and Radon domains

$$M(t_k, \Delta_j) = \sum_{i=1}^{N_p} R(\tau_k - T(p_i, \Delta_j, \delta), p_i). \tag{3.3}$$

To condition equation (3.3) into a form that is conducive to inversion, I perform the Fourier transform

$$M(\omega_k, \Delta_j) = \sum_{i=1}^{N_p} exp(-i\omega_k T(p_i, \Delta_j, \delta)) R(\omega_k, p_i), \tag{3.4}$$

where the shift theorem modifies the discrete Radon equation into a more tractable form. For a single, constant frequency ω_k, this equation may be expressed in matrix notation as

$$M(\Delta_j) = \mathbf{A}(\Delta_j, p_i) R(p_i), \tag{3.5}$$

and $\mathbf{A}(\Delta_j, p_i)$ denotes a matrix of time shifts with magnitudes determined by the path function (Sacchi and Ulrych, 1995; An et al., 2007; Gu and Sacchi, 2009). Alternative Radon methods exist in medical tomography that are based on spline convolutions (Rivière and Pan, 1998; Horbelt et al., 2002). The use of the Fourier transform in this implmentation enables a least-squares inversion estimate of the Radon domain, which is hastened by the solving of multiple, smaller linear systems. Unfortunately, inverse problems are often ill-posed such that uniqueness, existence and stability of the solution are not guaranteed (Tikhonov, 1987), and RT is no exception (Kuchment, 2006). These concerns are alleviated by the addition of an *a priori* assumption (regularization). The simplest regularization is based on the ℓ_2 norm (Parker, 1994) of the Radon signal, which is achieved by minimizing the cost function

$$J = \|M(\Delta_j) - \mathbf{A}(\Delta_j, p_i) R(p_i)\|_2^2 + \mu \|R(p_i)\|_2^2. \tag{3.6}$$

The Lagrange multiplier μ determines the trade-off between the least-squares fit of the data (first term in equation 3.6) and bounding the energy in the Radon domain (second term in equation 3.6). In this implementation, solutions to linear systems are solved directly, which

is sufficient for moderately sized matrices. In the case of large matrices, conjugate gradient methods could be implemented to make computation more feasible.

Regularization methods based on other assumptions include Cauchy-based minimum entropy (Sacchi and Ulrych, 1995) and sparseness approaches associated with the ℓ_1 norm of the Radon signal. However, these regularizations are more computationally expensive since their cost function minimizations are not closed form solutions; instead, iterative methods which converge to the solution are often employed. Earlier methods to solve this problem are based on descending the gradient of the cost function (Landweber, 1951). Subsequent algorithms based on proximal gradients (Daubechies et al., 2004) are known for slower convergence rates (sub-linear), though accelerated methods have been proposed as faster alternatives (Bioucas-Dias and Figueiredo, 2007; Beck and Teboulle, 2009). This inversion code utilizes the Iteratively Reweighted Least Squares (IRLS) method (Daubechies et al., 2010), with linear convergence rates for ℓ_1 norms and quadratic convergence in the limit of ℓ_0 ensures timely computation. The IRLS method assumes a starting model (the ℓ_2 norm solution in this implementation) and updates the Radon solution to the next iteration based on the equation

$$R_{l+1} = (\mathbf{A}^H\mathbf{A} + \lambda\mathbf{Q}_l)^{-1}\mathbf{A}^H M. \tag{3.7}$$

In this equation (3.7) λ is a hyperparameter, $\mathbf{Q}_l$ is a diagonal matrix based on the current Radon solution R_l, $\mathbf{A}^H$ refers to the Hermitian transpose of $\mathbf{A}$ and subscripts refer to iteration step, with iterations continuing until relative changes to the cost function become negligible. The diagonal entries $Q_{mm} = (|R_m| + b)^{-1}$ and $Q_{mm} = (|R_m|^2 + b)^{-1}$ are non-linear due to non-quadratic cost functions for ℓ_1 and Cauchy regularizations, respectitvely. Within these diagonal elements, a second hyperparameter b has been imposed; this ensures continuity of the penalty function's gradient and enforces the degree of sparsity in the final solution. The choice of regularization is at the discretion of the researcher depending on, but not limited to, the nature of the application and availability/quality of data.

Optimization of regularization terms is required to ensure fidelity and stability during inversion. If prior information is known about the noise in the spatial domain, then

optimization may be acheived through a χ^2 test. This is particularily advantageous for the ℓ_1 and Cauchy inversions as the relationship among μ, λ and b parameters will reduce this problem into the optimization of a single parameter. In the case of real data, little is often known about the noise level and optimization must be achieved empirically based on a trade-off curve (L-curve). More detailed discussions of damping parameter and its optimization can be found in Engl and Grever (1994), Sacchi (1997) and Hansen (1998).

3.2 Application of the Radon transform

A suite of transverse-component synthetic seismograms are used to demonstrate the effectiveness of RT. Figure 3.2a shows a record section of simulated SS precursors (Shearer and Masters, 1992) consisting of ~1000 source-station pairs used in the investigation of mantle stratification beneath South America (Contenti et al., 2012). These synthetics were computed using the reflectivity method based on PREM (Dziewoński and Anderson, 1981) and Global Centroid Moment Tensor solutions (Dziewoński et al., 1981) of the associated earthquakes. Differential times between SS and its precursors provide a proven means for constraining the depths of mantle discontinuities (Shearer and Masters, 1992; An et al., 2007; Gu et al., 2009; Deuss, 2009).

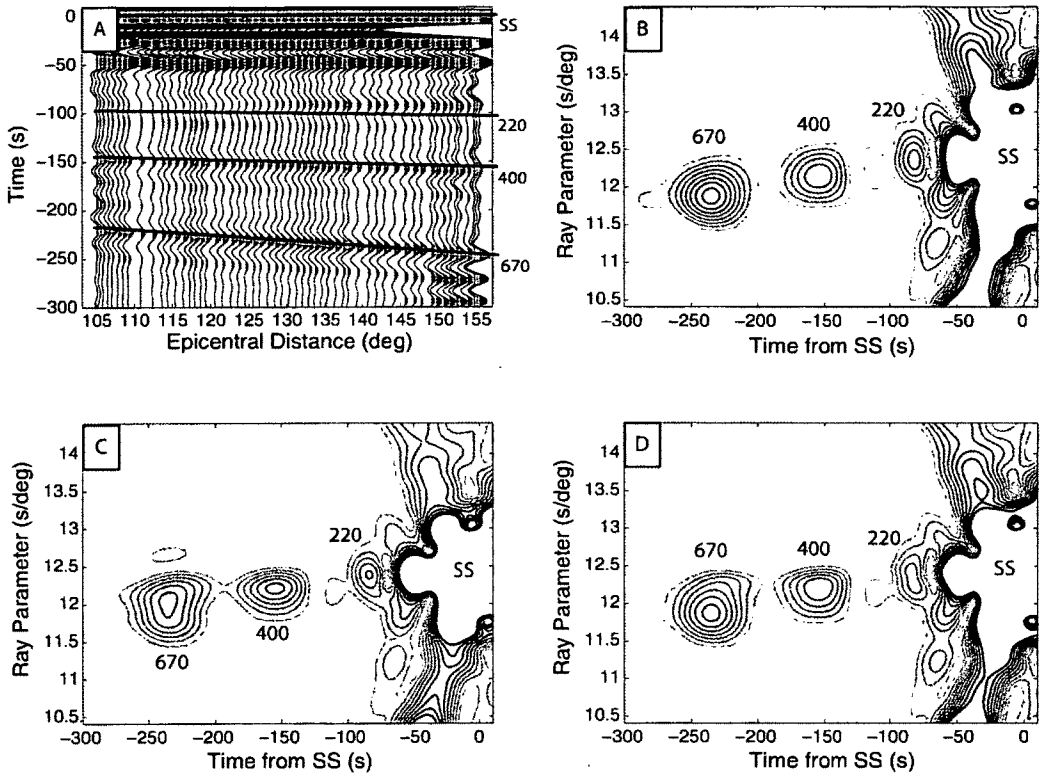

Figure 3.2: Radon transform of a simulated record section containing SS and its precursors. (a) SS and its precursors in the spatial domain. The synthetic seismograms have been aligned on SS. Precursors resulting from discontinuities at 220, 410 and 660 km are highlighted by solid lines. The depths of the 410- and 660-km seismic discontinuities are 400 and 670 km, respectively, in PREM. (b) Instantaneous amplitude of the Radon transform, where the inversion was regularized using an ℓ_2 norm and $\delta \approx 125$. Distinct peaks in Radon domain are attributed to each ray parameter and their respective slopes in the spatial domain. Additional Radon inversions are performed using (c) ℓ_1 and (d) Cauchy methods. Sharper signals are observed in these two cases, especially for SS, due to the emphasis on sparseness. The variance of the residuals was kept constant to ensure a fair comparison of the inversion methods.

Each seismogram is aligned on the arrival of the SS surface reflection and sorted according to epicentral distance. Then, the Radon_inverse routine is applied to the record section (see Figure 3.2) while assuming linear path functions in each of the three regu-

larizations: ℓ_2, ℓ_1 and Cauchy. To ensure a fair comparison, I restrict the variance of the residuals (observation-prediction) to a constant value for all regularization approaches. Radon-domain signals are identified for all reflections and the depth errors of the 660, 410 and 220 km discontinuities are less than 0.2%. The emphasis on the sparseness of the solution is apparent in the Cauchy and ℓ_1 Radon solutions; as the most prominent arrival, SS is most significantly affected by the sparseness criterion (Sacchi, 1997).

As suggested by Figure 3.2, Radon_inverse constructs the Radon domain and enables accurate assessments of the strength and depth of a given seismic reflection. The opposite operation, Radon_forward, transforms the Radon image back to the spatial domain (Figure 3.3). During this process it re-samples SS and its precursors at regular intervals and interpolates phase move-outs within a gap in receiver coverage in the distance range of 110-117° (see Figure 3.3). In addition, the ability to mute other seismic phases greatly facilitates the examination of $S_{220}S$ and $S_{660}S$ in the spatial domain.

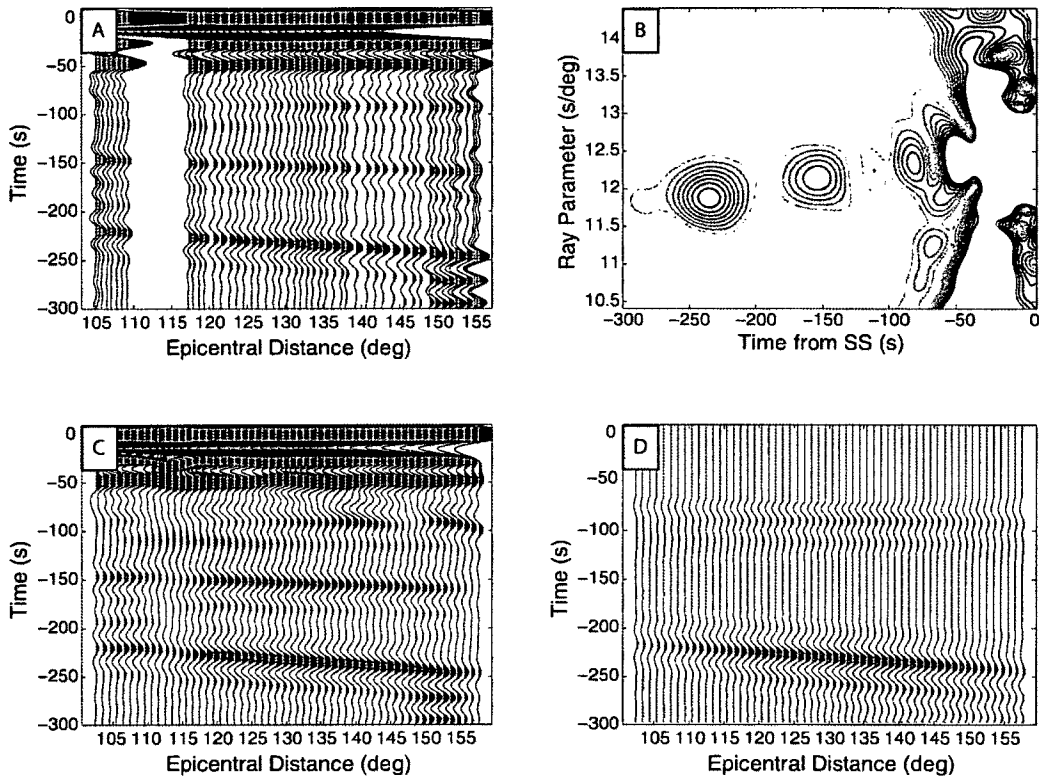

Figure 3.3: Resampling and filtering of seismic data using RT. (a) An irregularly sampled synthetic record section containing SS and its precursors. (b) Instantaneous amplitude of RT based on ℓ_2 regularization. (c) Reconstructed and spatially interpolated record section by applying the forward operator on the Radon signal. (d) Result of applying the forward operator after retaining only the RT signals associated with $S_{220}S$ and $S_{660}S$.

The two routines detailed in this chapter are directly applicable to other geophysical data with a simple change of input record section (in matrix form). As an example, I apply RT to radial-component receiver functions (Langston, 1979; Rondenay, 2009) that were computed based on broadband seismic data from EDM, a station within the Canadian National Seismic Network. The input record section (Figure 3.4a) was obtained using iterative deconvolution (Ligorria and Ammon, 1999) and shows a series of secondary reflected and converted phases after the first arrival. The RT is based on parabolic path functions and an

ℓ_2 norm, the preferred modeling choices due to nonlinear move-out curves. Strong signals are observed at the expected times/ray parameters for first-order crustal reverberations and P-to-S conversions from mantle seismic discontinuities (Figure 3.4b). Signal corresponding to conversions at the 410-km discontinuity (see Figure 3.4b) are best resolved due to coherent time-domain wave amplitudes along the highlighted, *de facto* move-out curve. The ability to isolate and constrain small, secondary arrivals such as P-to-S conversions in Radon domain could greatly assist the imaging of solid Earth seismic structures.

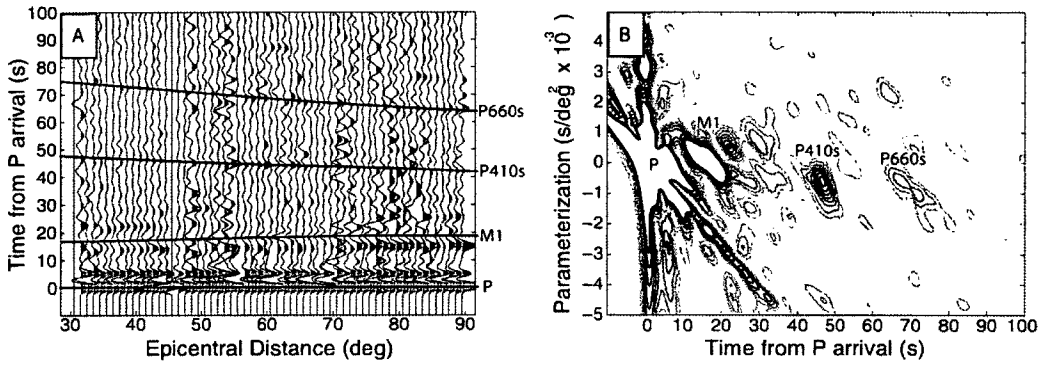

Figure 3.4: RT of receiver function data from station EDM. (a) A record section showing nonlinear arrivals originated from crustal multiples and P-to-S conversions at the 410- and 660-km discontinuities. (b) Instantaneous amplitude of RT domain signals. The transform is computed based on the ℓ_2 norm, parabolic path-functions and $\delta = 30$. Signals corresponding to P410s and P660s are recognizable, especially the former due to coherent, energetic arrivals in the spatial domain. A first-order crustal reverberation, near the main P arrival, is labeled M1 in both panels.

3.3 Conclusions

I have presented two Matlab-based routines, Radon_inverse and Radon_forward, that perform discrete inverse and forward Radon transforms. These frequency-based methods offer the user flexible choices among multiple regularization methods and path functions. They are designed for simplicity and flexibility, and the Matlab foundation ensures portability between platforms. Both Radon_inverse and Radon_forward could be readily adapted or

modified for a broad range of geophysical applications. The Matlab codes and their instructions are available for download at `http://www.ualberta.ca/~rjs10/Software/`.

CHAPTER 4

Development of P′P′ analysis[1]

Seismic inquiry provides valuable insight to the dynamics of the mantle. For example, SS/PP precursors and ScS reverberations are advantageous because their sensitivities are partially decoupled from earthquake and receiver distribution. Limitations due to bandwidth of these phases and complicated Fresnel zones for SS/PP prohibit the analysis of the fine structure of the mantle. Higher frequency methods, such as receiver functions, can robustly identify mantle features, but their strong dependence on station distribution inhibits their applicability on the global scale.

A promising high frequency alternative are P′P′ precursors (Adams, 1968): core phases capable of resolving small-scale structures (resolution of ~5 km vertically, 200 km laterally) in the mantle, owing to its short-period nature (~1 Hz, see Teng and Tung, 1973; Tkalčić et al., 2006) and shallow angle of incidence. The antipodal reflection of P′P′ (see Figure 4.1a) compliments the BP distributions of PP and SS precursors, while the core-traveling ray paths of P′P′ permits imaging at mid mantle (LeStunff et al., 1995) and potentially greater depths. Early regional observations of $P'_{660}P'$ were reported in Antarctica and the Indian ocean (Engdahl and Flinn, 1969), the Atlantic-Indian rise and Ninety-East

[1]A version of this chapter has been submitted for publication. (Schultz and Gu, 2012b, Geophysical Journal International).

ridge (Whitcomb and Anderson, 1970) and Antartica (Bolt and Qamar, 1972), supporting its interpretation as a global feature. $P'_{410}P'$ has remained more elusive, only being reported in a few recent studies (Nakanishi, 1988; Davis et al., 1989; Benz and Vidale, 1993; Xu et al., 1998, 2003). Authors attributed the scarcity of $P'_{410}P'$ to its smaller amplitude, possibly exacerbated by the reflectivity occurring over a gradient (Sobel, 1978; Benz and Vidale, 1993; Xu et al., 2003). Phase identification and analysis are further complicated by triplication of P'P' (PKiKPPKiKP, PKIKPPKIKP, PKPPKP$_{AB}$ and PKPPKP$_{BC}$ see Figure 4.1b), with studies restricting epicentral distances to 60-75° to take advantage of the nearby caustic. The maximum phase nature of P'P' (Figure 4.2b) implies scattering from mantle heterogeneities (King and Cleary, 1974; Haddon et al., 1977; Tkalčić et al., 2006; Earle et al., 2011; Wu et al., 2012) and asymmetric P'P' (Whitcomb, 1973), resulting in arrivals up to 50 and 30 seconds prior to P'P', respectively. These complications have hampered the detection of P'P' precursors; only a handful of studies on these phases were published in the past few decades, despite their promise in high-resolution, global imaging of mantle reflectivity.

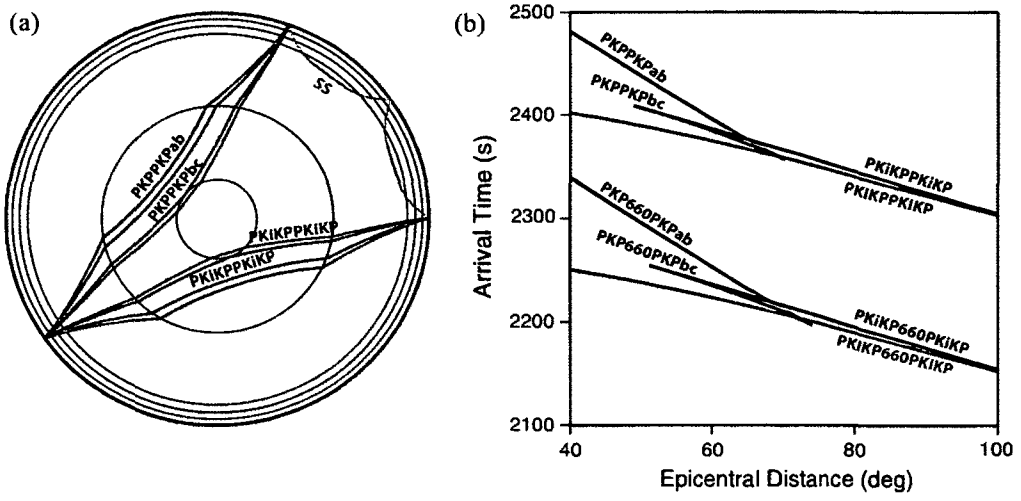

Figure 4.1: Ray paths for various bottom-side reflection phases (a). P'P' phases ($PKPPKP_{AB}$, $PKPPKP_{BC}$, PKiKPPKiKP and PKIKPPKIKP) have antipodal bounce points, while SS and PP (not shown, analogous path to SS) have bounce points which are roughly the geometric mid point. All of these phases may also have precursory arrivals due to reflections below the surface. Move-out curve for P'P' and $P'_{660}P'$ phases (b) based on ak135 earth model. All P'P' phases have a negative, apparent slowness due to their long (>180°) paths.

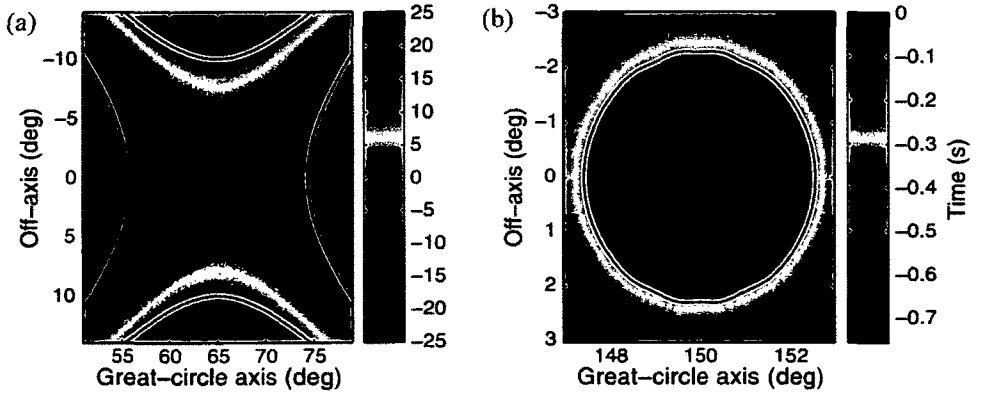

Figure 4.2: Surface Fresnel zones for SS (a) and PKIKPPKIKP (b). Fresnel cutoffs are depicted with black contour lines, based on a quarter of the phase's period. SS phases are minimum-maximum and bounded by 20°, while PKIKPPKIKP is maximum phase and bounded by roughly 4°.

In this chapter I present a robust method of precursor analysis (for brevity RPA) tailored to surmount challenges specific to P'P', but still remaining applicable to other (*e.g.*, SS and PP) precursors. Resolution tests on synthetic seismograms suggest RPA reaches the intrinsic limits of resolution for well behaved data. Further tests on poorly sampled, noisier data provide a metric for the applicability of RPA.

4.1 Method

The reflector depth beneath a BP can be determined by the differential time between the surface and precursory arrivals if the velocities along ray paths are precisely known. Due to path similarity away from the BP, these differential times are dominated by the two-way transit time of the surface reflection above the reflector in the vicinity of the BP. In practice, the task of detecting and timing precursors are complicated by a wide range of factors including noise, interfering phases, non-geometric ray paths, scattering, dipping reflectors, and earthquake source effects. This section details a robust precursor extraction method predicated on careful data preprocessing, deconvolution, partial stacking, RT and migration. This algorithm mainly targets P'P' precursors, but remains completely general for other low-amplitude arrivals such SS or PP precursors.

4.1.1 Preprocessing

Data is deconvolved from receiver response and then filtered to an appropriate frequency band, depending on the nature of the data. Often data needs to be discarded on the basis of poor signal to noise ratio (SNR). In most studies, seismograms below SNR of 3 (Deuss, 2009) are considered unacceptable and rejected. More quantitatively, analysis will adhere to the rubric determined by synthetics tests in this chapter. To ensure reliable results, epicentral distances are limited on the basis of steep incidence angle and minimizing effects from extraneous phase arrivals. Seismograms are also inspected using a Matlab-based visualization tool to review traces and reject aberrant ones.

4.1.2 Deconvolution

In prior analysis of precursors, earthquakes with high moment magnitudes (Mw > 7.0) are omitted. Large magnitude earthquakes potentially have long, complicated source time functions, which are problematic in data stacking. Path dependent properties, like attenuation, will vary with the distribution of BP azimuths, disrupting the quality of partial data stacks. Seismic deconvolution minimizes these complications, retaining only effects local to the study region. In terms of the convolutional model, the Fourier transform of the main phase $A(\omega)$ is expressible as the function

$$A(\omega) = s(\omega)H_{s2d}(\omega)H_{d2BP}(\omega)r_s(\omega)H_{BP2d}(\omega)H_{d2r}(\omega). \tag{4.1}$$

The spectral element $s(\omega)$ represents the complete earthquake source mechanism, $r_s(\omega)$ is the distortion due to reflection at the surface and the terms of the form $H_{x2y}(\omega)$ (x and y being generic) are the transfer function encountered along the wave path: from starting point x to ending point y, with abbreviations for source (s), discontinuity (d), BP (BP), and receiver (r). The spectrum of a precursor $A_d(\omega)$ shares similar features:

$$A_d(\omega) = s(\omega)H'_{s2d}(\omega)r_d(\omega)H'_{d2r}(\omega). \tag{4.2}$$

The main and precursory phases have a common source function and experience similar path effects away from the BP. If it is assumed that non-local transfer function terms of the main and precursor phases are the same within error (*e.g.*, $H_{s2d}(\omega)$ versus $H'_{s2d}(\omega)$), then deconvolving the main phase from precursors, in terms of a spectral division, yields the result

$$D(\omega) = \frac{r_d(\omega)}{H_{d2BP}(\omega)r_s(\omega)H_{BP2d}}. \tag{4.3}$$

Deconvolved signals $D(\omega)$ are consistent, resulting from the properties of the reflector (*e.g.*, depth, impedance contrast) and the overlying medium in the vicinity of the BP. This is favorable for stacking procedures since inconsistencies between traces are minimized and

thus will stack more coherently.

In reality, spectral division is unstable and requires addition of a water level term to reduce spurious contributions from noise (Wiggins and Clayton, 1976; Ammon, 1991). Instead, I use a time-domain, regularized, least-squares approach (Sacchi, 1997), to estimate the deconvolved seismograms. This is achieved by deconvolving the seismic trace $S(t)$ from a window around the main arrival and minimizing the cost function

$$J = \|S(t) - A(t) * D(t)\|_2^2 + \mu\|D(t)\|_2^2. \tag{4.4}$$

The damping factor μ is determined using a χ^2 statistic as a target misfit (Sacchi, 1997) and a 1-D search based on a spline interpolation. The optimal damping factor is chosen as one that matches the χ^2 expectation value. Optimally damped, time-domain inversion deconvolution suppresses Gaussian noise, which aids further analysis. Other cost functions that emphasize spareness (Cauchy-based) were investigated for the deconvolution of P'P', however, under optimal damping conditions and typical noise encountered with P'P' these functions converge to the solution from Equation 4.4 (Sacchi, 1997).

Sample deconvolution of P'P' is depicted in Figure 4.3, the removal of source mechanism and path complexities away from the data gather simplifies analysis. For the purpose of demonstration, arrivals on the deconvolved trace have been exaggerated based on a running average of the seismic energy. The deconvolved trace (Figure 4.3b) has many arrivals, consistent with reflections from accepted seismic discontinuities in the structure of the mantle. These arrivals are not apparent on the unaltered seismogram (Figure 4.3a), even after similar noise suppression. The complex nature of the P'P' waveform obscures much information which is recovered through deconvolution. In the remainder of the chapter deconvolved traces will still be referred to as SS or P'P' for brevity; however, it is important to note that these traces are, more correctly, an estimation of the reflectivity series beneath the BP.

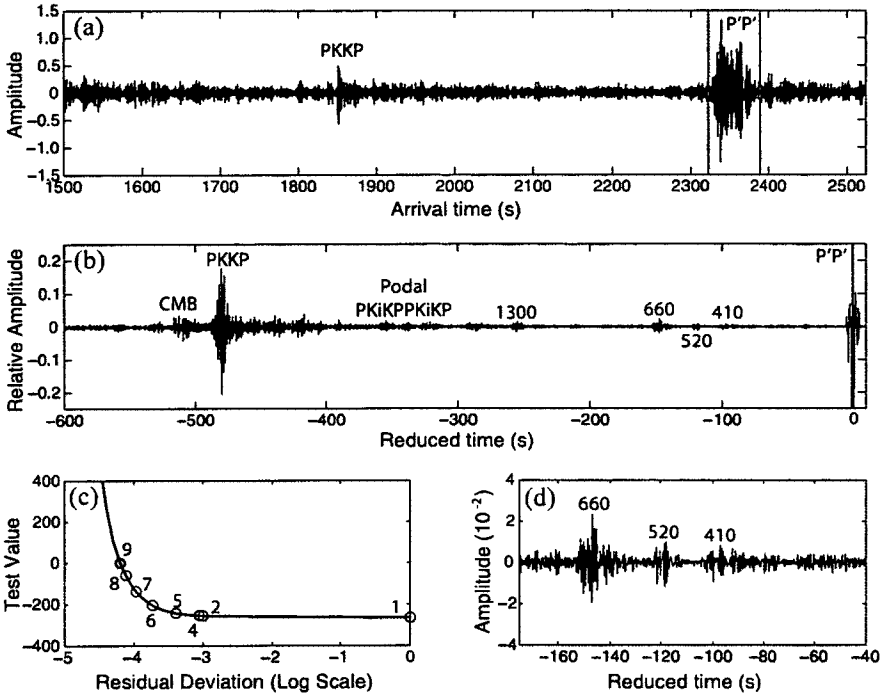

Figure 4.3: Deconvolution of a single P'P' seismogram. The seismogram (a) shows the P'P' arrival, which has been windowed for deconvolution. The signal on the second panel (b) has been deconvolved from this P'P' waveform, which now appears as a simpler impulse (scaled to an amplitude of 1.0). The deconvolved signal has been enhanced using a running average of seismic energy, to elucidate other arrivals. Precursory arrivals have been labeled according to their estimated depths, other interfering arrivals (podal PKiKPPKiKP and PKKP) will be omitted from migration in the Radon process. A test (c) determines optimal damping at the zero crossing of the test value. Numbers indicate step progression in interpolating toward optimally damped solution. The final panel (d) is smaller section of the deconvolved trace, showing MTZ reflections more closely.

4.1.3 Partial stacking

Precursor data is low amplitude, typically less than 3% of the main arrival (Shearer, 1993; Gu et al., 1998, 2003), which presents a formidable challenge in phase detection and measurement on individual records. Seismograms are discretized into caps, based on geographical location of their BP, and then binned by epicentral distance and stacked. This offers a com-

promise between retaining precursor move-out, while still enhancing SNR. Spatial overlap for distance bins is chosen as the distance precursory arrivals remain in phase. Coherent information will stack constructively, potentially increasing SNR by a factor of the square root of the number of seismograms stacked (Shearer, 1991a). Some effects of the maximum-phase nature of P'P' (asymmetric arrivals) are partially mitigated through stacking, reducing their presence from 30 seconds to 10 seconds prior to P'P' (Sobel, 1978). Other non-linear stacking techniques such as N-th root (Kanasewich et al., 1973) and phase-weighted (Schimmel and Paulssen, 1997; Rost and Thomas, 2009) include the advantage of further noise suppression. However, these methods distort amplitude information of the signal; an integral quantity in investigating reflector strength. The method forgoes additional noise suppression in the stacking phase in favor of candid amplitudes.

4.1.4 Radon transform

Precursor phases are characterized by ray parameters that are similar, but not the same, as their main phase. A discrepancy in ray parameter results in a subtle precursor phase move-out after the main arrival has been corrected to zero slowness, prohibiting the use of a direct summation in precursor analysis. Instead, slant stack methods (Rost and Thomas, 2009) are employed along sets of paths, *i.e.*, linear or parabolic. Summation along a path enables simultaneous constraints of both differential time and ray parameter of the precursor phases; the two variables in this migration approach. The addition of ray parameter information is useful in assessing the shape of the reflector and the mantle heterogeneities surrounding it.

Instead of forming time-domain slant stacks, which suffers from poor slowness resolution, I adopt a frequency-based inversion implementation of the RT (Schultz and Gu, 2012a). Inversion offers the advantage of improved resolution through regularization techniques based on the ℓ_2 or ℓ_1 norms as well as Cauchy-based (Sacchi and Ulrych, 1995) cost function. The optimal damping parameter is chosen as the turning point on the L-curve (Parker, 1994) for competing cost function terms: least-squares fit to the data and bounding the energy in the Radon domain (ℓ_2 norm). Further work into the applicability of sparse

Radon inversions (ℓ_1 and Cauchy-based) for precursors could potentially further increase the resolution of my method. Slowness information in the Radon domain provides an advantage for user review, extraneous arrivals (*e.g.*, podal PKiKPPKiKP in P'P' analysis) are identified and excluded from further analysis. Prior to migration, additional noise suppression in the Radon domain can be achieved by a weighting function based on a running average of seismic energy. However, this comes at the expense of amplitude distortion, obscuring reflector strength information. Schultz and Gu (2012a) offers the portable, freely available Radon operators used in this chapter.

4.1.5 Migration

Migration bridges the crucial gap between seismic parameters and reflector depth. Various migration techniques have been introduced over the years, each with their own benefits and detriments. Kirchhoff migration techniques have the potential to image dipping structures, but multipathing due to caustics or scattering in complicated geology is problematic for single valued travel time implementations (Etgen et al., 2009). Sophisticated techniques, like reverse time migration (Chang, 1994; Chang and McMechan, 1990) offer more rigorous approaches to solving the acoustic wave equation. However, these methods come at the price of computational cost and often assume regular spatial sampling, which is impractical for precursor BP distribution. This implementation defers to an application of beam forming Kirchoff migration (Sun et al., 2000). Gathers of data are beam formed using the RT, which summarizes spatial data into the $\tau - p$ domain. Radon amplitudes are then migrated to depth based on travel time calculations that assume ray theory and Huygen's principle. Ray paths are computed (Crotwell et al., 1999) with their associated differential times and ray parameters while conserving epicentral distance. Particular to P'P' and its maximum phase nature (Figure 4.2b), arrivals are highly susceptible to asymmetric reflections (Whitcomb, 1973; Wu et al., 2012) or scattering (Tkalčić et al., 2006; Earle et al., 2011; Wu et al., 2012). This demands that all ray paths computations, both specular and non-specular, are incorporated in the migration procedure (see Figure 4.4a). Contours of constant depth

(isobaths) in Figure 4.4b and c reveal that both SS and P'P' precursor differential times are maximum phase with respect to perturbations in ray parameter. The maximal time for each isobath represents the specular reflection of SS (Figure 4.4b) and P'P' (Figure 4.4c) precursors, all other points along the isobath are non-specular (scattered or dipping discontinuity). In this formulation, the Radon domain (axes of differential time and ray parameter) corresponds to values of reflector depth, allowing for the direct mapping of seismic energy to the appropriate depths.

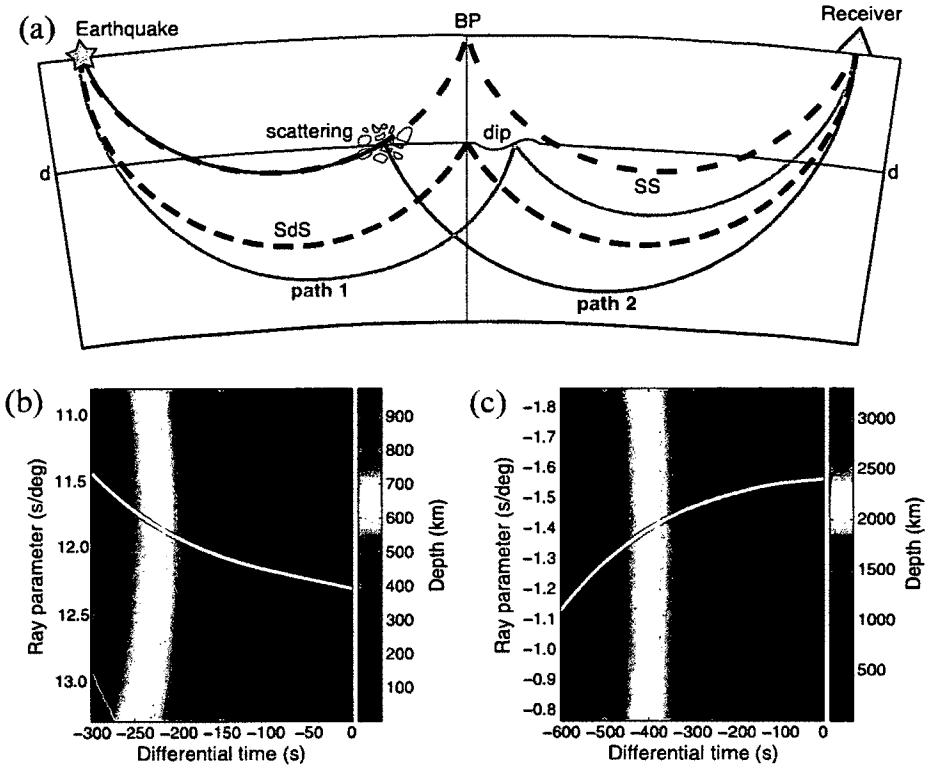

Figure 4.4: Caricature depicting sample ray paths for specular, asymmetric and scattered SS arrivals (a), incorporation of all arrivals is important for further P'P' analysis (P'P' paths not shown). Dotted lines show specular arrivals for the main phase and precursor. Ray paths for forward scattering (path 2) and an asymmetric reflection due to a dipped surface (path 1) are also depicted. Migration mappings for SS (b) and P'P' (c) are tabulated using epicentral distances of 130° and 60°, respectively. The P'P' phase has the potential to constrain whole mantle structure while SS only permits the analysis of the upper-mantle. Specular reflections are confined to time and ray parameter values along the white line. Non-specular ray paths are also defined for various scattering depths, ray parameters and differential times. Scattering from a constant reflector depth defines contours (isobaths) in this domain and reveals P'P' and SS are maximum phase with respect to perturbations in ray parameter.

4.2 Synthetic tests

Transverse-component, synthetic seismograms based on approximately 5000 source-station pairs used in the investigation of mantle dynamics beneath South America (Contenti et al., 2012) are used to demonstrate the effectiveness of RPA. Each trace is based on PREM structure (Dziewoński and Anderson, 1981) and Global Centroid Moment Tensor solutions (Dziewoński et al., 1981) of the associated earthquakes. From this library of SS precursors, seismograms are chosen randomly and placed into caps, which are then contaminated with noise. This process is performed twenty times for each combination of cap size (20, 30, 40, 60, 80, 100, 120 and 200) and SNR ratio (2.0, 4.0, 6.0, 8.0 and 10.0). Seismograms are deconvolved from, and aligned on, the arrival of the SS surface reflection. Tests on data sets below a SNR of 2.0 are not performed due to the inability to reliably detect main phase arrivals, which RPA is predicated upon. The Radon inverse routine (Schultz and Gu, 2012a) is applied using the ℓ_2 norm regularization and linear precursor phase move-out. Precursor phases in the Radon domain are migrated using my implementation, with the maximum migration amplitude determining reflector depth. A statistical analysis of the precursor residuals (observation-expectation) shows that (see Figure 4.5) many of the well sampled caps (100, 120, 200) reach the intrinsic limit of resolution for this SS sample ($\sim$2 km). I adopt a resolving power with a deviation of 4 km (*i.e.*, half of the intrinsic limit) as the cutoff. This restriction provides a general guideline to precursor analysis; for example, caps with SNR of 2.0 would require a minimum of $\sim$60 seismograms to produce stable and reliable results. A similar trend appears for systematic bias (Figure 4.5a), caps stacked with as few as 60-80 traces with SNR of 2.0 are accurate to within 2 km. Better still, the higher SNR stacks (>2.0) only require $\sim$30 traces for accurate depth reconstructions.

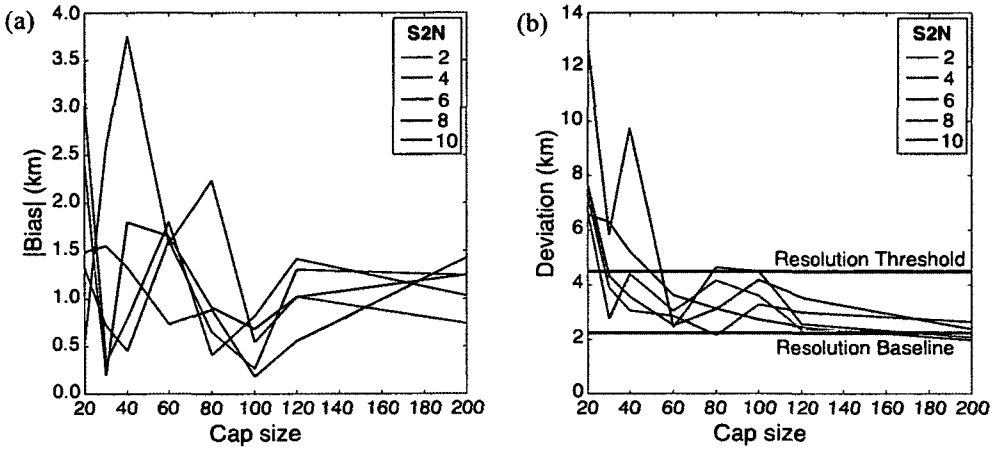

Figure 4.5: Statistical results from synthetic tests on RPA. Absolute value of the residual bias (a) and residual standard deviation (b). A general trend of decreasing accuracy, reliability and stability are noted for decreasing cap sizes and/or SNR ratio. The resolution baseline is determined by the Nyquist frequency, the smallest possible resolving power of a seismogram. An acceptable level (Resolution threshold) was chosen as twice this and caps above this value are deemed too unstable for reliable analysis.

4.2.1 Discussion

The synthetic tests performed in this section are highly idealized. Synthetic traces incorporate only reflected energy, minor interference from extraneous phases and introduced noise is both white and Gaussian. Even in this idealized case details about the efficacy of RPA are inferred. Robust depth determinations from precursor phases are observed for caps as small as 60. In comparison, methods based solely on linear stack algorithms (partial and slant stacking) expect stacks of 400 SNR=2.0 traces to coerce a 5% amplitude precursor to the same degree of confidence. This approximate order of magnitude improvement can be attributed to the strong suppression of random noise in the deconvolution/Radon inversion procedures. Realistic data will differ drastically from these test cases; scattered or asymmetric arrivals, dipping reflectors, interfering arrivals, heterogeneity and complicated source time functions limit the effectiveness of conventional methods. Established methodology

utilized in RPA attempts to address these issues, in turn reproducing reflectivity structure more faithfully than linear stacking and migration alone. These advances are hardly definitive though, with pervasive noise is still recognized in migration of P'P' data.

4.3 Conclusions

Methodology described in this chapter alleviates prior concerns associated with P'P' precursors, allowing for robust, accurate and highly-resolved migration. Synthetic tests performed on this method provide a quality control baseline for further precursor investigations. Furthermore, results suggest significant improvements over more traditional linear stacking methods. The analysis of P'P' precursors, coupled with appropriate methodology, presents an opportunity to study the mantle in great detail, especially when complimented by broader-scale SS or PP constraints. The aim for developing RPA is to enable the analysis of P'P' precursors. In its current state RPA can reliably map precursor energy to appropriate depths, but could still benefit from the modification or addition to its ensemble. The caustic present in P'P' has only been partially mitigated through deconvolution and beam forming. The extension of Gaussian beam migration methods (Hill, 2001; Popov et al., 2010) to precursors would better address phase triplication with a more complete reconstruction of amplitude information. The possibility of coherent, spurious or strong noise sources warrants further investigation. Attenuation of these noise sources could be performed in either the Radon domain, through ridgelet techniques (Do and Vetterli, 2003) and application of sparse inversion (Schultz and Gu, 2012a) or the spatial domain by means of multichannel singular spectrum analysis (Oropeza and Sacchi, 2011), curvelet transforms (Herrmann and Hennenfent, 2008) or prediction filters (Abma, 1995). If spatial denoising techniques prove adequate, the elimination of partial stacking and its blurring effects, from RPA, could further increase precursor resolution.

CHAPTER 5

Pilot analysis of the Nazca-South America subduction zone[1]

The objective of RPA is to enable the robust analysis of P′P′ precursors, to assist the investigation of the existence, strength, depth, thickness and spatial scale of mantle reflectors/discontinuities. The spectral content of P′P′ indicates high resolution imaging of the mantle in both vertical and lateral extents, after the application of processing techniques. Resolving mantle structures at a scale of ~5 km allows for the interrogation of its fine structure; phase transitions which were only probed for depth and reflection amplitude, on the broad scale, may appear more clearly as a sharp or gradual process occurring over a range of pressures. Further still, characteristics of scattered waveforms could indicate the presence of heterogeneity in tune with precursor bandwidth. Through a greater understanding of these characteristics one may conjecture potential origins, providing insight to the present-day state of the mantle.

In this chapter I apply RPA to image the mantle at select locations near the Nazca-South America subduction zone. This continuing tectonic process began in the late Trias-

[1]A version of this chapter has been submitted for publication. (Schultz and Gu, 2012b, Geophysical Journal International).

sic (Pardo-Casas and Molnar, 1987), with prolonged subduction being responsible for the orogeny of the Andes and volcanism within. Today, this ocean-continent convergence occurs at a rate of ~6.6 cm/year (Kendrick et al., 2003), with evidence of its history from tomographic results (Engdahl et al., 1995; Li et al., 2008; Fukao et al., 2009). High velocity anomalies, attributed to the descending Nazca slab, penetrate through the MTZ and into the lower mantle. Thermal effects from the slab contribute to a regionally depressed 660, as evidenced by studies on SS precursors (Flanagan and Shearer, 1998; Collier and Helffrich, 2001; Schmerr and Garnero, 2007; Contenti et al., 2012) and receiver functions (Liu et al., 2003; Wölbern et al., 2009). Compositional variations near the top of the MTZ have also been suggested as the cause of split/diminished $S_{410}S$ (see Figure 5.1) amplitudes (Schmerr and Garnero, 2007; Contenti et al., 2012). The study of mantle discontinuities could be enriched by the addition of high resolution P′P′ precursors. Tentative results in this chapter further test the accuracy and robustness of RPA, while simultaneously evaluating the consistency, sharpness, and origin of mantle seismic discontinuities beneath South America.

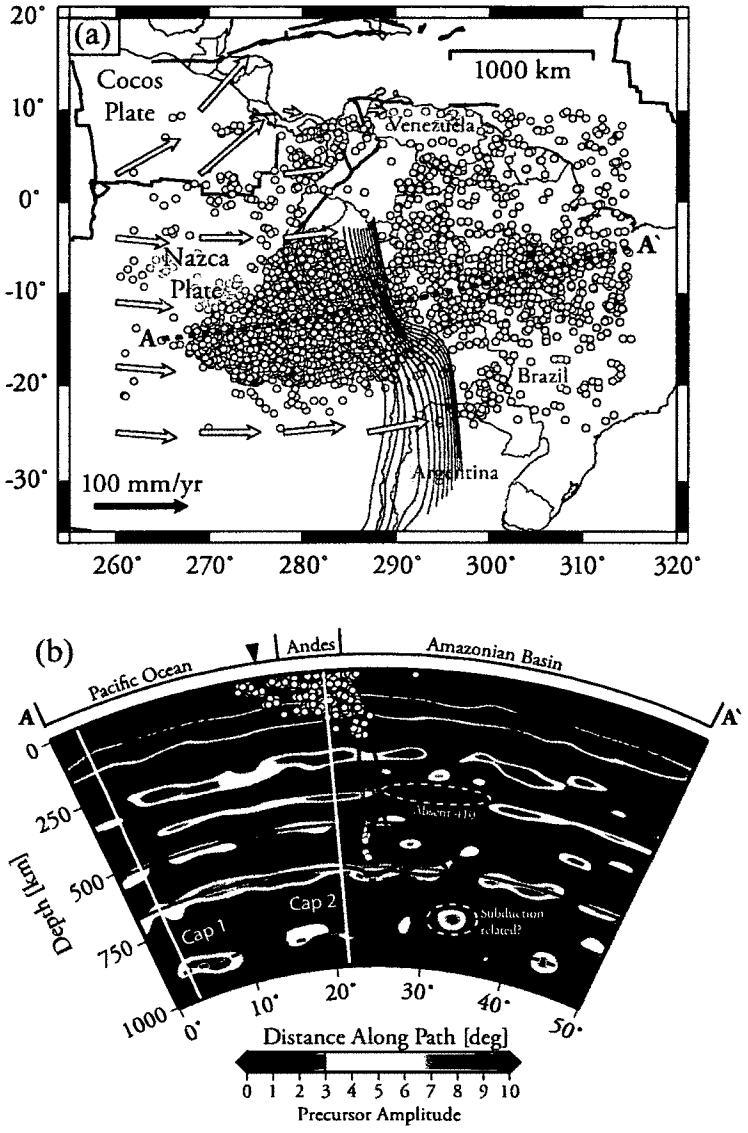

Figure 5.1: BPs of the 5720 traces used in the study of Contenti et al. (2012) (a). Slab contours are represented by thin grey lines (Gudmundsson and Sambridge, 1998), plate boundaries are depicted with thick black lines (Bird, 2003) and plate motions by filled arrows (Kreemer et al., 2003). The reflectivity cross section path is bounded by the points A and A′, the results of which are in panel (b). Interpreted position of the Nazca slab is outlined in white and the 410, 520 and 660 discontinuites are denoted with black lines laterally along the cross section and white circles indicate earthquake hypocenters. Radial white lines reference the cap centres studied in this chapter (see Figure 5.2). Figure is modified after Contenti et al. (2012).

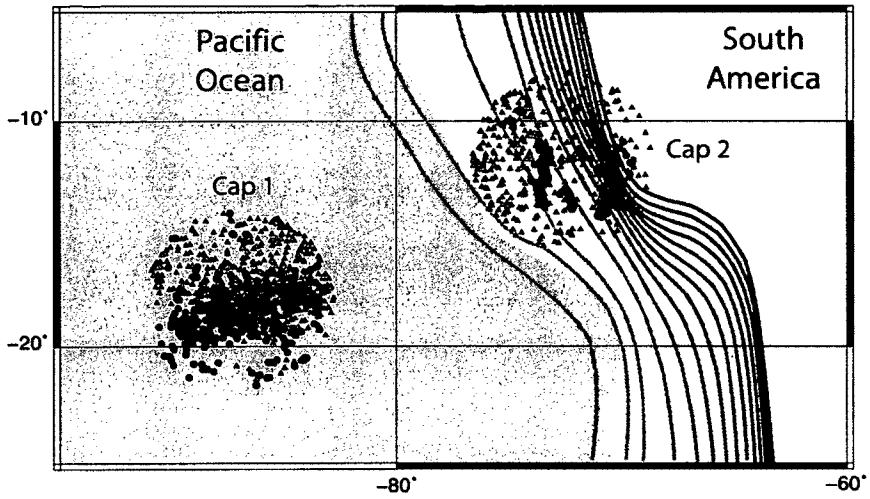

Figure 5.2: Two sample caps near South America. The distribution of BPs for SS (red triangles) and P′P′ (blue circles) are depicted for two caps (Cap 1 and 2) sampling oceanic and subduction zones. Cap 1 contains 778 SS and 381 P′P′ traces, while Cap 2 contains 469 SS and 276 P′P′. Subducted lithosphere is represented by green contours (Gudmundsson and Sambridge, 1998).

5.1 Processing details

Two distinct regions are targeted in this experiment (see Figure 5.2): southeastern Pacific ocean basin (centred at 18°S and 87°W) and the subduction zone beneath the Southern Andes of Peru. The choice of locations are motivated by regions of scientific interest as well as by the density and overlap of P′P′ and SS datasets. The SS data is a subset of Contenti et al. (2012) with epicentral distances of 100-160°, source depths from 0-100 km and bandpass filter corners at 0.013 and 0.07 Hz. The bandwidth of SS precursors utilized will investigate the mantle at a nominal depth resolution of ~30 km, while P′P′ bandwidth (with filter corners at 0.45-1.80 Hz) results in a finer scale of ~5 km. The P′P′ data set encompasses publicly available data archived at IRIS Data Management Center from 1990

to 2009, where the selected epicentral distances and source depths are 50-85° and 0-600 km, respectively. I applied RPA to each cap using the ℓ_2 norm regularization and linear phase move-outs for Radon inversion, which was sufficient for the extraction of SS precursors (see Figure 5.3a and b). P′P′ data sets required weighted noise suppression in the Radon domain (see Figure 5.3c and d), which reduces their ability to quantitatively analyze the reflection strength. To ensure fair comparison between SS and P′P′, amplitudes of the migration profiles were normalized to the same total energy. Migration was subsequently performed on these data sets assuming velocities from ak135 (Kennett et al., 1995). It should be noted that, negative and positive Radon domain signals are migrated independently to prevent destructive interference. This bifurcation is not required for SS, as most of the migrated energy is specular (*i.e.*, positive and negative peaks are out of phase, see Figure 5.3a, b and Figure 5.4). On the other hand, much of the precursor energy from P′P′ is scattered and incoherent, therefore necessitating the separation of overlapping positive and negative peaks (see Figure 5.3c, d and Figure 5.4). The majority of the interpretation of migrated profiles will focus on the positive amplitudes, as is typical for precursor analysis (Flanagan and Shearer, 1998; Gu et al., 2003).

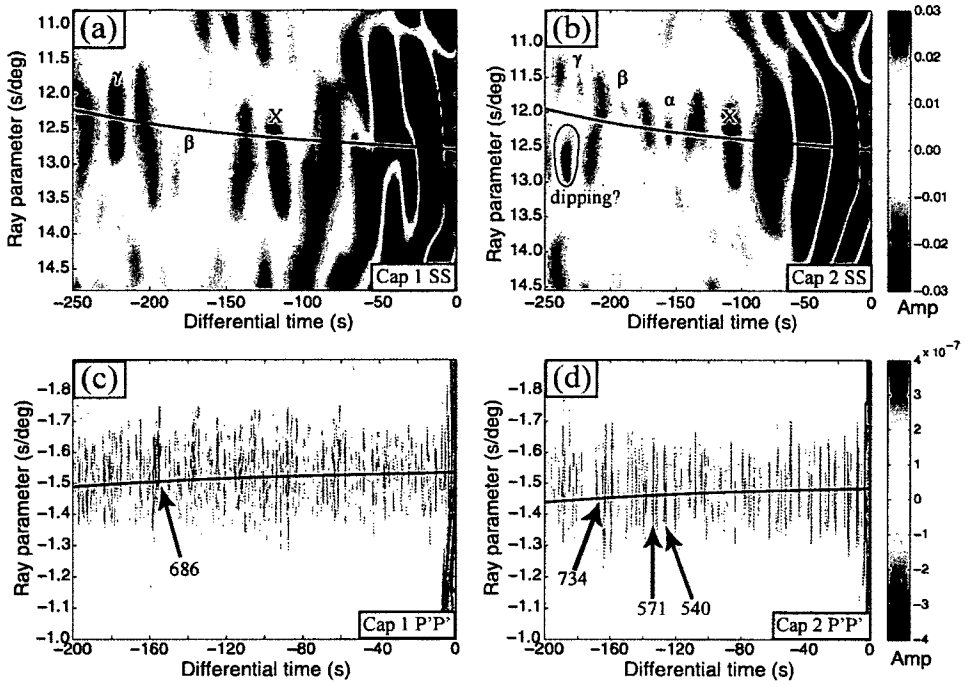

Figure 5.3: Spatial data has been transformed into the Radon domain for Cap 1 (a and c) and 2 (b and d) with specular reflections occurring along the black line. The low frequency content of SS data (a and b) manifests as large sidelobes. Oceanic data (a) depicts a strong, specular reflection of 660 (γ). In contrast, depression of the 660 in subduction zones implies a dipping reflection interface, evidenced in the Radon image (b). P'P' Radon domains (c and d) starkly contrast SS counterparts. Arrivals are completely independent, no sidelobes are apparent. Many of the P'P' precursors are non-specular and thus difficult to interpret in the Radon domain. Migration will correctly assign a depth to all arrivals, regardless of scattering or asymmetric reflections. Letters and numbers provide labels to phases referred to in the text.

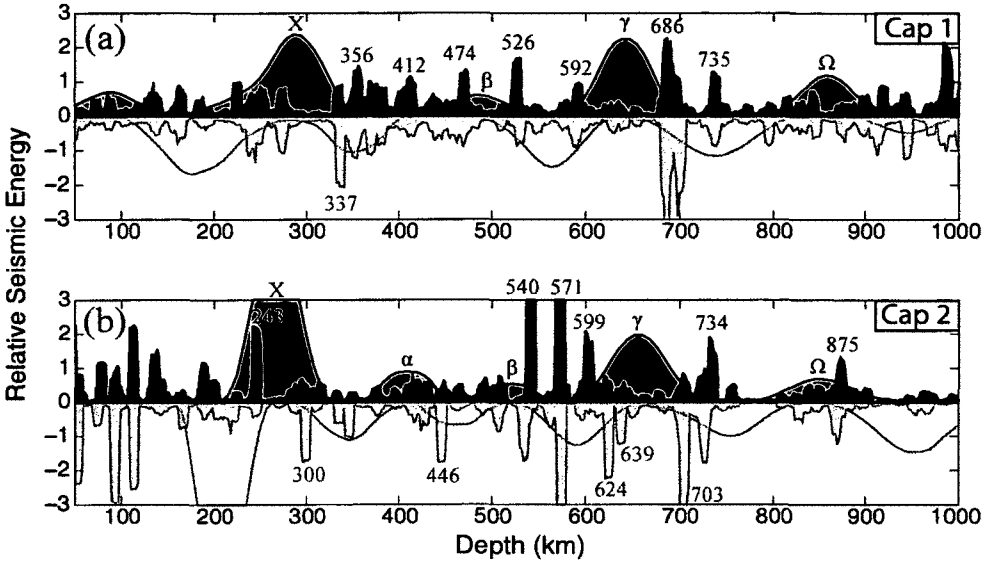

Figure 5.4: Migration profiles for Cap 1 and 2. Migration for SS (red-filled traces) and P′P′ (blue-filled traces) is repeated for both their positive (upper half) and negative (faded lower half) amplitude information. Positive amplitude information is used to infer mantle structure, dynamics and composition local to the south eastern Pacific ocean (a) and subduction zone (b) caps. Letters and numbers (color-coded) provide labels to phases referred to in the text.

5.2 Multi-scale migration results

The Radon solutions prior to migration (Figure 5.3) show major differences in the spectral contents of SS and P′P′ precursors. Signals from the SS precursors are dominated by coherent (along the slowness axis), low-frequency energy maxima (see Figures 5.3a and 5.3b). A distinct advantage of P′P′ precursors over SS precursors is the clarity of the wave field (see Figure 5.3). The time windows from -100 to 0 seconds in Figures 5.3a and 5.3b are cluttered by large side-lobes of SS, with the extent of the interference being largely dictated by the complexity of the crustal structures (Deuss and Woodhouse, 2002; Gu et al., 2003; Rychert and Shearer, 2010). In contrast, the overwhelming amplitude of P′P′ is limited to

the first 10 seconds (Cap 1, see Figure 5.3c) or less (Cap 2, see Figure 5.3d). These times would translate to depths shallower than 40 km, thereby providing a relatively unobstructed view of the lithosphere and asthenosphere.

Energetic signals (labeled X in Figure 5.3a and b, letters will refer to labels on Figure 5.3 or 5.4) are consistently observed at the relative times of -116 seconds in the Pacific ocean to -107 seconds in the vicinity of Nazca slab, which suggest a strong reflection in the depth range of 285-270 km. A prominent signal (γ) at -222 seconds beneath the ocean, which translates to a depth of 645 km, is specular due to its canonical ray parameter. In comparison, a much weaker and highly variable signal is observed near the plate boundary; the signal strength and ray angle dependence are both consistent with a dipping interface (see Figure 5.3b). The apparent lack of the 410 in Cap 1 and a modest 410 in Cap 2 (α) corroborates the corresponding observations of Contenti et al. (2012) and raises questions about the thermal and compositional variations at the top of the MTZ. Radon signals from the P′P′ precursors are highly variable across the entire time range (Figures 5.3c and 5.3d), especially beneath the ocean basin. The juxtaposed positive and negative peaks severely limits my ability to identify and interpret individual phases from the Radon domain alone, a major reason that a depth migration based on the Radon solution is vital for P′P′ precursors. Closely packed arrivals at a depth of 686 km ($\sim$-157 s) represents that maximum P′P′ energy under the Pacific ocean basin. Two potentially deeper reflections are recognizable at $\sim$700 and 740 km depths in the vicinity of the subduction zone, as well as distinct arrivals in connection with reflectors at 571 and 540 km (β) that favor a low-frequency, mid MTZ arrival in S waves (see Figure 5.3b).

Accurate interpretation of the existence, nature and depth of reflections require proper depth migration, a critical procedure necessitated by the complex P′P′ Radon image (see Figures 5.3c and 5.3d) and ray angle dependence of 660 in SS precursors. The resulting migrated traces based on decoupled positive and negative Radon amplitudes (see Figure 5.4) become much simpler through a proper summation of the energies from various mantle origins. The energetic arrivals labeled by X and γ from SS precursors (Figure 5.4)

translates to prominent reflections. The latter phase exhibits minimal complexities in Cap 2 (see Figure 5.4b for comparisons), while showing a greater depth (660 km) than the Pacific ocean basin. In both caps, the positive X phase is preceded by a large negative swing. Weak reflectors are also detected in the depth range of 830-880 km (Ω) and within the MTZ (β), the latter of which varies from the ocean (488 km) to the subduction zone (518 km). On the other hand, the 410 is invisible beneath eastern Pacific oceans and low amplitude (α) under the South American continent. Both observations are in qualitative agreement with those of (Contenti et al., 2012) and impose constraints on the mantle at the base of the asthenosphere. Overall, the structure obtained by SS precursors provides a useful reference for the long wavelength characteristics of known and postulated discontinuities/reflectors.

The migration profiles of P'P' precursors show greater complexity than their SS counterparts. Instead of broad energy maxima centered at the phase boundaries, P'P' precursors cluster near the tail ends of the SS precursor signals for the 660 in both caps while exhibiting minimal energy in the center. The most prominent P'P' arrival is characteristically first-order (resembles the main phase arrival) in Cap 1 at 686 km. The projected depths of this phase is most compatible with reported values from Flanagan and Shearer (1998) and the regional profile of Contenti et al. (2012), indicating an anomalously deep 660 in an oceanic region (Cap 1) and expected, large depressions beneath the Nazca plate subduction zone (Cap 2). It is worth noting that the signal at 703 km in Cap 2, which was significant in Cap 1, is diminished and no longer resembles a first-order reflection. In addition, two distinct peaks are detected flanking the central arrival in the depth ranges of 592-599 km and 734-735 km, which are the most consistent arrivals between the two tectonic regimes sampled by this data. The shallower arrival is more prominently observed in the subduction profile, reporting a slight depression, an increase in amplitude and a second, deeper, negative amplitude (thickness of $\sim$45 km).

Migrated P'P' precursors shows significantly more non-specular and scattered energy than SS, especially beneath the ocean (Cap 1). The sequence of contiguous P'P' precursors within the depth range of 337-412 km is highly variable and complex. Initiated by a neg-

ative arrival at 337 km, the main body of the wave train consists of a series of incoherent arrivals that, judging from the correlated positive and negative arrivals, likely result from mantle scattering. These contiguous arrivals are concluded by a positive pulse at 412 km and proceeded by a deeper, more isloated arrival at 474 km. This highlights the structural differences, rather than similarities, between the two examined regions at fine scales. The remainder of the MTZ features some of the most robust P'P' precursors despite strong regional variations in their depths and migration amplitudes. A distinct positive peak is observed at 526 km beneath the Pacific (see Figure 5.4a), while exceptionally large P'P' phases at the equivalent depths of 540 and 571 km (~2.5 times larger than the nearby γ arrival) beneath the plate convergent zone offers critical information on the impedance, depth, and spatial scales of the responsible MTZ structure (see chapter 5.3). The overall clarity and plurality of P'P' precursors in the depth range from 450 to 580 km clearly favor the observed (and relatively weak) S-wave signal in mid MTZ as a depth-averaged reflection, rather than a side-lobe of the 660 reflection. The P'P' precursors sampling the mantle beneath Nazca-South America subduction zone also exhibit more structure than those beneath the Pacific ocean basin. Exceptional to the subduction profiles, several early lithospheric arrivals (<100 km) as well as energy at 243 km are noted. Several early lithospheric arrivals (<100km), a moderate energy peak at 243 km and mid mantle (Ω in SS, 875 km in P'P') are unique to the plate boundary zone. The characteristics of these signals potentially reflect the geometry and structure of subducted oceanic lithosphere in this region (see chapter 5.3). In addition, Cap 2 shows moderate mid mantle arrivals in both SS (β) and P'P' (at 875 km) precursors. Their presence and overlapping depths within the active subduction zone appear to favor slab penetration into the lower mantle.

5.3 Discussions

The development of RPA mainly aims to address the shortcomings of P'P' for a better utilization of its exceptional resolving power. Deconvolution plays a key role in the process by simplifying the P'P' waveform to an impulse. The reduction of the main arrival to an

impulse has several important properties: source mechanism no longer contributes to the trace, an impulsive response limits the overlap of arrivals, and precursory arrivals depend on parameters local to the BP. These properties allow for more coherent stacking of traces, which improves the isolation and detection of weak secondary arrivals. Furthermore, RPA uses the RT to incorporate ray parameter information. By migrating scattered or reflected phases back to their depth of origin, I am able to increase the image resolution and reduce the effect of non-specular arrivals that follow asymmetric paths. The Radon domain also provides an opportunity for data review, muting of extraneous phases and noise reduction through least squares inversion. The mini-max shape of SS and PP Fresnel zones (Shearer, 1993; Schmerr and Garnero, 2006; Deuss, 2009) further complicates the migration procedure by advancing asymmetric arrivals along the great-circle path and delaying arrivals from off axis scattering. In contrast, P'P' precursors are more advantageous since their maximum phase Fresnel volume ensures all arrivals (off or on great-circle axis) are consistent and greatly simplifies migration. A well sampled azimuthal range potentially minimizes Fresnel zone migration complications as well as other source or receiver considerations (Zheng and Romanowicz, 2012). In addition, partial stacking and Radon techniques require aggregates of data. The binning of data into caps assumes the slow variation of arrival depths, which is justified at scales similar to the Fresnel zone. Therefore, when sampling substantial topography, binning gathers in excess of the Fresnel zone could potentially succumb to averaging effects.

5.3.1 Implications for mantle stratification and dynamics

While the reflectivity structures from targeted caps is far from complete (a more comprehensive regional mapping based on P'P' precursors is currently underway), they do provide relatively unbiased comparison between long (SS) and short (P'P') period methods, especially in view of superior data densities for both precursors, and between tectonically intriguing parts of southeastern Pacific ocean basins and Nazca-South America subduction zone. For both approaches, the vast majority of the arrivals are dominated by, or exhibits

a strong component of, positive Radon amplitudes. This finding suggests an increase in impedance contrast with depth at most upper/mid mantle depths. Two notable exceptions are identified at 337 and 639 km, beneath the Pacific and western Amazon basins, respectively; their implications will be detailed in the latter part of this section. The connection between SS and P'P' precursors are undeniable: with few exceptions, broad S-wave reflection signals are typically surrounded near the end points by multiple short-wavelength P'P' arrivals. In addition to successfully verifying the existence and robustness of seismic interface(s), observations in migration profiles highlight the contrasting vertical resolving powers of these two approaches. Overall, the migration profiles of P'P' precursors show far more structural complexities in the mantle (*e.g.*, beneath ocean basins in Cap 1) than those suggested by SS precursors. Such differences are mainly manifestations of distinct bandwidths, which translate to imaging scales, and the elastic parameters of mantle rocks in response to thermal and/or compositional variations.

The outcome of the migration imaging of SS and P'P' precursors raise important questions about the temperature and mineralogy near the base of the MTZ. A major difference between the two data types is the inferred depth of the post spinel transition of olivine to perovskite and magnesiowustite (Ita and Stixrude, 1992; Bina and Helffrich, 1994; Akaogi et al., 2007). Strong signals from SS precursors commence at 640-670 km, which are comparable to or slightly shallower than globally averaged depth of 650-660 km (Flanagan and Shearer, 1998; Gu et al., 1998, 2003; Houser and Williams, 2010). This 660 is consistent with globally observed depression in subduction zones around the world, due to reduced temperatures from the subducting plate. In comparison, PP precursors infer a much deeper reflecting interface (at 686 km) under the Pacific ocean, potentially resulting from the sharp gradient associated with a transitional layer. The thickness of this strong gradient zone is likely sharp in comparison with the bandwidth of P'P' precursors ($<$ 5km) in view of the large, first-order migration amplitude.

The P reflection characteristics of the ringwoodite transition beneath plate boundary are strongly influenced by the descending Nazca plate. Nearly half of the BPs sample in

Cap 2 reside near the Peruvian Andes, providing strong sensitivity to the 660 oceanward from the steeply dipping part of the Wadati-Benioff zone. The low overall P migration amplitude in the range of 630-720 km reinforces the well-documented difficulty in observing P wave reflections at the base of the MTZ in subduction zones, and may be attributed to a number of factors. For instance, severe scattering on a strongly dipped endothermic phase boundary (Schmerr and Garnero, 2007; Contenti et al., 2012; Gu et al., 2012) is expected to cause incoherent summation near the subduction zone. A reduced impedance contrast at the interface between the high-velocity descending slab and a post-spinel lower mantle could also lower the detectability of P wave reflections. In addition, the presence of water, which could range from 1-3 wt.%, have been known to attenuate both P and S wave amplitudes. The combination of these factors leads to a gradual transition with defocused energy, as suggested by the absence of a robust P′P′ precursor signal.

While the post spinel transition is generally well-documented globally, observational support for garnet-related phase changes (Vacher et al., 1998; Akaogi et al., 2002; Hirose, 2002) have been far less pervasive (Deuss and Woodhouse, 2002; Ai and Zheng, 2003; Tibi et al., 2007; Schmerr and Thomas, 2011) or conclusive (Lebedev et al., 2002a; Gu et al., 2012). In the pyrolite model (Ringwood, 1975), olivine contributes to the majority (62%) of the upper mantle. According to high-pressure laboratory measurements, secondary mantle constituents, such as majorite garnet, can transform into ilmentite at pressure-temperature conditions at ~600 km, and ultimately to perovskite at depths slightly below the post-spinel boundary. The proximity of these two phase changes relative to that of the olivine component present a considerable challenge for phase separation and, subsequently, a proper interpretation of the discontinuity topography at the base of MTZ (Deuss, 2009; Gu and Sacchi, 2009). The migration of SS precursors in this study shows no evidence of split 660 reflections. On the other hand, the superior vertical resolution of the P′P′ precursors are ideal for isolating the effects of the various phase boundaries near the base of the upper mantle. Potential majorite garnet-ilmenite (590-640 km) and ilmenite-perovskite transition (730-735 km) are the most consistent arrivals between the two regions examined in this study. Their presence provides evidence for garnet-related phase changes, especially near

the subdution zone where cooler mantle temperatures are expected to promote their gradual transition (over an interval of ~50 km) of garnet to ilmenite (Vacher et al., 1998; Akaogi et al., 2002; Hirose, 2002). In the subduction profile, this transition likely takes place within a layer of ~40 km, starting from 599 km and potentially terminated nearby the tail at 639 km (see Figure 5.4).

One of the sharpest distinctions found in this chapter is the discrepancy between the upper MTZ arrivals, complex structure is indicated by P′P′ (337-412 km) and contrasted by a single reflection from SS (α). This may be attributed to shear velocity structure and moduli being more susceptible to change, in the presence of partially molten rock, than their compressional/bulk counterparts (Hammond and Humphreys, 2000; Wimert and Hier-Majumder, 2012). Additionally, scattering due to heterogeneity on the lithological scale is more pronounced in P′P′ in view of its higher frequency content (Stixrude and Lithgow-Bertelloni, 2012). Melt has been suggested to be globally pervasive (Tauzin et al., 2010) and its scattering effect on P′P′ could cause the well-documented difficulties in the detection of $P'_{410}P'$ reflections. Additionally, the proposition of melt implies anomalously low-velocities, which would support the observation of the initial negative arrival at 337 km. In the study region, upwelling from the nearby San Felix hotspot (26°S and 80°W) in association with a hot thermal plume (Vinnik and Farra, 2002, 2007; Vinnik et al., 2010) is a candidate for the locally observed scattering in this profile. Studies of receiver functions near the Baja Guadalupe hot spot in California (Vinnik et al., 2010) also reported the presence of discontinuity at 480 km (similar to my 475 km arrival), relegating it to yet unidentified mantle structure. The absence of $S_{410}S$ further supports chemical heterogeneity in view of the high susceptibility of shear velocity to melt. The presence of a low velocity layer atop the 410 has been proposed (Revenaugh and Sipkin, 1994; Leahy and Bercovici, 2007; Hier-Majumder and Courtier, 2011) in connection with subduction related, neutrally buoyant silicate melt. A simple $S_{410}S$ (α) and the lack of $P'_{410}P'$ in the subduction profile do not provide definitive evidence to support this hypothesis. However, these results are consistent with those of Contenti et al. (2012), where diminished $S_{410}S$ amplitudes in response to chemical heterogeneity were observed further inland.

Mid-MTZ arrivals are associated with the transition of wadsleyite to ringwoodite (Shearer, 1990; Ita and Stixrude, 1992). Also, a second transition occurring in the presence of trace calcium, allows the formation of Ca-perovskite (571 km) from the exsolution of majorite garnet (Ita and Stixrude, 1992; Weidner and Wang, 2000; Saikia et al., 2008). At nominal mantle temperatures this transition is seismically indistinguishable from wadsleyite-ringwoodite (526 and 540 km), however, colder mantle conditions from the Nazca slab cause a separation of these two transitions (Deuss and Woodhouse, 2001; Saikia et al., 2008). A hydrated mantle extending well into the transition zone would explain the strength of these arrivals through sharpening of the wadsleyite-ringwoodite transition (Inoue et al., 2010), likely to a thickness (~11 km) resonant with the P'P' bandwidth. The observation of 520 in SS (β) varies only subtly, with similar amplitude and a stronger depression (likely compounded by Ca-perovskite 'splitting') of this feature.

In addition, the presence of a mid-mantle energy is supported by both SS (Ω) and P'P' (875 km), with a strong overlap in the two subduction profiles. Candidates for deeper reflectors have been proposed *e.g.*, phase transitions in metastable garnet (Kawakatsu and Niu, 1994), stishovite (Hirose et al., 2005), hydrous magnesium silicates (van der Meijde et al., 2003; Ohtani, 2005; Courtier and Revenaugh, 2006) and Ca-perovskite (Stixrude et al., 2007). The Ca-perovskite transition being the most favorable interpretation based on the strong implication of its presence directly overhead. Both SS and P'P' migration report strong X-discontinuity (X and 243 km, respectively) peaks and a substantially sharper P'P' subduction/continental arrival than its oceanic counterpart lends further support to the preferential detection of X-discontinuity in areas of active mantle dynamics (Angel et al., 1992; Woodland, 1998; Deuss and Woodhouse, 2002). Neither upper- nor mid-mantle peaks in SS (X and Ω) are present in the Pacific P'P' migration profile. This discrepancy could be attributed to difference in Fresnel zone footprints or highlighting the sensitivity of SS to weaker discontinuities. The earliest P'P' arrivals (<100 km) are likely due to reflections from the subducting lithosphere, exacerbated by the shallow angle of slab descent over this depth interval (Soudoudi et al., 2011).

At present, limited data prevents more robust identification of transitions and conjecture of other important features such as MTZ thickness, lateral continuity of arrivals and their relative amplitudes. Future inquiry into this region with additional data will permit their analysis, thereby providing further insight to the morphology, distortion and dynamics of the subducting Nazca plate.

5.4 Conclusion

Results from this chapter establish P′P′ precursors as a legitimate means to determine mantle structure. Results suggest P′P′ is able to resolve the mantle at a scale an order of magnitude better (5 km vertically, 220 km laterally) than previous precursor studies; a scale that is more competitive with receiver functions, while retaining the BP distribution of P′P′. A tentative glimpse into mantle conditions beneath South America is inferred using both SS and P′P′ precursors, consistently showing traditional mantle features as well as the more subtle garnet transitions. Depression of the 660 is attributed to thermal variations, 520 arrivals near subducted slab material suggest a thickness resonant with P′P′ (~11 km). Evidence for a layer of melt at the top of the MTZ is supported by both SS and P′P′ with diminished SS amplitudes and complex P′P′ arrivals. This 'complex' arrival being characterized by a sharp negative arrival marking the initiation of the low velocity zone, scattered arrivals recorded incoherently throughout its extent and finalized by the arrival of the ubiquitous 410. The analysis of P′P′ precursors, coupled with appropriate methodology, presents an opportunity to study the mantle in great detail, especially when complimented by broader-scale SS or PP constraints.

CHAPTER 6

Conclusions

This thesis provides a in-depth analysis of secondary seismic precursors to main arrivals, a powerful tool in the determination of mantle reflectivity structure. Whereas much literature exists on time-domain phase identification and interpretation, especially based on SS and PP precursors, the resolution of the targeted structures often remains to be desired. The density of ray paths is a key constraint, though the recent increase of seismic networks through the US Array and F/J-Array experiments has, to a great extent, bridged the gaps among the achievable resolutions from global, regional, and exploration seismic analysis. This puts the onus squarely on the shoulders of researchers and their imaging tools to extract every possible signal on a given seismic record for a more informed interpretation of crustal and mantle seismic structures. The main objective of this thesis is to highlight the importance and contributions of improved approaches based on well-documented (SS precursors) and new (P'P') methods for mantle imaging. The chapters of this thesis effectively document a logical progression of seismic imaging methods from low (SS precursors) to high (P'P' precursors) resolution, as well as from refinements of existing (SS precursors) to new, innovative (P'P' precursors) methods. The results of this thesis provide a glimpse of the promising future in global and regional characterization of mantle seismic stratifications and dynamics based on innovative, multi-resolution approaches.

Many key findings based on the approaches outlined in this thesis could have significant implications for mantle temperatures, dynamics, phase transitions and mineral composition. Some of the results have been published in peer-reviewed journals (Chapters 2 and 3), others have been submitted or are in preparation (Chapters 4 and 5). Below is an account of key results from the various chapters.

Chapter 2 uses improved time-domain SS precursor approach to reveal the broad olivine dominated structure beneath the northwestern Pacific subduction zone. Stronger mid-MTZ reflectors are evidenced in the vicinity of descending slab material. Anti-correlated 410 and 660 topography, after slab dip corrections, indicate that local olivine phase transitions are largely controlled by perturbations in mantle temperature. This strong temperature dependence allows for the indirect interpretation of slab dynamics; a non-uniform depression of the 660 suggests deflected slab material is not flat, favouring a deformed or buckled slab underneath the Honshu island. Beneath the southern Kuril arc, gaps in reflectivity are interpreted as the penetration of the slab through these transitions, introducing chemical heterogeneity in the lower mantle.

Chapter 3 of this thesis details theory and a new implmentation of RT, which is an integral component in the P′P′ ensemble. The RT has numerous algorithms proposed throughout the literature; my method defers to a frequency based, inversion schema. Frequency methods hasten computation by solving several smaller linear systems and non-quadratic cost functions are solved using the IRLS algorithm. Tests performed on SS synthetics and receiver function data demonstrate the flexibility of the RT, while showcasing noise suppression, spatial interpolation, muting extraneous phases and differences between the inversions methods and path integrations. One of the most important features of this techniques is the addition of ray parameter information. Ray parameter is a conserved quantity in ray tracing techniques and has implications (when combined with travel time information) for the origins of rays.

Chapter 4 highlights a combined RT-migration method for both SS and P′P′ precursors. This approach proves to be as robust as and more accurate than existing approaches for

SS precursors. More importantly, it enables effective extractions of P′P′ and its precursors, which have proven to be problematic in past studies. Low amplitude precursors, complicated source mechanisms, maximum-phase Fresnel zones, phase triplication, scattering and asymmetric arrivals plague P′P′. A pedagogical approach to precursors analysis, with emphasis on these problems, was the focus of chapter 4. Deconvolution accounts for wave path dependent properties and source mechanisms due to similarities between the main arrival and precursors. Removal of these effects from the waveform estimates the reflectivity series beneath the BP, aiding stacking procedures. Partial stacking spatially blurs data over a window, compromising between noise attenuation and retaining move-out information. The transformation of seismic data to the Radon domain has many favourable properties: the attenuation of noise, muting of extraneous arrivals and addition of ray parameter information. Ray parameter is particularly important because it accounts for realistic structures like dipping interfaces or scattering. When coupled with migration, Radon data is mapped directly to an appropriate depth. Synthetic tests demonstrate that these revamped techniques resolve structures to their intrinsic limits when well sampled. In the case of more poorly sampled caps, substantially fewer traces are required for accurate and robust results than conventional methods.

Finally, chapter 5 details the setup and outcomes of a pilot experiment based on the novel techniques introduced in chapter 4. Sample data from the South America subduction zone highlights the resolving power of P′P′. Mantle structure is determined on the fine scale, depicting not only ubiquitous olvine transitions, but potential garnet and melt structures as well. Within the southeastern Pacific, the post spinel phase loop is observed as a strong broad peak in SS and sharp in comparison to P′P′ bandwidth. Accompanying the post spinel transition is a pair of subtle P′P′ arrivals, including a second-order reflection. These arrivals have been ascribed to gradual garnet-ilmenite-perovskite transitions, which are obscured in SS. Subduction-related sharpening of the wadsleyite-ringwoodite loop increases reflection amplitude, an effect which is overt in P′P′ due to resonance. Scattered arrivals situated on top of the 410 initiated with a negative amplitude arrival and absent $S_{410}S$ are conjectured to be manifestations of a low velocity melt. SS precursors are well established and provide

a benchmark to ensure P'P' interpretations are justified by consistency. Simultaneously, SS precursors provide a stark contrast displaying the limitations of its bandwidth. The use of advanced techniques benefits SS analysis as well, evidence of a dipping 660 subduction interface has been accounted for by migration. With previous methodology a dipped transition would have incorrect depth determination, or erroneously interpreted as a split phase if the dipped energy is significant.

6.1 Future direction and suggestions

Analysis of P'P' precursors has been accomplished through the methodology presented in my thesis. Sample analysis of the South America subduction zone has given the reader a taste of P'P' resolving power. Currently an in-depth study of this region is in progress, results of which will further elucidate the nature of subduction and the Nazca plate. The phase P'P' is core traveling, placing no restrictions on a 'deepest' mantle discontinuity it may probe. With future refinement of deeper arrivals, slabs can be tracked after the MTZ and into their maturity at the core-mantle boundary, potentially on a global scale. While this method has shown merit, it undoubtedly could benefit from alterations. Some of the simplest suggestions, with large potential gains, would be an investigation into the applicability of sparse Radon inversions or expanding P'P' bandwidth. The lower corner of P'P' frequency is bounded due to background noise, inhibiting increased bandwidth; however, the only presently known constraint on upper frequencies is computational cost. An investigation into the viability of higher frequency bandwidth for P'P' precursors would be beneficial, especially the spectral content of deconvolved precursors. Other investigations, which will require more effort, that inquire to the presence of coherent noise and prescribe attenuation methods may be required to retain precursor amplitude information. Overall, P'P' precursors promise to be a cutting-edge seismological tool to interrogate mantle structure, with the subject of this thesis providing a general 'cook book' for their analysis. The application and improvement of this technique will likely be a topic of great interest in future seismology studies.

Bibliography

Abma, R. "Lateral prediction for noise attenuation by t-x and f-x techniques." *Geophysics* 60 (November 1995): 1887.

Adams, R. D. "Early reflections of P'P' as an indication of upper mantle structure." *Bulletin of the Seismological Society of America* 58 (1968): 1933–1947.

Agee, Carl B. "Phase transformations and seismic structure in the upper mantle and transition zone." *Reviews in Mineralogy and Geochemistry* 37 (1998): 165–203.

Ai, Y. and T. Zheng. "The upper mantle discontinuity structure beneath eastern China." *Geophysical Research Letters* 30 (2003): 2089.

Akaogi, M., H. Takayama, H. Kojitani, H. Kawaji, and T. Atake. "Low-temperature heat capacities, entropies and enthalpies of Mg_2SiO_4 polymorphs, and $\alpha-\beta-\gamma$ and post-spinel phase relations at high pressure." *Physics and Chemistry of Minerals* 34 (2007): 169–183.

Akaogi, M., A. Tanaka, and E. Ito. "Garnet-ilmenite-perovskite transitions in the system $Mg_4Si_4O_{12}Mg_3Al_2Si_3O_{12}$ at high pressures and high temperatures: phase equilibria, calorimetry and implications for mantle structure." *Physics of the Earth and Planetary Interiors* 132 (2002): 303–324.

Ammon, C. J. "The isolation of receiver effects from teleseismic P waveforms." *Bulletin of the Seismological Society of America* 81 (December 1991): 2504–2510.

An, M., M. Feng, and Y. Zhao. "Destruction of lithosphere within the north China craton inferred from surface wave tomography." *Geochemistry, Geophysics, Geosystems* 10 (2009): 8016.

An, Y., Y. J. Gu, and M. D. Sacchi. "Imaging mantle discontinuities using least squares Radon transform." *Journal of Geophysical Research* 112 (2007).

Andrews, J. and A. Deuss. "Detailed nature of the 660 km region of the mantle from global receiver function data." *Journal of Geophysical Research* 113 (2008): B06304.

Angel, R. J., A. Chopelas, and N. L. Ross. "Stability of high- density clinoenstatite at upper mantle pressures Stability of high- density clinoenstatite at upper mantle pressures." *Nature* 358 (1992): 322–324.

Bagley, B., A. M. Courtier, and J. Revenaugh. "Melting in the deep upper mantle oceanward of the Honshu slab." *Physics of the Earth and Planetary Interiors* 175 (July 2009): 137–144.

Bassin, C. and G. Laske. "The current limits of resolution for surface wave tomography in North America." Fall Meet. Suppl. F897. *Eos. Trans. AGU* 81 (2000).

Bayly, B. "Geometry of subducted plates and island arcs viewed as a buckling problem." *Geology* 10 (December 1982): 629.

Beck, A. and M. Teboulle. "A fast iterative shrinkage-thresholding algorithm for linear inverse problems." *SIAM Journal on Imaging Sciences* 2 (2009.): 183–202.

Benz, H. M. and J. E. Vidale. "Sharpness of upper-mantle discontinuities determined from high-frequency reflections." *Nature* 365 (1993): 147–150.

Bercovici, D. and S.-i. Karato. "Whole-mantle convection and the transition-zone water filter." *Nature* 425 (September 2003): 39–44.

Beylkin, G. "Discrete Radon Transform." *IEEE Transactions on Acoustics Speech and Signal Processing* 35 (1987): 162–172.

Bijwaard, H., W. Spakman, and E. R. Engdahl. "Closing the gap between regional and global travel time tomography." *Journal of Geophysical Research* 103 (1998): 30055–30078.

Billen, M. and G. Hirth. "Rheologic controls on slab dynamics." *Geochemistry, Geophysics, Geosystems* 8 (2007): Q08012.

Billen, M. I. "Modeling the Dynamics of Subducting Slabs." *Annual Review of Earth and Planetary Sciences* 36 (2008): 325–356.

Billen, M. I. "Slab dynamics in the transition zone." *Physics of the Earth and Planetary Interiors* 183 (2010): 296–308.

Bina, C. R. "Seismological Constraints upon Mantle Composition." *Treatise on Geochemistry.* Ed. R. Carson. 2 edition. Volume 2 . Oxford: Elsevier Science Publishing, 2003. 39–59.

Bina, C. R. and H. Kawakatsu. "Buoyancy, bending, and seismic visibility in deep slab stagnation." *Physics of the Earth and Planetary Interiors* 183 (2010): 330–340.

Bina, C. R., S. Stein, F. C. Marton, and E. M. Van Ark. "Implications of slab mineralogy for subduction dynamics." *Physics of the Earth and Planetary Interiors* 127 (2001): 51–66.

Bina, Craig R. and George Helffrich. "Phase transition Clapeyron slopes and transition zone seismic discontinuity topography." *Journal of Geophysical Research* 99 (1994): 15853–15860.

Bioucas-Dias, J. and A. Figueiredo. "A new TwIST: Two-step iterative shrinkage/thresholding algorithms for image restoration." *IEEE Transactions on Image Processing* 16 (2007): 2992–3004.

Bird, P. "An updated digital model of plate boundaries." *Geochemistry, Geophysics, Geosystems* 4 (2003): 1027.

Bock, G. "Synthetic seismogram images of upper mantle structure: No evidence for a 520-km discontinuity." *Journal of Geophysical Research* 99 (1994): 15843.

Bolt, Bruce A. and Anthony Qamar. "Observations of pseudo-aftershocks from underground nuclear explosions." *Physics of the Earth and Planetary Interiors* 5 (1972): 400 - 402.

Bracewell, R. N. "Strip integration in radio astronomy." *Australian Journal of Physics* 9 (1956): 198–201.

Cao, Q., R. D. van der Hilst, M. V. de Hoop, and S.-H. Shim. "Seismic Imaging of Transition Zone Discontinuities Suggests Hot Mantle West of Hawaii." *Science* 332 (2011): 1068–.

Cao, Q., P. Wang, R. D. van der Hilst, and M. V. de Hoop S. H. Shim. "Imaging the upper mantle transition zone with a generalized Radon transform of SS precursors." *Physics of the Earth and Planetary Interiors* 180 (2010): 80–91.

Chaljub, E. and A. Tarantola. "Sensitivity of SS precursors to topography on the upper-mantle 660-km discontinuity." *Geophysical Research Letters* 24 (1997): 2613–2616.

Chang, S., S. van der Lee, M. P. Flanagan, H. Bedle, F. Marone, E. M. Matzel, M. E. Pasyanos, A. J. Rodgers, B. Romanowicz, and C. Schmid. "Joint inversion for 3-dimensional S-velocity mantle structure along the Tethyan margin." *AGU Fall Meeting Abstracts* (December 2007): A1202.

Chang, W.-F. "3-D elastic prestack, reverse-time depth migration." *Geophysics* 59 (April 1994): 597.

Chang, W.-F. and G. A. McMechan. "3-D acoustic prestack reverse-time migration." *Geophysical Prospecting* 38 (1990): 737–755.

Chen, P.-F., C. R. Bina, and E. A. Okal. "A global survey of stress orientations in subducting slabs as revealed by intermediate-depth earthquakes." *Geophysical Journal International* 159 (2004): 721–733.

Chevrot, S., L. Vinnik, and J.-P. Montagner. "Global-scale analysis of the mantle Pds phases." *Journal of Geophysical Research* 104 (1999): 20203–20220.

Chien-Min, S. "Kinetics of high-pressure phase transformations: Implications to the evolution of the olivine → spinel transition in the downgoing lithosphere and its consequences on the dynamics of the mantle." *Tectonophysics* 31 (March 1976): 1–32.

Christensen, U. "Effects of Phase Transitions on Mantle Convection." *Annual Review of Earth and Planetary Sciences* 23 (1995): 65–88.

Christensen, U. "Geodynamic models of deep subduction." *Physics of the Earth and Planetary Interiors* 127 (December 2001): 25–34.

Christensen, U. R. "The influence of trench migration on slab penetration into the lower mantle." *Earth and Planetary Science Letters* 140 (May 1996): 27–39.

Collier, J. D. and G. R. Helffrich. "The thermal influence of the subducting slab beneath South America from 410 and 660 km discontinuity observations." *Geophysical Journal International* 147 (2001): 319–329.

Collier, J. D., G. R. Helffrich, and B. J. Wood. "Seismic discontinuities and subduction zones." *Physics of the Earth and Planetary Interiors* 127 (December 2001): 35–49.

Contenti, S., Y. J. Gu, A. Okeler, and M. D. Sacchi. "Shear wave reflectivity imaging of the Nazca-South America subduction zone: Stagnant slab in the mantle transition zone?." *Geophysical Research Letters* 39 (2012): L02310.

Cormack, A. M. "Representation of a function by its line integrals, with some radiological applications." *Journal of Applied Physics* 34 (1963): 2722–2727.

Courtier, A. and J. Revenaugh. "Slabs and shear wave reflectors in the midmantle." *Geophysical Research Letters* 113 (2008).

Courtier, A. M. and J. Revenaugh. "A water-rich transition zone beneath the eastern United States and Gulf of Mexico." *Earth's Deep Water Cycle*. Ed. S. Jacobsen and S. van der Lee. AGU Monograph, 2006.

Crotwell, H. P., J. Owens, and Jeroen Ritsema. "The TauP Toolkit: Flexible seismic travel-time and ray-path utilities." *Seismological Research Letters* 70 (1999): 154–160.

Daubechies, I., M. Defrise, and C. Mol. "An iterative thresholding algorithm for linear inverse problems with a sparsity constraint." *Communications on Pure and Applied Mathematics* 41 (2004): 909–996.

Daubechies, I., R. DeVore, M. Fornasier, and C. Güntürk. "Iteratively re-weighted least squares minimization for sparse recovery." *Communications on Pure and Applied Mathematics* 63 (2010): 1–38.

Davis, J. P., R. Kind, and I. S. Sacks. "Precursors to P'P' re-examined using broad-band data." *Geophysical Journal International* 99 (1989): 595–604.

Day, E. and A. Deuss. "P'P' and PP precursor observations of the 660km seismic discontinuity." *EGU General Assembly Conference Abstracts.* May 2010, 9139.

Demets, C., R. G. Gordon, D. F. Argus, and S. Stein. "Current plate motions." *Geophysical Journal International* 101 (May 1990): 425–478.

Deon, F., M. Koch-Müller, D. Rhede, and R. Wirth. "Water and Iron effect on the P-T-x coordinates of the 410-km discontinuity in the Earth upper mantle." *Contributions to Mineralogy and Petrology* 161 (April 2011): 653–666.

Deuss, A. "Global Observations of Mantle Discontinuities Using SS and PP Precursors." *Surveys in Geophysics* 30 (2009): 301–326.

Deuss, A., S. A. T. Redfern, K. Chambers, and J. Woodhouse. "The Nature of the 660-Kilometer Discontinuity in Earth's Mantle from Global Seismic Observations of PP Precursors." *Science* 311 (2006): 198–201.

Deuss, A. and J. Woodhouse. "Seismic Observations of Splitting of the Mid-Transition Zone Discontinuity in Earth's Mantle." *Science* 294 (October 2001): 354–357.

Deuss, A. and J. H. Woodhouse. "A systematic search for mantle discontinuities using SS-precursors." *Geophysical Research Letters* 29 (April 2002): 1249.

Do, M. N. and M. Vetterli. "The finite ridgelet transform for image representation." *IEEE Transactions on Image Processing* 12 (January 2003): 16–28.

Du, Z., L. P. Vinnik, and G. R. Foulger. "Evidence from P-to-S mantle converted waves for a flat 660-km discontinuity beneath Iceland." *Earth and Planetary Science Letters* 241 (January 2006): 271–280.

Duan, Y., D. Zhao, X. Zhang, S. Xia, Z. Liu, F. Wang, and L. Li. "Seismic structure and origin of active intraplate volcanoes in Northeast Asia." *Tectonophysics* 470 (May 2009): 257–266.

Dziewoński, A. M. and D. L. Anderson. "Preliminary reference Earth model." *Physics of the Earth and Planetary Interiors* 25 (June 1981): 297–356.

Dziewoński, A. M., T. A Chou, and T. H. Woodhouse. "Determination of Earthquake Source Parameters From Waveform Data for Studies of Global and Regional Seismicity." *Journal of Geophysical Research* 86 (1981): 2825–2852.

Earle, P. S., S. Rost, P. M. Shearer, and C. Thomas. "Scattered P'P' Waves Observed at Short Distances." *The Bulletin of the Seismological Society of America* 101 (December 2011): 2843–2854.

Efron, B. "Bootstrap methods: another look at the Jackknife." *Annals of Statistics* 7 (1979): 1–26.

Engdahl, E. R, R. D van der Hilst, and J. Berrocal. "Imaging of subducted lithosphere beneath South America." *Geophysical Research Letters* 22 (1995).

Engdahl, Eric R. and Edwards A. Flinn. "Seismic Waves Reflected from Discontinuities within Earth's Upper Mantle." *Science* 163 (1969): 177–179.

Engl, H. W. and W. Grever. "Using the L-curve for determining optimal regularization parameters." *Numerical Mathematics* 69 (1994): 25–31.

Etgen, J., S. H. Gray, and Y. Zhang. "An overview of depth imaging in exploration geophysics." *Geophysics* 74 (2009): 5.

Fee, D. and K. Dueker. "Mantle transition zone topography and structure beneath the Yellowstone hotspot." *Geophysical Research Letters* 31 (September 2004): 18603.

Feng, M. and M. An. "Lithospheric structure of the Chinese mainland determined from joint inversion of regional and teleseismic Rayleigh-wave group velocities." *Journal of Geophysical Research (Solid Earth)* 115 (June 2010): 6317.

Flanagan, M. P. and Peter M. Shearer. "Global mapping of topography on transition zone velocity discontinuities by stacking SS precursors." *Journal of Geophysical Research* 103 (1998): 2673–2692.

Frost, D. J. and David Dolejs. "Experimental determination of the effect of H_2O on the 410-km seismic discontinuity." *Earth and Planetary Science Letters* 256 (2007): 182 – 195.

Fukao, Y. "Upper mantle P structure on the ocean side of the Japan-Kurile Arc." *Geophysical Journal International* 50 (September 1977): 621–642.

Fukao, Y., M. Obayashi, H. Inoue, and M. Nenbai. "Subducting slabs stagnant in the mantle transition zone." *Journal of Geophysical Research* 97 (April 1992): 4809–4822.

Fukao, Y., M. Obayashi, and T. Nakakuki. "Stagnant Slab: A Review." *Annual Review of Earth and Planetary Sciences* 37 (May 2009): 19–46.

Fukao, Y., S. Widiyantoro, and M. Obayashi. "Stagnant slabs in the upper and lower mantle transition region." *Reviews of Geophysics* 39 (2001): 291–323.

Gasparik, T. "Melting experiments on the enstatite-diopside join at 70 224 kbar, including the melting of diopside." *Contributions to Mineralogy and Petrology* 124 (July 1996): 139–153.

Gilbert, H. J., A. F. Sheehan, K. G. Dueker, and P. Molnar. "Receiver functions in the western United States, with implications for upper mantle structure and dynamics." *Journal of Geophysical Research (Solid Earth)* 108 (May 2003): 2229.

Gorbatov, A. and B. L. N. Kennett. "Joint bulk-sound and shear tomography for Western Pacific subduction zones." *Earth and Planetary Science Letters* 210 (May 2003): 527–543.

Gorbatov, A., S. Widiyantoro, Y. Fukao, and E. Gordeev. "Signature of remnant slabs in the North Pacific from P-wave tomography." *Geophysical Journal International* 142 (July 2000): 27–36.

Gossler, J. and R. Kind. "Seismic evidence for very deep roots of continents." *Earth and Planetary Science Letters* 138 (February 1996): 1–13.

Grand, Steven P. "Mantle shear–wave tomography and the fate of subducted slabs." *Philosophical Transactions of the Royal Society of London. Series A: Mathematical, Physical and Engineering Sciences* 360 (November 2002): 2475–2491.

Gu, Y. J., Y. An, M. D. Sacchi, R. Schultz, and J. Ritsema. "Mantle reflectivity structure beneath oceanic hotspots." *Geophysics Journal International* 178 (2009): 1456–1472.

Gu, Y. J. and A. M. Dziewoński. "Global variability of transition zone thickness." *Journal of Geophysical Research* 107 (July 2002): 2135.

Gu, Y. J., A. M. Dziewoński, and C. B. Agee. "Global de-correlation of the topography of transition zone discontinuities." *Earth Planet. Sci. Lett.* 157 (April 1998): 57–67.

Gu, Y. J., A. M. Dziewonski, and G. Ekström. "Preferential detection of the Lehmann discontinuity beneath continents." *Geophysical Research Letters* 28 (2001): 4655–4658.

Gu, Y. J., A. M. Dziewoński, and G. Ekström. "Simultaneous inversion for mantle shear velocity and topography of transition zone discontinuities." *Geophysical Journal International* 154 (2003): 559–583.

Gu, Y. J., A. Ökeler, and R. Schultz. "Tracking slabs beneath northwestern Pacific subduction zones." *Earth and Planetary Science Letters* 331 (2012): 269 - 280.

Gu, Y. J. and M. D. Sacchi. "Radon transform methods and their applications in mapping mantle reflectivity structure." *Surveys In Geophysics* 30 (2009): 327–354.

Gu, Y. J., R. Schultz, and A. Okeler. "Migration and Radon Imaging of the Western Pacific Subduction Zones Using SdS Waves." *AGU Fall Meeting Abstracts* (December 2008): A8.

Gudmundsson, Ó. and M. Sambridge. "A regionalized upper mantle (RUM) seismic model." *Journal of Geophysical Research* 103 (1998): 7121–7136.

Haddon, R.A.W., E.S. Husebye, and D.W. King. "Origins of precursors to P'P'." *Physics of the Earth and Planetary Interiors* 14 (1977): 41 – 70.

Hammond, W. C. and E. D. Humphreys. "Upper mantle seismic wave velocity: Effects of realistic partial melt geometries." *Journal of Geophysical Research* 105 (May 2000): 10975–10986.

Hampson, D. "Inverse velocity stacking for multiple elimination." *Journal of the Canadian Society of Explorational Geophysicists* 22 (1986): 44–55.

Hansen, P. *Rank-defiecient and discrete ill-posed problems - numerical aspects of linear inversions.* Philadelphia, PA: SIAM, 1998.

Heit, B., X. Yuan, M. Bianchi, R. Kind, and J. Gossler. "Study of the lithospheric and upper-mantle discontinuities beneath eastern Asia by SS precursors." *Geophysical Journal International* 183 (October 2010): 252–266.

Helffrich, G. "Topography of the transition zone seismic discontinuities." *Reviews of Geophysics* 38 (2000): 141–158.

Herrmann, F. J. and G. Hennenfent. "Non-parametric seismic data recovery with curvelet frames." *Geophysical Journal International* 173 (April 2008): 233–248.

Hier-Majumder, Saswata and Anna Courtier. "Seismic signature of small melt fraction atop the transition zone." *Earth and Planetary Science Letters* 308 (2011): 334 – 342.

Hill, N. R. "Prestack Gaussian-beam depth migration." *Geophysics* 66 (2001): 1240.

Hirose, K., Y. Fei, Y. Ma, and H.-K. Mao. "The fate of subducted basaltic crust in the Earth's lower mantle." *Nature* 397 (January 1999): 53–56.

Hirose, Kei. "Phase transitions in pyrolitic mantle around 670-km depth: Implications for upwelling of plumes from the lower mantle." *Journal of Geophysical Research* 107 (2002): 2078.

Hirose, Kei, Naoto Takafuji, Nagayoshi Sata, and Yasuo Ohishi. "Phase transition and density of subducted MORB crust in the lower mantle." *Earth and Planetary Science Letters* 237 (2005): 239 – 251.

Honda, S., M. Morishige, and Y. Orihashi. "Sinking hot anomaly trapped at the 410 km discontinuity near the Honshu subduction zone, Japan." *Earth and Planetary Science Letters* 261 (September 2007): 565–577.

Horbelt, S., M. Liebling, and M. Unser. "Discretization of the radon transform and of its inverse by spline convolutions." *IEEE Transactions on Medical Imaging* 21 (april 2002): 363 –376.

Houser, C., G. Masters, M. Flanagan, and P. Shearer. "Determination and analysis of long-wavelength transition zone structure using SS precursors." *Geophysical Journal International* 174 (July 2008): 178–194.

Houser, C. and Q. Williams. "Reconciling Pacific 410 and 660 km discontinuity topography, transition zone shear velocity patterns, and mantle phase transitions." *Earth and Planetary Science Letters* 296 (2010): 255–266.

Huang, J. and D. Zhao. "High-resolution mantle tomography of China and surrounding regions." *Journal of Geophysical Research (Solid Earth)* 111 (September 2006): 9305.

Ichiki, M., K. Baba, M. Obayashi, and H. Utada. "Water content and geotherm in the upper mantle above the stagnant slab: Interpretation of electrical conductivity and seismic P-wave velocity models." *Physics of the Earth and Planetary Interiors* 155 (April 2006): 1–15.

Iidaka, T. and D. Suetsugu. "Seismological evidence for metastable olivine inside a subducting slab." *Nature* 356 (April 1992): 593–595.

Inoue, T., T. Ueda, Y. Tanimoto, A. Yamada, and T. Irifune. "The effect of water on the high-pressure phase boundaries in the system Mg_2SiO_4-Fe_2SiO_4." *Journal of Physics: Conference Series* 215 (2010): 012101.

Inoue, T., H. Yurimoto, and Y. Kudoh. "Hydrous modified spinel, Mg(1.75)SiH(0.5)O4: a new water reservoir in the mantle transition region." *Geophysical Research Letters* 22 (January 1995): 117–120.

Inoue, Toru. "Effect of water on melting phase relations and melt composition in the system Mg_2SiO_4-$MgSiO_3$-H_2O up to 15 GPa." *Physics of the Earth and Planetary Interiors* 85 (1994): 237 - 263.

Irifune, T., N. Nishiyama, K. Kuroda, T. Inoue, M. Isshiki, W. Utsumi, K. Funakoshi, S. Urakawa, T. Uchida, T. Katsura, and O. Ohtaka. "The Postspinel Phase Boundary in Mg_2SiO_4 Determined by in Situ X-ray Diffraction." *Science* 279 (1998): 1698–1700.

Irifune, T. and A. E. Ringwood. "Phase transformations in subducted oceanic crust and buoyancy relationships at depths of 600-800 km in the mantle." *Earth and Planetary Science Letters* 117 (May 1993): 101–110.

Ita, Joel and Lars Stixrude. "Petrology, Elasticity, and Composition of the Mantle Transition Zone." *Journal of Geophysical Research* 97 (1992): 6849–6866.

Jasbinsek, J. J., K. G. Dueker, and S. M. Hansen. "Characterizing the 410 km discontinuity low-velocity layer beneath the LA RISTRA array in the North American Southwest." *Geochemistry, Geophysics, Geosystems* 11 (March 2010): 3008.

Ji, Y. and H.-C. Nataf. "Detection of mantle plumes in the lower mantle by diffraction tomography: Hawaii." *Earth and Planetary Science Letters* 159 (June 1998): 99–115.

Jiang, G., D. Zhao, and G. Zhang. "Seismic evidence for a metastable olivine wedge in the subducting Pacific slab under Japan Sea." *Earth and Planetary Science Letters* 270 (June 2008): 300–307.

Kanasewich, E. R., C. D. Hemmings, and T Aplasian. "N-th root stack nonlinear multi-channel filter." *Geophysics* 38 (1973): 327–338.

Kaneshima, S. and G. Helffrich. "Dipping Low-Velocity Layer in the Mid-Lower Mantle: Evidence for Geochemical Heterogeneity." *Science* 283 (March 1999): 1888.

Kaneshima, S. and G. Helffrich. "Subparallel dipping heterogeneities in the mid-lower mantle." *Journal of Geophysical Research (Solid Earth)* 108 (May 2003): 2272.

Kárason, H. and R. D. van der Hilst. "Constraints on Mantle Convection From Seismic Tomography." *The History and Dynamics of Global Plate Motions, Geophysical Monograph Series.* Ed. M. A. Richards, R. G. Gordon, and R. D. van der Hilst. Volume 121 . Washington, D.C.: American Geophysical Union, 2000. 277–288.

Karato, S. "Remote Sensing of Hydrogen in Earths Mantle." *Reviews in Mineralogy and Geochemistry* 62 (2006): 343–375.

Karato, S.-I. and P. Wu. "Rheology of the upper mantle - A synthesis." *Science* 260 (May 1993): 771–778.

Katsura, T. and E. Ito. "The system Mg_2SiO_4-Fe_2SiO_4 at high pressures and temperatures: Precise determination of stabilities of olivine, modified spinel, and spinel." *Journal of Geophysical Research* 94 (nov 1989): 15663–15670.

Kawakatsu, H. and F. Niu. "Seismic evidence for a 920-km discontinuity in the mantle." *Nature* 371 (1994): 301–305.

Kellogg, L. H., B. H. Hager, and R. D. van der Hilst. "Compositional Stratification in the Deep Mantle." *Science* 283 (March 1999): 1881.

Kendrick, Eric, Michael Bevis, Robert Smalley Jr., Benjamin Brooks, Rodrigo Barriga Vargas, Eduardo Lauria, and Luiz Paulo Souto Fortes. "The Nazca-South America Euler vector and its rate of change." *Journal of South American Earth Sciences* 16 (2003): 125 – 131.

Kennett, B. L. N. and E. R. Engdahl. "Traveltimes for global earthquake location and phase identification." *Geophysical Journal International* 105 (1991): 429–465.

Kennett, B. L. N., E. R. Engdahl, and R. Buland. "Constraints on seismic velocities in the Earth from traveltimes." *Geophysical Journal International* 122 (1995): 108–124.

Kind, P. and X. Li. "Deep earth structure-transition zone and mantle discontinuities." *Treatise on Geophysics.* Ed. G. Schubert. Volume 1 . B.V., Amsterdam: Elsevier Science Publishing, 2003. 591–618.

King, D. W. and J. R. Cleary. "A note on the interpretation of precursors to PKPPKP." *Bulletin of the Seismological Society of America* 64 (1974): 721–723.

Kohlstedt, D. L., H. Keppler, and D. C. Rubie. "Solubility of water in the α, β and γ phases of $(Mg,Fe)_2SiO_4$." *Contributions to Mineralogy and Petrology* 123 (1996): 345–357.

Korenaga, J. and T. H. Jordan. "Physics of multiscale convection in Earth's mantle: Evolution of sublithospheric convection." *Journal of Geophysical Research (Solid Earth)* 109 (January 2004): 1405.

Koyama, T., H. Shimizu, H. Utada, M. Ichiki, E. Ohtani, and R. Hae. "Water content in the mantle transition zone beneath the North Pacific derived from the electrical transition zone beneath the North Pacific derived from the electrical conductivity anomaly." *Earth's Deep Water Cycle, Geophysical Monograph Series.* Ed. S. D. Jacobsen and S. van der Lee. Volume 168 . Washington, D.C.: American Geophysical Union, 2006. 171–179.

Kreemer, C., W. E. Holt, and A. J. Haines. "An integrated global model of present-day plate motions and plate boundary deformation." *Geophysical Journal International* 154 (2003): 8–34.

Kubo, T., E. Ohtani, T. Kondo, T. Kato, M. Toma, T. Hosoya, A. Sano, T. Kikegawa, and T. Nagase. "Metastable garnet in oceanic crust at the top of the lower mantle." *Nature* 420 (December 2002): 803–806.

Kuchment, P. "Generalized transforms of radon type and their applications." *The radon transform, inverse problems, and tomography.* Ed. G. Olafsson and E. T. Quinto. Providence, RI: American Mathematical Society, 2006. 67–92.

Landweber, L. "An Iteration Formula for Fredholm Integral Equations of the First Kind." *American Journal of Mathematics* 73 (1951): 615–624.

Langston, C. A. "Structure Under Mount Rainier, Washington, Inferred From Teleseismic Body Waves." *Journal of Geophysical Research* 84 (1979): 4749–4762.

Lawrence, J. F. and P. M. Shearer. "A global study of transition zone thickness using receiver functions." *Journal of Geophysical Research (Solid Earth)* 111 (June 2006): 6307.

Lawrence, J. F. and P. M. Shearer. "Imaging mantle transition zone thickness with SdS-SS finite-frequency sensitivity kernels." *Geophysical Journal International* 174 (2008): 143–158.

Leahy, G. M. and D. Bercovici. "On the dynamics of a hydrous melt layer above the transition zone." *Journal of Geophysical Research* 112 (July 2007): 7401.

Leahy, G. M. and D. Bercovici. "Reactive infiltration of hydrous melt above the mantle transition zone." *Journal of Geophysical Research (Solid Earth)* 115 (August 2010): 8406.

Lebedev, S., S. Chevrot, and R. D. van der Hilst. "The 660-km discontinuity within the subducting NW-Pacific lithospheric slab." *Earth and Planetary Science Letters* 205 (December 2002): 25–35.

Lebedev, S., S. Chevrot, and R. D. van der Hilst. "Seismic Evidence for Olivine Phase Changes at the 410- and 660-Kilometer Discontinuities." *Science* 296 (May 2002): 1300–1302.

Lebedev, S., S. Chevrot, and R. D. van der Hilst. "The 660-km discontinuity within the subducting NW-Pacific lithospheric slab." *Earth and Planetary Science Letters* 205 (December 2002): 25–35.

Lebedev, S. and G. Nolet. "Upper mantle beneath Southeast Asia from S velocity tomography." *Journal of Geophysical Research (Solid Earth)* 108 (January 2003): 2048.

Lei, J. and D. Zhao. "P-wave tomography and origin of the Changbai intraplate volcano in Northeast Asia." *Tectonophysics* 397 (March 2005): 281–295.

LeStunff, Yves, Charles W. Wicks, and Barbara Romanowicz. "PP Precursors Under Africa: Evidence for Mid-Mantle Reflectors." *Science* 270 (1995): 74–77.

Li, C. and R. D. van der Hilst. "Structure of the upper mantle and transition zone beneath Southeast Asia from traveltime tomography." *Journal of Geophysical Research (Solid Earth)* 115 (July 2010): 7308.

Li, Chang, Robert D. van der Hilst, E. Robert Engdahl, and Scott Burdick. "A new global model for P wave speed variations in Earth's mantle." *Geochemistry, Geophysics, Geosystems* 9 (2008).

Li, J., Q.-F. Chen, E. Vanacore, and F. Niu. "Topography of the 660-km discontinuity beneath northeast China: Implications for a retrograde motion of the subducting Pacific slab." *Geophysical Research Letters* 35 (January 2008): 1302.

Li, X., S. V. Sobolev, R. Kind, X. Yuan, and C. Estabrook. "A detailed receiver function image of the upper mantle discontinuities in the Japan subduction zone." *Earth and Planetary Science Letters* 183 (December 2000): 527–541.

Ligorria, J. P. and C. J. Ammon. "Iterative deconvolution and receiver-function estimation." *Bulletin of the Seismological Society of America* 89 (October 1999): 1395–1400.

Litasov, K. D., E. Ohtani, and A. Sano. "Influence of water on major phase transitions in the Earth's mantle." *Earth's Deep Water Cycle, Geophysical Monograph Series.* Ed. S. D. Jacobsen and S. van der Lee. Volume 168 . Washington, D.C.: American Geophysical Union, 2006. 95–111.

Liu, Kelly H., Stephen S. Gao, Paul G. Silver, and Yongkai Zhang. "Mantle layering across central South America." *Journal of Geophysical Research* 108 (November 2003): 2510.

Liu, Q. and Y. J. Gu. "Seismic imaging: From classical to adjoint tomography." *Tectonophysics* 566-567 (2012): 31–66.

Mégnin, C. and B. Romanowicz. "The three-dimensional shear velocity structure of the mantle from the inversion of body, surface and higher-mode waveforms." *Geophysical Journal International* 143 (December 2000): 709–728.

Melbourne, T. and D. Helmberger. "Fine structure of the 410-km discontinuity." *Journal of Geophysical Research* 103 (May 1998): 10091–10102.

Miyashiro, A. "Hot regions and the origin of marginal basins in the western Pacific." *Tectonophysics* 122 (February 1986): 195–216.

Morelli, A. and A. M. Dziewonski. "Body Wave Traveltimes and A Spherically Symmetric P- and S-Wave Velocity Model." *Geophysical Journal International* 112 (1993): 178–194.

Nakakuki, T., M. Tagawa, and Y. Iwase. "Dynamical mechanisms controlling formation and avalanche of a stagnant slab." *Physics of the Earth and Planetary Interiors* 183 (November 2010): 309–320.

Nakanishi, Ichiro. "Reflections of PP from upper mantle discontinuities beneath the Mid-Atlantic Ridge." *Geophysical Journal* 93 (1988): 335–346.

Neele, F. "Sharp 400-km discontinuity from short-period P reflections." *Geophysical Research Letters* 23 (1996): 419–422.

Neele, F., H. de Regt, and J. VanDecar. "Gross errors in upper-mantle discontinuity topography from underside reflection data." *Geophysical Journal International* 129 (1997): 194–204.

Nishihara, Y., T. Shinmei, and S. Karato. "Grain-growth kinetics in wadsleyite: Effects of chemical environment." *Physics of the Earth and Planetary Interiors* 154 (2006): 30 – 43.

Niu, F. and H. Kawakatsu. "Depth variation of the mid-mantle seismic discontinuity." *Geophysical Research Letters* 24 (1997).

Niu, F., H. Kawakatsu, and Y. Fukao. "Seismic evidence for a chemical heterogeneity in the midmantle: A strong and slightly dipping seismic reflector beneath the Mariana subduction zone." *Journal of Geophysical Research (Solid Earth)* 108 (September 2003): 2419.

Niu, F., A. Levander, S. Ham, and M. Obayashi. "Mapping the subducting Pacific slab beneath southwest Japan with Hi-net receiver functions [rapid communication]." *Earth and Planetary Science Letters* 239 (October 2005): 9–17.

Northrup, C. J., L. H. Royden, and B. C. Burchfiel. "Motion of the Pacific plate relative to Eurasia and its potential relation to Cenozoic extension along the eastern margin of Eurasia." *Geology* 23 (August 1995): 719.

Obayashi, M., H. Sugioka, J. Yoshimitsu, and Y. Fukao. "High temperature anomalies oceanward of subducting slabs at the 410-km discontinuity." *Earth and Planetary Science Letters* 243 (March 2006): 149–158.

Ohtani, E. "Water in the Mantle." *Elements* 1 (2005): 25–30.

Ohtani, E. and T. Sakai. "Recent advances in the study of mantle phase transitions." *Physics of the Earth and Planetary Interiors* 170 (November 2008): 240–247.

Ohtani, E., M. Toma, K. Litasov, T. Kubo, and A. Suzuki. "Stability of dense hydrous magnesium silicate phases and water storage capacity in the transition zone and lower mantle." *Physics of the Earth and Planetary Interiors* 124 (June 2001): 105–117.

Okino, K., M. Ando, S. Kaneshima, and K. Hirahara. "The horizontally lying slab." *Geophysical Research Letters* 16 (1989): 1059–1062.

Oropeza, V. and M. Sacchi. "Simultaneous seismic data denoising and reconstruction via multichannel singular spectrum analysis." *Geophysics* 76 (2011): 25.

Pardo-Casas, F. and P. Molnar. "Relative motion of the Nazca (Farallon) and South American plates since Late Cretaceous time.." *Tectonics* 6 (1987): 233.

Parker, R. L. *Geophysical inverse theory.* Princeton, NJ: Princeton University Press, 1994.

Popov, M. M., N. M. Semtchenok, P. M. Popov, and A. R. Verdel. "Depth migration by the Gaussian beam summation method." *Geophysics* 75 (2010): 81.

Press, W. H., S. A. Teukolsky, W. T. Vetterling, and B. P. Flannery. *Numerical recipes in C++ : the art of scientific computing.* Cambridge, United Kingdom: Cambridge University Press, 2002.

Priestley, K., E. Debayle, D. McKenzie, and S. Pilidou. "Upper mantle structure of eastern Asia from multimode surface waveform tomography." *Journal of Geophysical Research (Solid Earth)* 111 (October 2006): 10304.

Radon, J. "Über die Bestimmung von Funktionen durch ihre Integralwerte längs gewisser Mannigfaltigkeiten." *Berichte über die Verhandlungen der Sächsische Akademie der Wissenschaften* 69 (1917): 267–277.

Ramesh, D. S., H. K. Wakatsu, S. Watada, and X. Yuan. "Receiver function images of the central Chugoku region in the Japanese islands using Hi-net data." *Earth, Planets, and Space* 57 (April 2005): 271–280.

Revenaugh, J. and T. H. Jordan. "Mantle layering from ScS reverberations. 2. The Transition zone." *Journal of Geophysical Research* 96 (November 1991): 19763–19780.

Revenaugh, J. and T. H. Jordan. "Mantle layering from ScS reverberations 3. The upper mantle." *Journal of Geophysical Research* 96 (1991): 19781–19810.

Revenaugh, J. and T. H. Jordan. "Mantle layering from ScS reverberations 4. The lower mantle and core-mantle boundary." *Journal of Geophysical Research* 96 (1991): 19811–19824.

Revenaugh, J. and S. A. Sipkin. "Seismic evidence for silicate melt atop the 410-km mantle discontinuity." *Nature* 369 (1994): 474–476.

Ribe, N.M., E. Stutsmann, Y. Ren, and R. van der Hilst. "Buckling instabilities of subducted lithosphere beneath the transition zone." *Earth and Planetary Science Letters* 254 (2007): 172–179.

Richard, G., D. Bercovici, and S.-I. Karato. "Slab dehydration in the Earth's mantle transition zone." *Earth and Planetary Science Letters* 251 (November 2006): 156–167.

Richard, G. C. and H. Iwamori. "Stagnant slab, wet plumes and Cenozoic volcanism in East Asia." *Physics of the Earth and Planetary Interiors* 183 (November 2010): 280–287.

Ringwood, A. E. *Composition and Petrology of the Earth's Mantle.* New York, USA: McGraw-Hill, 1975.

Rivière, P. J. La and X. Pan. "Spline-based inverse Radon transform in two and three dimensions." *Nuclear Science, IEEE Transactions on* 45 (aug 1998): 2224 –2231.

Romanowicz, B. "Global Mantle Tomography: Progress Status in the Past 10 Years." *Annual Review of Earth and Planetary Sciences* 31 (2003): 303–328.

Rondenay, S. "Upper mantle imaging with array recordings of converted and scattered teleseismic waves." *Surveys in Geophysics* 30 (2009): 377–405.

Rondenay, S., G. A. Abers, and P. E. van Keken. "Seismic imaging of subduction zone metamorphism." *Geology* 36 (2008): 275–278.

Rost, S. and C. Thomas. "Improving seismic resolution through array processing techniques." *Surveys in Geophysics* 30 (2009): 271–299.

Roth, E. G., D. A. Wiens, L. M. Dorman, J. Hildebrand, and S. C. Webb. "Seismic attenuation tomography of the Tonga-Fiji region using phase pair methods." *Journal of Geophysical Research* 104 (March 1999): 4795–4810.

Roth, E. G., D. A. Wiens, and D. Zhao. "An empirical relationship between seismic attenuation and velocity anomalies in the upper mantle." *Geophysical Research Letters* 27 (2000): 601.

Rychert, C. A. and P. M. Shearer. "A Global View of the Lithosphere-Asthenosphere Boundary." *Science* 324 (April 2009): 495–.

Rychert, Catherine A. and Peter M. Shearer. "Resolving crustal thickness using SS waveform stacks." *Geophysical Journal International* 180 (2010): 1128–1137.

Sacchi, M. D. "Reweighting strategies in seismic deconvolution." *Geophysics Journal International* 129 (1997): 651–656.

Sacchi, M. D. and T. J. Ulrych. "High-resolution velocity gathers and offset space reconstruction." *Geophysics* 60 (1995): 1169–1177.

Saikia, A., D. J. Frost, and D. C. Rubie. "Splitting of the 520-Kilometer Seismic Discontinuity and Chemical Heterogeneity in the Mantle." *Science* 319 (2008): 1515–1518.

Saita, T., D. Suetsugu, T. Ohtaki, H. Takenaka, K. Kanjo, and I. Purwana. "Transition zone thickness beneath Indonesia as inferred using the receiver function method for data from the JISNET regional broadband seismic network." *Geophysical Research Letters* 29 (April 2002): 070000–1.

Sambridge, M. and Ó. Gudmundsson. "Tomographic systems of equations with irregular cells." *Journal of Geophysical Research* 103 (January 1998): 773–782.

Schaeffer, A. J. and M. G. Bostock. "A low-velocity zone atop the transition zone in northwestern Canada." *Journal of Geophysical Research (Solid Earth)* 115 (June 2010): 6302.

Schimmel, M. and H. Paulssen. "Noise reduction and detection of weak, coherent signals through phase-weighted stacks." *Geophysical Journal International* 130 (1997): 497–505.

Schmerr, N. and E. J. Garnero. "Investigation of upper mantle discontinuity structure beneath the central Pacific using SS precursors." *Journal of Geophysical Research* 111 (2006).

Schmerr, N. and E. J. Garnero. "Upper Mantle Discontinuity Topography from Thermal and Chemical Heterogeneity." *Science* 318 (October 2007): 623–626.

Schmerr, N. and C. Thomas. "Subducted lithosphere beneath the Kuriles from migration of PP precursors." *Earth and Planetary Science Letters* 311 (nov 2011): 101–111.

Schmid, C., S. Goes, S. van der Lee, and D. Giardini. "Fate of the Cenozoic Farallon slab from a comparison of kinematic thermal modeling with tomographic images." *Earth and Planetary Science Letters* 204 (November 2002): 17–32.

Schubert, G., D. A. Yuen, and D. L. Turcotte. "Role of phase transitions in a dynamic mantle." *Geophysical Journal of the Royal Astronomical Society* 42 (1975): 705–735.

Schulte-Pelkum, V., G. Monsalve, A. Sheehan, M. R. Pandey, S. Sapkota, R. Bilham, and F. Wu. "Imaging the Indian subcontinent beneath the Himalaya." *Nature* 435 (2005): 1222–1225.

Schultz, R. and Yu J. Gu. "Flexible, inversion-based Matlab implementation of the Radon transform." *submitted to Computers and Geosciences* (2012).

Schultz, R. and Yu J. Gu. "P'P' Method paper." *submitted to Geophysical Journal International* (2012).

Seno, T., T. Sakurai, and S. Stein. "Can the Okhotsk plate be discriminated from the North American plate?." *Journal of Geophysical Research* 101 (1996): 11305–11316.

Shearer, P. M. "Seismic imaging of upper-mantle structure with new evidence for a 520-km discontinuity." *Nature* 344 (1990): 121 – 126.

Shearer, P. M. "Constraints on Upper Mantle Discontinuities From Observations of Long-Period Reflected and Converted Phases." *Journal of Geophysical Research* 96 (1991): 18147–18182.

Shearer, P. M. "Imaging global body-wave phases by stacking long-period SS precursors." *Journal of Geophysical Research* 96 (1991): 20353–20364.

Shearer, P. M. "Global mapping of upper mantle reflectors from long-period SS precursors." *Geophysical Journal International* 115 (1993).

Shearer, P. M. "Transition zone velocity gradients and the 520-km discontinuity." *Journal of Geophysical Research* 101 (February 1996): 3053–3066.

Shearer, P. M. "Upper mantle seismic discontinuities." *Earth's Deep Interior: Mineral Physics and Tomography From the Atomic to the Global Scale, AGU Geophysical Monograph 117.* . American Geophysical Union, 2000. 115–131.

Shearer, Peter M., Megan P. Flanagan, and Michael A. H. Hedlin. "Experiments in migration processing of SS precursor data to image upper mantle discontinuity structure." *Journal of Geophysical Research* 104 (1999): 7229–7242.

Shearer, Peter M and Guy T Masters. "Global mapping of topography on the 660-km discontinuity." *Nature* 355 (1992).

Sheehan, A. F., G. A. Abers, C. H. Jones, and A. L. Lerner-Lam. "Crustal thickness variations across the Colorado Rocky Mountains from teleseismic receiver functions." *Journal of Geophysical Research* 100 (1995): 20391–20404.

Shen, X., H. Zhou, and H. Kawakatsu. "Mapping the upper mantle discontinuities beneath China with teleseismic receiver functions." *Earth, Planets, and Space* 60 (July 2008): 713–719.

Shieh, S. R, H. Mao, R. J Hemley, and L. C. Ming. "Decomposition of phase D in the lower mantle and the fate of dense hydrous silicates in subducting slabs." *Earth Planet. Sci. Lett.* 159 (1998): 13–23.

Smyth, J. R. and D. J. Frost. "The effect of water on the 410-km discontinuity: An experimental study." *Geophysical Research Letters* 29 (May 2002): 100000–1.

Sobel, P.A. *The phase P'dP' as a means for determining upper mantle structure.* PhD thesis, University of Minnesota, Minneapolis, 1978.

Soudoudi, F., X. Yuan, G. Asch, and R. Kind. "High-resolution image of the geometry and thickness of the subducting Nazca lithosphere beneath northern Chile." *Journal of Geophysical Research* 116 (2011).

Stixrude, L. and C. Lithgow-Bertelloni. "Geophysics of Chemical Heterogeneity in the Mantle." *Annual Review of Earth and Planetary Sciences* 40 (2012): 569–595.

Stixrude, L., C. Lithgow-Bertelloni, B. Kiefer, and P. Fumagalli. "Phase stability and shear softening in $CaSiO_3$ perovskite at high pressure." *Physical Reviews B* 75 (2007).

Suetsugu, D., T. Inoue, M. Obayashi, A. Yamada, H. Shiobara, H. Sugioka, A. Ito, T. Kanazawa, H. Kawakatsu, A. Shito, and Y. Fukao. "Depths of the 410-km and 660-km discontinuities in and around the stagnant slab beneath the Philippine Sea: Is water stored in the stagnant slab?." *Physics of the Earth and Planetary Interiors* 183 (November 2010): 270–279.

Suetsugu, D., T. Inoue, A. Yamada, D. Zhao, and M. Obayashi. "Towards mapping the three-dimensional distribution of water in the transition zone from P-velocity tomography and 660-km discontinuity depths." *Earth's Deep Water Cycle, Geophysical Monograph Series*. Ed. S. D. Jacobsen and S. van der Lee. Volume 168 . Washington, D.C.: American Geophysical Union, 2006. 237–249.

Suetsugu, D., T. Isse, S. Tanaka, M. Obayashi, H. Shiobara, H. Sugioka, T. Kanazawa, Y. Fukao, G. Barruol, and D. Reymond. "South Pacific mantle plumes imaged by seismic observation on islands and seafloor." *Geochemistry, Geophysics, Geosystems* 10 (2009): Q11014.

Sugioka, H., D. Suetsugu, M. Obayashi, Y. Fukao, and Y. Gao. "Fast P- and S-wave velocities associated with the cold stagnant slab beneath the northern Philippine Sea." *Physics of the Earth and Planetary Interiors* 179 (March 2010): 1–6.

Sun, Y., F. Qin, S. Checkles, and J. P. Leveille. "3-D prestack Kirchhoff beam migration for depth imaging." *Geophysics* 65 (2000): 1592.

Tagawa, M., T. Nakakuki, and F. Tajima. "Dynamical modeling of trench retreat driven by the slab interaction with the mantle transition zone." *Earth, Planets, and Space* 59 (February 2007): 65–74.

Tateno, S., K. Hirose, N. Sata, and Y. Ohishi. "Phase relations in $Mg_3Al_2Si_3O_{12}$ to 180 GPa: Effect of Al on post-perovskite phase transition." *Geophysical Research Letters* 32 (August 2005): 15306.

Tauzin, B., E. Debayle, and G. Wittlinger. "The mantle transition zone as seen by global Pds phases: no clear evidence for a thin transition zone beneath continents." *Journal of Geophysical Research* 113 (2008).

Tauzin, B., E. Debayle, and G. Wittlinger. "Seismic evidence for a global low-velocity layer within the Earth's upper mantle." *Nature Geosci* 3 (2010): 718–721.

Teng, Ta-Liang and James P. Tung. "Upper-mantle discontinuity from amplitude data of P'P' and its precursors." *Bulletin of the Seismological Society of America* 63 (1973): 587–597.

Tetzlaff, M. and H. Schmeling. "The influence of olivine metastability on deep subduction of oceanic lithosphere." *Physics of the Earth and Planetary Interiors* 120 (June 2000): 29–38.

Thomas, C. and M. I. Billen. "Mantle transition zone structure along a profile in the SW Pacific: thermal and compositional variations." *Geophysical Journal International* 176 (2009): 113–125.

Thorson, J. R. and J. F. Claerbout. "Velocity-stack and slant-stack stochastic inversion." *Geophysics* 50 (1985): 2727–2741.

Tibi, R., D. A. Wiens, H. Shiobara, H. Sugioka, and X. Yuan. "Double seismic discontinuities at the base of the mantle transition zone near the Mariana slab." *Geophysical Research Letters* 34 (August 2007): 16316.

Tikhonov, A. N. *Ill-posed problems in the natural sciences.* Moscow, Russia: MIR publisher, 1987.

Tkalčić, Hrvoje, Megan P. Flanagan, and Vernon F. Cormier. "Observation of near-podal P'P' precursors: Evidence for back scattering from the 150220 km zone in the Earth's upper mantle." *Geophysical Research Letters* 33 (2006): 1–4.

Tonegawa, T., K. Hirahara, T. Shibutani, and N. Fujii. "Lower slab boundary in the Japan subduction zone." *Earth and Planetary Science Letters* 247 (July 2006): 101–107.

Torii, Y. and S. Yoshioka. "Physical conditions producing slab stagnation: Constraints of the Clapeyron slope, mantle viscosity, trench retreat, and dip angles." *Tectonophysics* 445 (December 2007): 200–209.

Trad, D., T. Ulrych, and M. D. Sacchi. "Latest views of the sparse Radon transform." *Geophysics* 68 (2003): 386–399.

Vacher, Pierre, Antoine Mocquet, and Christophe Sotin. "Computation of seismic profiles from mineral physics: the importance of the non-olivine components for explaining the 660 km depth discontinuity." *Physics of the Earth and Planetary Interiors* 106 (1998): 275–298.

van der Hilst, R. D. and H. Karason. "Compositional Heterogeneity in the Bottom 1000 Kilometers of Earth's Mantle: Toward a Hybrid Convection Model." *Science* 283 (March 1999): 1885.

van der Hilst, R. D., S. Widiyantoro, and E. R. Engdahl. "Evidence for deep mantle circulation from global tomography." *Nature* 386 (April 1997): 578–584.

van der Hist, R., R. Engdahl, W. Spakman, and G. Nolet. "Tomographic imaging of subducted lithosphere below northwest Pacific island arcs." *Nature* 353 (September 1991): 37–43.

Meijde, M.van der , F. Marone, D. Giardini, and S. van der Lee. "Seismic evidence for water deep in Earth's Upper Mantle." *Science* 300 (2003): 1556–1558.

Meijde, M.van der , S. van der Lee, and D. Giardini. "Seismic discontinuities in the Mediterranean mantle." *Physics of the Earth and Planetary Interiors* 148 (February 2005): 233–250.

van Keken, P. E., S. Karato, and D. A. Yuen. "Rheological control of oceanic crust separation in the transition zone." *Geophysical Research Letters* 23 (1996): 1821–1824.

Vidale, J. E., X.-Y. Ding, and S. P. Grand. "The 410-km-depth discontinuity: A sharpness

estimate from near-critical reflections." *Geophysical Research Letters* 22 (1995): 2557–2560.

Vidale, John E and Harley M Benz. "Upper-mantle seismic discontinuities and the thermal structure of subduction zones." *Nature* 356 (1992).

Vinnik, L. and V. Farra. "Subcratonic low-velocity layer and flood basalts." *Geophysical Research Letters* 29 (February 2002): 040000–1.

Vinnik, L. and V. Farra. "Low S velocity atop the 410-km discontinuity and mantle plumes." *Earth and Planetary Science Letters* 262 (October 2007): 398–412.

Vinnik, L., Y. Ren, E. Stutzmann, V. Farra, and S. Kiselev. "Observations of S410p and S350p phases at seismograph stations in California." *Journal of Geophysical Research (Solid Earth)* 115 (May 2010): 5303.

Wang, Y., T. Uchida, J. Zhang, M. L. Rivers, and S. R. Sutton. "Thermal equation of state of akimotoite $MgSiO_3$ and effects of the akimotoite-garnet transformation on seismic structure near the 660 km discontinuity." *Physics of the Earth and Planetary Interiors* 143 (June 2004): 57–80.

Weidner, D. J. and Y. Wang. "Chemical- and Clapeyron-induced buoyancy at the 660 km discontinuity." *Journal of Geophysical Research* 103 (April 1998): 7431–7442.

Weidner, D. J. and Y. Wang. "Phase transformations: Implications for mantle structure." *Earth's Deep Interior: Mineral Physics and Tomography From the Atomic to the Global Scale, Geophysical Monograph Series.* Ed. S. Karato. Volume 117 . Washington D.C.: American Geophysical Union, 2000. 215–235.

Whitcomb, J. H. and D. L. Anderson. "Reflection of P'P' seismic waves from discontinuities in the mantle." *Journal of Geophysical Research* 75 (1970): 5713–5728.

Whitcomb, James H. "Asymmetric P'P': An alternative to P'dP' reflections in the uppermost mantle (0 to 110 km)." *Bulletin of the Seismological Society of America* 63 (1973): 133–143.

Widiyantoro, S., B. L. N. Kennett, and R. D. van der Hilst. "Seismic tomography with P and S data reveals lateral variations in the rigidity of deep slabs." *Earth and Planetary Science Letters* 173 (November 1999): 91–100.

Wiggins, R. W. and R. A. Clayton. "Source shape estimation and deconvolution of teleseismic bodywaves." *Geophysical Journal International* 47 (October 1976): 151–177.

Wimert, Jesse and Saswata Hier-Majumder. "A three-dimensional microgeodynamic model of melt geometry in the Earth's deep interior." *Journal of Geophysical Research* 117 (2012): B04203.

Wölbern, I., B. Heit, X. Yuan, G. Asch, R. Kind, J. Viramonte, S. Tawackoli, and H. Wilke. "Receiver function images from the Moho and the slab beneath the Altiplano and Puna plateaus in the Central Andes." *Geophysical Journal International* 177 (2009): 296–308.

Wood, B. J. "The Effect of H_2O on the 410-Kilometer Seismic Discontinuity." *Science* 268 (April 1995): 74–76.

Woodland, Alan B. "The orthorhombic to high-P monoclinic phase transition in Mg-Fe pyroxenes: Can it produce a seismic discontinuity?." *Geophysical Research Letters* 25 (1998): 1241–1244.

Wu, W., S. Ni, and X. Zeng. "Evidence for P'P' asymmetrical scattering at near podal distances." *Geophysical Research Letters* 39 (2012): 11306.

Xu, Fei, John E. Vidale, and Paul S. Earle. "Survey of precursors to P'P': Fine structure of mantle discontinuities." *Journal of Geophysical Research* 108 (2003): 2024.

Xu, Fei, John E. Vidale, Paul S. Earle, and Harley M. Benz. "Mantle discontinuities under southern Africa from precursors to P'P'$_df$." *Geophysical Research Letters* 25 (1998): 571–574.

Xu, Y. and D. A. Wiens. "Upper mantle structure of the southwest Pacific from regional waveform inversion." *Journal of Geophysical Research* 102 (December 1997): 27439–27452.

Yamada, A., D. Zhao, T. Inoue, D. Suetsugu, and M. Obayashi. "Seismological evidence for compositional variations at the base of the mantle transition zone under Japan Islands." *Gondwana Research* 16 (2009): 482–490.

Zhao, D. "Seismological structure of subduction zones and its implications for arc magmatism and dynamics." *Physics of the Earth and Planetary Interiors* 127 (December 2001): 197–214.

Zhao, D. "Global tomographic images of mantle plumes and subducting slabs: insight into deep Earth dynamics." *Physics of the Earth and Planetary Interiors* 146 (August 2004): 3–34.

Zhao, D., A. Hasegawa, and S. Horiuchi. "Tomographic imaging of P and S wave velocity structure beneath northeastern Japan." *Journal of Geophysical Research* 97 (December 1992): 19909.

Zhao, D., S. Maruyama, and S. Omori. "Mantle dynamics of Western Pacific and East Asia: Insight from seismic tomography and mineral physics." *Gondwana Research* 11 (2007): 120–131.

Zhao, D. and E. Ohtani. "Deep slab subduction and dehydration and their geodynamic consequences: evidence from seismology and mineral physics." *Godwana Research* 16 (2009): 401–413.

Zheng, Y., T. Lay, M. P. Flanagan, and Q. Williams. "Pervasive Seismic Wave Reflectivity and Metasomatism of the Tonga Mantle Wedge." *Science* 316 (2007).

Zheng, Z. and B. Romanowicz. "Do double "SS precursors" mean double discontinuities?." *submitted to Geophysical Journal International* (2012).

Zhu, G., Y. Shi, and P. Tackley. "Subduction of the Western Pacific Plate underneath Northeast China: Implications of numerical studies." *Physics of the Earth and Planetary Interiors* 178 (January 2010): 92–99.

Zou, H., Q. Fan, and Y. Yao. "U-Th systematics of dispersed young volcanoes in NE China: Asthenosphere upwelling caused by piling up and upward thickening of stagnant Pacific slab." *Chemical Geology* 255 (2008): 134–142.